

# **Dynamic Electrothermal Model of a Sputtered Thermopile Thermal Radiation Detector for Earth Radiation Budget Applications**

by

Stéphanie Weckmann

Thesis submitted to the faculty of the  
Virginia Polytechnic Institute and State University  
In partial fulfillment of the requirements for the degree of  
Master of Science

In

Mechanical Engineering

Dr. J. R. Mahan, Chairman  
Dr. E. P. Scott  
Dr. J. R. Thomas

August 28, 1997  
Blacksburg, Virginia

Keywords : Thermocouple, Conduction, Radiation, Detector

# **Dynamic Electrothermal Model of a Sputtered Thermopile Thermal Radiation Detector for Earth Radiation Budget Applications**

By Stéphanie Weckmann  
J. Robert Mahan, Chairman  
Mechanical Engineering  
(ABSTRACT)

The Clouds and the Earth's Radiant Energy System (CERES) is a program sponsored by the National Aeronautics and Space Administration (NASA) aimed at evaluating the global energy balance. Current scanning radiometers used for CERES consist of thin-film thermistor bolometers viewing the Earth through a Cassegrain telescope.

The Thermal Radiation Group, a laboratory in the Department of Mechanical Engineering at Virginia Polytechnic Institute and State University, is currently studying a new sensor concept to replace the current bolometer: a thermopile thermal radiation detector. This next-generation detector would consist of a thermal sensor array made of thermocouple junction pairs, or thermopiles. The objective of the current research is to perform a thermal analysis of the thermopile. Numerical thermal models are particularly suited to solve problems for which temperature is the dominant mechanism of the operation of the device (through the thermoelectric effect), as well as for complex geometries composed of numerous different materials. Feasibility and design specifications are studied by developing a dynamic electrothermal model of the thermopile using the finite element method. A commercial finite element-modeling package, ALGOR, is used.

## **Acknowledgments**

First, I thank my advisor, Dr. J.R. Mahan, for giving me the opportunity to come to the United States and work with the Thermal Radiation Group, to complete my training period and furthermore to work on a Master's Degree. I am particularly thankful for the great confidence he had in me, for his support, enthusiasm and his guidance. I thank Dr. E. P. Scott and Dr. J. R. Thomas for their willingness to serve on my advisory committee.

Thanks are also extended to NASA for supporting this work under NASA Grants NCC-1-243 and NAS-1-96059.

Thanks to Mr. Lawrence W. Langley and Dr. E. L. Nelson from Vatel, for their cooperation and involvement.

My thanks also go to the TRG colleagues. Special thanks to Dr. K. J. Priestley who didn't hesitate to read the entire thesis and correct my French awkwardness. I thank also Dr. M. Haeffelin and Félix Nevárez for their support and assistance.

Most of all I thank Jérôme for helping me to make it and Pierre for the unforgettable brownies.

Finally, I am grateful to my Mother, Father and Sister for their love and never-ending encouragements.

## Table of Contents

<b>1. Introduction</b>	1
1.1 The Earth Radiation Budget	2
1.2 A Brief History of the Earth Radiation Measurements	5
1.3 Signal Processing	9
1.4 Description of the Sputtered Thermopile Thermal Radiation Detector	11
1.5 Goals and Motivations	15
<b>2. The Thermopile</b>	16
2.1 Background and Theory	17
2.1.1 The thermoelectric effects	17
2.1.2 Thermodynamics of thermoelectricity	21
2.1.3 Literature on thermoelectric effects	25
2.2 The Thermopile	26
2.2.1 Description of the device	26
2.2.2 Motivation for the choice of a thermoelectric device	29
2.2.3 The thermopile thermal model	30
2.2.4 The thermoelectric radiation detector specifications and design	34
2.2.5 Parameters available to improve the sensitivity of the device	36

<b>3. Finite Element Model</b>	38
3.1 Finite Element Formulation	38
3.2 Finite Element Software	41
3.2.1 ALGOR operation modes	41
3.2.2 Capabilities of and comments on the software	44
3.3 The Thermal Models	45
3.3.1 General assumptions and approximations	46
3.3.2 One-dimensional model	47
3.3.3 Two-dimensional model	53
3.3.4 Validation of the models	56
<b>4. Results and Discussion</b>	60
4.1 One-Dimensional and Two-Dimensional Model Results	61
4.1.1 Temperature distribution	61
4.1.2 Sensitivity	63
4.1.3 The time response	71
4.1.4 Conclusion	83
4.2 Parametric Study	84
4.2.1 Heat-source (active junction) size effect	84
4.2.2 Ramp slope effect	88
4.2.3 Heat flux boundary condition	93
4.3 Electrical Model of the Active Junction	95
<b>5. Conclusions and Recommendations</b>	99
5.1 Conclusions	99
5.2 Recommendations for further study	100

References	102
Vita	105

## List of Tables

Table 1.1. Planned EOS instrument launches [Wielicki, 1995]	7
Table 1.2. Planned CERES Host Spacecraft [Barkstrom, 1990]	8
Table 2.1. Nominal material and thermal properties of the thermopile, the absorber layer and the heat sink.	36
Table 3.1. Comparison of the finite element results obtained with ALGOR and PATRAN-ABAQUS	57
Table 4.1. Effect of junction definition on the predicted sensitivity	69
Table 4.2. Sensitivity of the detector based on the one-dimensional and two-dimensional models	70
Table 4.3. Influence of the device geometry on time constant and rms error	79
Table 4.4. Comparison between the one-dimensional and two-dimensional models	83
Table 4.5. Time constant and rms error associated with different active junction lengths	88
Table 4.6. Sensitivity, time constant and rms error for different ramp angles	93

## List of Figures

Figure 1.1.	Illustration of the global energy balance at the top of the atmosphere and at the surface of the Earth [ Bulletin of the American Meteorological Society (cover),1995]	3
Figure 1.2.	Data processing [Haeffelin, 1997]	10
Figure 1.4.	(a) Detail of a single pixel and (b) the thermopile linear array and connection leads [Mahan, 1997]	12
Figure 1.5.	The thermopile linear array and its cavity [Mahan, 1997]	13
Figure 2.1.	Electromagnetic spectrum	16
Figure 2.2.	Illustration of the Seebeck effect	18
Figure 2.3.	Illustration of the Peltier effect	19
Figure 2.4.	Thomson effect	20
Figure 2.5.	Example of a Thermopile	28
Figure 2.6.	Fabrication sequence for the thermopile linear array [Mahan, 1997]	31
Figure 2.7.	The energy balance on a system consisting of a thermal mass, $C$ , and a thermal impedance of conductance, $K$	32
Figure 2.8.	Profile of the thermocouple design	35
Figure 3.1.	Two-dimensional region subdivided in finite elements	39
Figure 3.2.	The types of available boundary conditions in ALGOR	40
Figure 3.3.	Summary of stages used in ALGOR	43
Figure 3.4.	Example of a two-dimensional mesh created on ALGOR	44
Figure 3.5.	Boundary conditions applied to the pixel	47

Figure 3.6.	One-dimensional model of the active junction	48
Figure 3.7.	Schematic representation of the one-dimensional steady-state formulation	50
Figure 3.8.	Thermocouple three-dimensional geometry	54
Figure 3.9.	Two-dimensional model of the thermocouple boundary conditions	55
Figure 3.10.	Dimensions and materials of the two-dimensional model	55
Figure 3.11.	Temperature distribution obtained with ALGOR	59
Figure 3.12.	Temperature distribution obtained with PATRAN-ABAQUS	59
Figure 4.1.	The steady-state one-dimensional temperature distribution for the boundary conditions shown in Figure 3.6.	62
Figure 4.2.	The steady-state two-dimensional temperature distribution corresponding to the boundary conditions of Figure 3.9	62
Figure 4.3.	Comparison between different type of junctions: (a) the typical design and (b) the current design.	64
Figure 4.4.	Temperature profile along the active junction	65
Figure 4.5.	The law of intermediate temperatures applied to our model	67
Figure 4.6.	Definition of three different candidate junctions according to their locations	68
Figure 4.7.	One-dimensional model time step optimization	73
Figure 4.8.	Two-dimensional model time step optimization	74
Figure 4.9.	Junction nodes selected (active junction length of 60 $\mu\text{m}$ )	75
Figure 4.10.	Time response of different junction nodes (active junction length of 60 $\mu\text{m}$ )	76
Figure 4.11.	Junction nodes selected (active junction length of 93 $\mu\text{m}$ )	77
Figure 4.12.	Time response of different junction nodes (active junction length of 93 $\mu\text{m}$ )	78
Figure 4.13.	Comparison between the finite element time response function and the “best-fit” (Equation 4.2) curve from the first-order model	81

Figure 4.14.	(a) Error (percent) between the finite element time response function and the “best-fit” curve (Equation 4.2), and (b) view with greater vertical resolution for $t \geq 0.7 \times 10^{-3}$ s.	82
Figure 4.15.	Influence of the size of the active junction on the thermal time response of the thermocouple	85
Figure 4.16.	Sensitivity of the thermocouple as a function of the active junction length	86
Figure 4.17.	Time constant of the thermocouple as a function of the active junction length	87
Figure 4.18.	Comparison of three different designs considered in the parametric study	89
Figure 4.19.	Effect of the ramp slope on the thermal time response of the thermocouple	90
Figure 4.20.	Sensitivity as a function of the ramp angle $\alpha$ . (The “best fit” curve has been provided to guide the eye through the calculated results)	92
Figure 4.21.	New model boundary conditions	94
Figure 4.22.	The distributed junction represented as (a) sixty discrete cells (61 nodes) and (b) the associated electrical model.	96

## Nomenclature

A	Cross-sectional area ( $\text{m}^2$ )
C	Heat capacity (J/K)
$C_p$	Specific heat (J/kg.K)
$E_{AB}$	Relative Seebeck Electromotive force (V)
I	Electrical current (A)
k	Thermal conductivity (W/m.K)
K	Thermal conductance (W/K)
L	Length (m)
m	Mass (kg)
n	Number of thermocouple pairs (-)
P	Radiative energy (W), heat energy (W), electrical power (W)
$P_{AB}$	Relative Peltier coefficient (V)
$q''$	Heat flux ( $\text{W}/\text{m}^2$ )
$q'''$	Heat source ( $\text{W}/\text{m}^3$ )
r	Aspect ratio (-)
R	Electrical resistance ( $\Omega$ )
$R_t$	Thermal resistance (K/W)
S	Absolute Seebeck coefficient (V/K)
T	Temperature (K)
t	Time (s)

V Electrical potential (V)  
x,y Cartesian coordinates (m)

### **Greek**

$\alpha$  Diffusivity ( $\text{m}^2/\text{s}$ )  
 $\phi, \psi$  Function of variables  
 $\lambda_n$  Eigen values  
 $\rho$  Volumetric density ( $\text{kg}/\text{m}^3$ ), resistivity ( $\Omega\text{m}$ )  
 $\sigma$  Thomson coefficient (V/K)  
 $\tau$  Time constant (s)  
 $\mu$  micro

# 1. Introduction

It is the nature of mankind to seek an understanding of the world around him, to explain natural phenomena. The Earth's climate system presents a real challenge from both an observational and a theoretical perspective. By understanding the effects of global climate change its consequences can be anticipated and mitigated.

Processes that have the potential to change the climate system, such as global warming due to the "greenhouse effect," are of major concern. For many years we have known that burning fossil fuels increases the concentration of carbon dioxide ( $\text{CO}_2$ ) within the atmosphere and that this change increases the atmospheric greenhouse effect. Recently, we have discovered that greenhouse gases other than  $\text{CO}_2$ , such as methane ( $\text{CH}_4$ ) and nitrous oxide ( $\text{N}_2\text{O}$ ), can also play a significant role in greenhouse warming.

Despite the increase in greenhouse gas concentrations, the magnitude of any resulting climate change is still not understood. This is due to the complex nature of feedback within the climate system. For example water vapor, which is the most active greenhouse gas, is believed to represent a positive feedback to global warming. However, increased amounts of water vapor due to a warming of the Earth's surface may correlate with increased cloud amounts. Clouds are known to have a net cooling effect on the atmosphere. Thus, the responses of water vapor and clouds to changes in the Earth-atmosphere system, whether anthropogenic (fossil fuel burning, deforestation) or natural (volcanic), play a key role in determining climate change.

Thus, to increase our understanding of the long-term consequences of human activities on the global environment and also to improve our capabilities for long-range weather and climate

forecasting, the international scientific community has combined its research efforts to address these scientific issues. A program of observation of variables that govern global climate change, including the radiation budget, has been undertaken. The motivation for the work described in this thesis is to adapt sputtered thermopile technology to the fabrication of detector elements in radiometers for monitoring the Earth radiation budget from space. The present effort is aimed at providing the next generation of scanning radiometers for the ongoing Cloud and Earth's Radiant Energy System (CERES) experiment and at providing the Geostationary Earth Radiation Budget (GERB) experiment with a radiation detector.

### 1.1 The Earth Radiation Budget

The global energy balance at the top of the atmosphere (TOA) can be expressed as an equilibrium between the incident solar radiation, the shortwave radiation reflected by the Earth and its atmosphere, and the longwave radiation emitted by the Earth and its atmosphere. The hypothesis on the radiative energy budget to be tested may be expressed symbolically as

$$P_i - P_r = P_e , \quad (1.1)$$

where  $P_i$  (W) is the incident solar energy,  $P_r$  (W) is the reflected solar energy and  $P_e$  (W) is the thermal energy emitted by the Earth-atmosphere system.

In terms of heat fluxes,  $\phi$  (W/m<sup>2</sup>), this balance can be written as

$$\int_t \int_s (\phi_i - \phi_r) dt ds = \int_t \int_s \phi_e dt ds , \quad (1.2)$$

where the integral over  $s$  is formed over an imaginary surface at the TOA and the integral over time,  $t$ , is formed over a sufficiently long time period.

Under equilibrium conditions, the climate system is such that the Earth absorbs as much shortwave energy as it emits in the longwave bands. If we consider the Earth in the energy balance we have another equation,

$$P_a = P_e = P_i - P_r, \quad (1.3)$$

where  $P_a$  (W) is the part of the incoming radiation absorbed by the Earth and the atmosphere. A simple model of the global energy balance at the top of the atmosphere and at the surface of the Earth is illustrated in Figure 1.1.

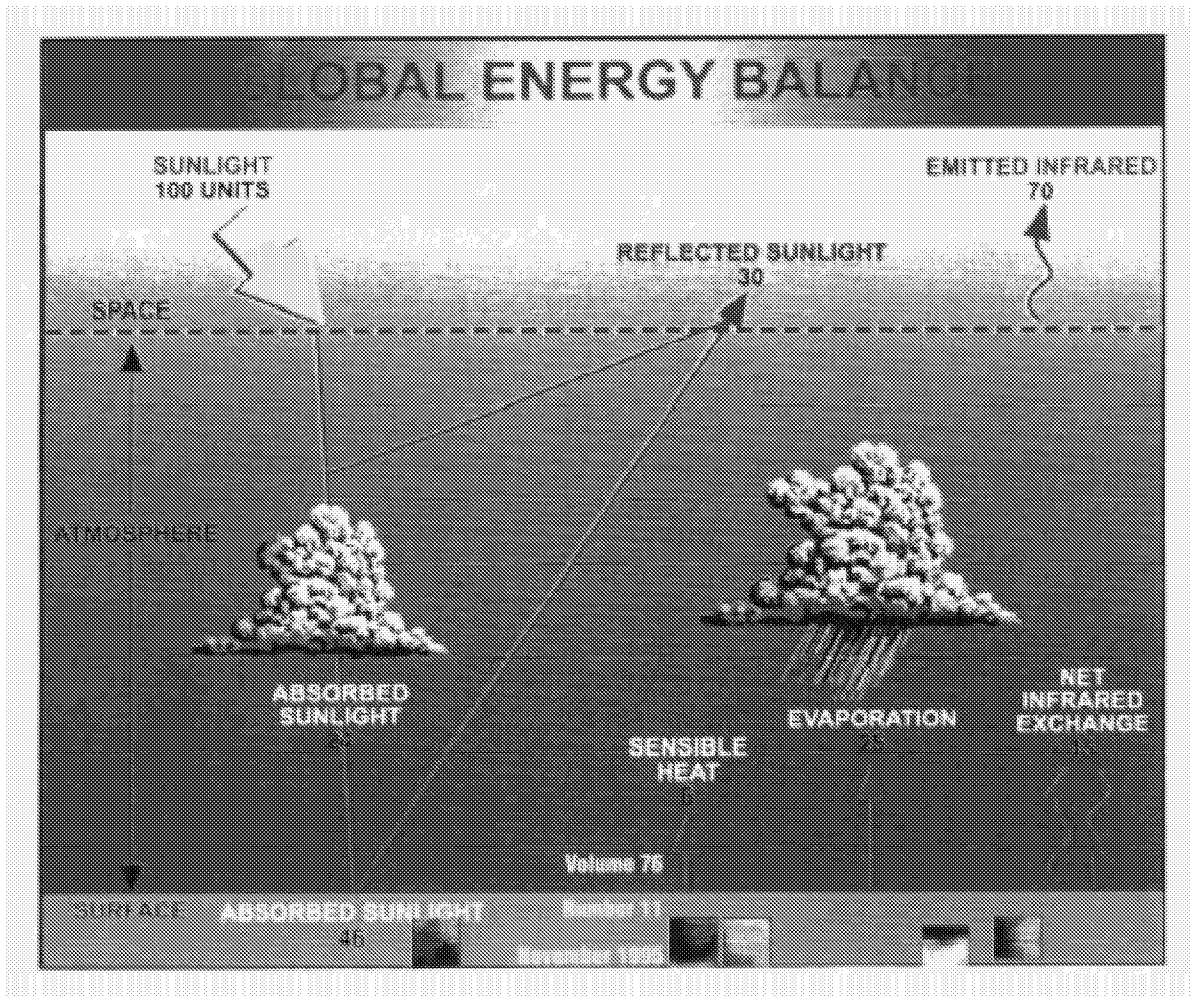


Figure 1.1. Illustration of the global energy balance at the top of the atmosphere and at surface of the Earth [Bulletin of the American Meteorological Society (cover), Volume 76, 1995]

On average, the incoming solar heat flux at the top of the atmosphere is  $340 \text{ W/m}^2$ . Of this amount roughly 30 percent (about  $100 \text{ W/m}^2$ ) is reflected back into space so that  $240 \text{ W/m}^2$  is absorbed by the Earth-atmosphere system and thus, under equilibrium conditions,  $240 \text{ W/m}^2$  is re-emitted by the Earth and the atmosphere into space. Perturbing this equilibrium, for instance by admitting a change in the chemical composition of the atmosphere such as increasing the amount of a greenhouse gas, will affect the emitted radiation. To compensate for such imbalances, the Earth will heat up until a new radiative balance is achieved [Wielicki, 1995]; hence the term “global warming.”

Global warming is also influenced by cloud feedback. The introduction of clouds enhances shortwave reflection, cooling the Earth-atmosphere system; but it also decreases the emitted long-wave radiation, warming the Earth-atmosphere system. The net result of clouds on the climate, called the net cloud radiative forcing, is a cooling effect [Ramanathan, 1989]. While this net cooling effect has been confirmed, the role of cloud feedback on the energy balance is not fully understood and remains an area of ongoing research.

Do human activities produce perturbations to the extent that the climatic equilibrium is modified? Do climate models accurately portray the influence of clouds on climate? How does the cloud feedback mechanism influence the climate? Further investigations have to be carried out to answer these questions. The Earth radiation budget and cloud properties must be observed and improvements in detection of radiative flux at the TOA must be obtained.

The goal of EOS, the Earth Observing System, is to obtain data on the emitted and reflected components of the radiation coming from the Earth; EOS is NASA’s contribution to the international Mission to Planet Earth. This program consists of space-based remote sensing platforms on Earth-orbiting satellites which provide critical global observations of the Earth’s radiation. The main aim of EOS is to understand the climate evolution over a long period of time [Anon., 1993].

## 1.2 A Brief History of Earth Radiation Measurements

In 1959 Explorer 6 made the first satellite-based Earth radiation budget measurement, and with this first attempt began an era of three generations of Earth radiation budget satellite missions between 1960 and 1984 [House, 1986]. In 1979, twenty years after Explorer 6, the United States Congress created the Earth Radiation Budget Experiment (ERBE) as a NASA program. This was the first satellite mission dedicated to measuring the Earth radiation budget using multiple satellites in order to obtain sufficient spatial and temporal coverage [Barkstrom, 1984].

The ERBE goal was to achieve spatial resolution and temporal sampling adequate to define diurnal, or daily, variations of the Earth radiation budget components [Lee, 1990]. The first ERBE satellite was launched by the space shuttle Challenger on October 8, 1984. On December 12, 1984, and September 17, 1986, two additional satellites that included ERBE instrumentation, called National Oceanic and Atmospheric Administration (NOAA) 9 and 10, were launched. Each of these satellites carried three scanning radiometers with a narrow field-of-view covering a 0.2-to-5- $\mu\text{m}$  wavelength interval (shortwave), a 5-to-50- $\mu\text{m}$  wavelength interval (longwave), and a 0.2-to-100- $\mu\text{m}$  “total” interval. They also carried four nonscanning radiometers. These nonscanning radiometers include two unfiltered total and two filtered shortwave wide and medium field-of-view (WFOV and MFOV) channels, respectively, which stare at the Earth. The nonscanning detectors are active cavity radiometers which supply electrical heat to the instrument cavity in just the amount required to compensate for the variation of incident radiation [Tira, 1987].

The results of the ERBE program are widely reported, but the 1989 article in **Science** by Ramanathan is perhaps the best summary. Briefly, these results validate the essential physics of the greenhouse effect. They confirm that water vapor is a major source of positive feedback in the climate and that clouds have a net cooling effect. It was also established that low-level clouds cool the climate through reflection of shortwave solar radiation, whereas high-level clouds cause heating through absorption and reflection of longwave radiation emitted by the Earth’s surface.

Though the question of the general effect of clouds on the Earth’s climate has been answered, the ERBE scanning radiometers were too short-lived to provide data on the cloud feedback effect.

Viewing these encouraging results and taking into account the progress made in technology, NASA planned the CERES program. CERES is a component of the EOS program that intends to maintain the same type of monitoring as ERBE. Planned EOS instrument launches can be found in Table 1.1.

CERES scanning radiometers are of the same genre as those utilized on ERBE but with improved resolution and greater accuracy. Like ERBE, CERES has three scanning radiometric channels with the longwave channel limited to a narrower band (8 to 12  $\mu\text{m}$ ) in order to measure water vapor. But unlike ERBE, CERES will not carry nonscanning channels. In the case where two CERES instrument packages are used on the same platform, they will operate in two modes: the cross-track mode, which provides continuity with ERBE data, and a biaxial rotating mode in which the scanning plane is rotated from the reference cross-track plane. This second mode will provide angular radiance data that will be used to refine the bidirectional reflectance function.

The first of the CERES instrument packages will be launched in November of 1997 aboard the Tropical Rainfall Measuring Mission (TRMM) satellite. The mission periods of the planned CERES host spacecraft to be launched may be seen in Table 1.2.

Table 1.1. Planned EOS instrument launches [Wiekicki, 1995].

Satellite	Sponsor	Launch	Measurements
TRMM <sup>1</sup>	Japan/US	1 November 1997	radiative fluxes and cloud properties
EOS-AM <sup>2</sup>	US/Japan	June 1998	radiative fluxes and cloud properties
EOS-PM <sup>3</sup>	US/ESA <sup>4</sup>	December 2000	radiative fluxes and cloud properties
METOP <sup>5</sup>	EUMETSAT <sup>6</sup>	2000	cloud properties: complements EOS-AM
EOS-ALT <sup>7</sup>	US	2002	lidar cloud height

---

<sup>1</sup> Tropical Rainfall Measuring Mission

<sup>2</sup> Earth Observing System-AM (morning equatorial crossing time)

<sup>3</sup> Earth Observing System-PM (afternoon equatorial crossing time)

<sup>4</sup> European Space Agency

<sup>5</sup> Meteorological Operational Satellite

<sup>6</sup> European Meteorological Satellite

<sup>7</sup> Earth Observing System Altimetry Mission

Table 1.2. Planned CERES Host Spacecraft [Barkstrom, 1990]

Spacecraft	Sponsor	Number of CERES Instruments	Mission Period
TRMM	NASA/ NASDA <sup>8</sup>	1	1997-2000
EOS-AM-1	NASA	2	1998-2003
EOS-PM-2	NASA	2	2001-2005

---

<sup>8</sup> National Space Development Agency (Japan)

### 1.3 Signal Processing

In order to assess the Earth radiation budget from orbit, the radiation field measurements must be converted into electronic signals. These signals are then transmitted to Earth and translated, or “inverted,” from the satellite altitude to the top of the atmosphere. The continuous signal obtained, a voltage as a function of time, is sampled so as to have a succession of values (V) for each pixel scanned. Those values are then transformed into radiance ( $\text{W}/\text{m}^2/\text{sr}$ ) using the calibration conversion function. Bidirectional Reflectivity Distribution Functions (BRDF), called also Angular Dependence Model (ADM), are used to convert the radiance into instantaneous flux at the TOA. The flux values at the TOA are then averaged over time and space to obtain a measurement of the Earth radiation budget. Figure 1.2 shows the logic flow of the data processing procedure. These data are used to develop models that determine the average monthly radiation budget and its variability on regional, zonal, and global scales.

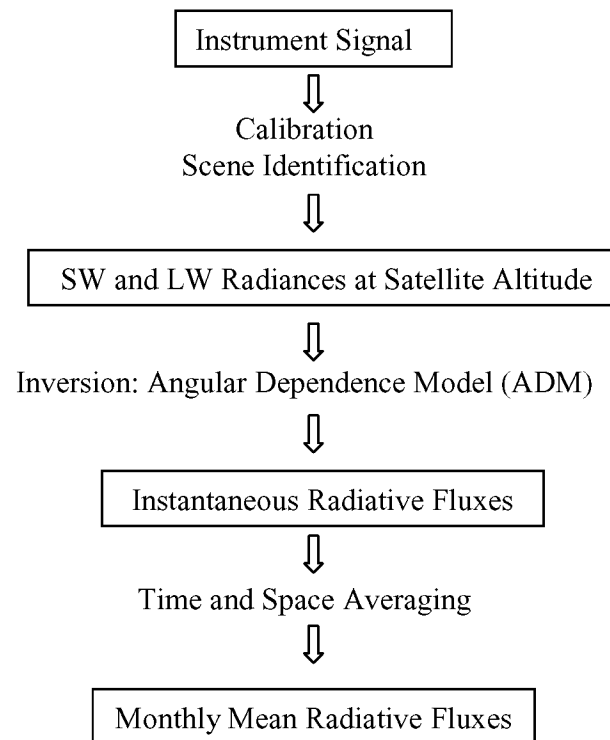


Figure 1.2. Data processing [Haeffelin, 1997]

#### **1.4 Description of the Sputtered Thermopile Thermal Radiation Detector**

A new detector concept for Earth radiation budget radiometry applications has been proposed by a team led by Prof. J. R. Mahan from the Department of Mechanical Engineering at Virginia Tech and Mr. L. W. Langley, president of Vatel Corporation [Mahan, 1996]. The intended application of the detector was the Geostationary Earth Radiation Budget (GERB) instrument. The GERB experiment was proposed by a European-American consortium lead by the United Kingdom. The GERB instrument is to be carried on a geostationary satellite with each detector pixel having a 30-by-30-km field-of-view on the Earth's surface. The satellite rotation on its axis would produce a series of scans of a linear array across the disk of the Earth. The GERB instrument is scheduled to fly on ESA's Meteosat Second Generation Satellite (MSG) and to be launched in the year 2000. The GERB-related effort has evolved into an effort to develop a next-generation detector for CERES. All of the preliminary detector design is based on the GERB instrument specifications.

The proposed detector consists of a linear array of blackened single-junction-pair thermocouples, shown in Figure 1.3. The linear array consists of 256 pixels. The 60-by-60- $\mu\text{m}$  pixels are separated from each other by a 3- $\mu\text{m}$  gap etched by a laser. Each pixel contains the active and reference junction of the thermocouple. The elements of a junction pair are electrically connected through leads attached to platinum pads at one end of the pixel (the reference junction). The output voltage is measured at the other end of the pixel (active junction). Each pixel is electrically and thermally independent.

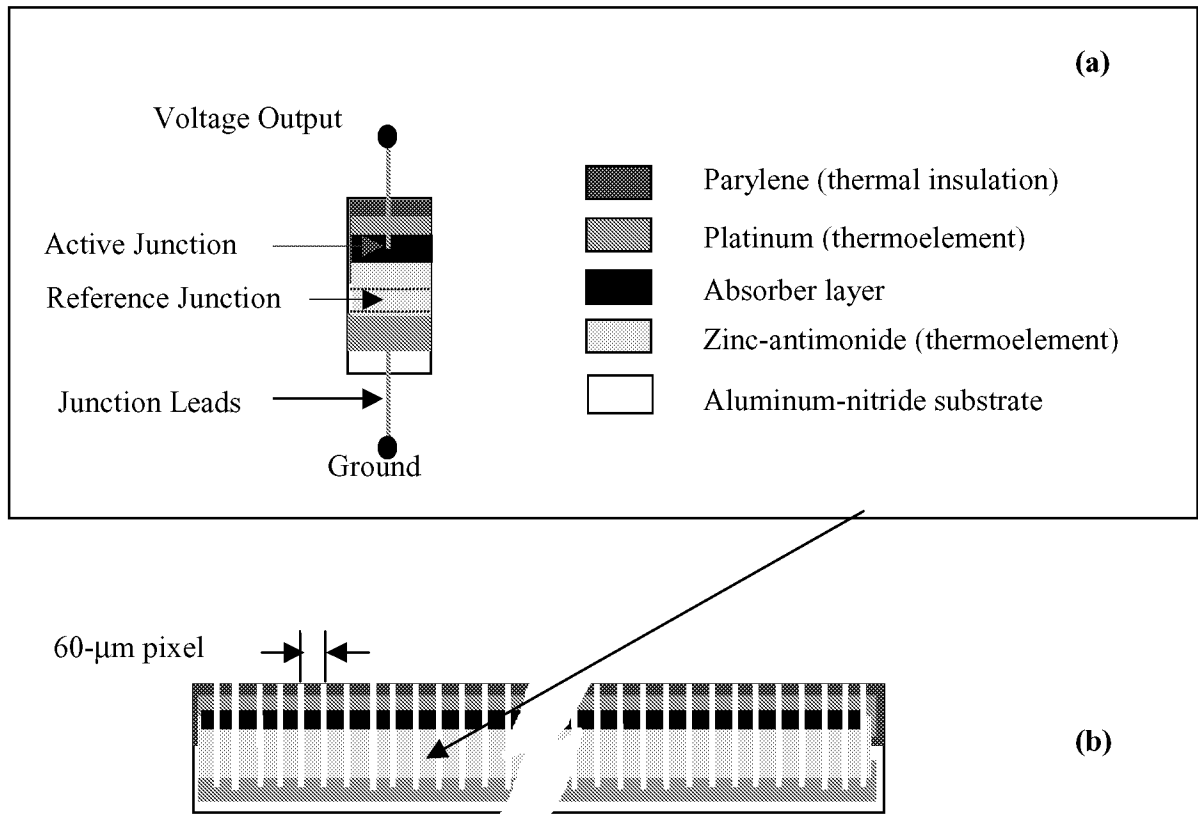


Figure 1.4. (a) Detail of a single pixel and (b) the thermopile linear array and connection leads [adapted from Mahan, 1997]

This design could be slightly changed for alternative future applications of the device, such as CERES next-generation instruments, by increasing the size of a pixel so that it contains two or more thermocouple junction pairs electrically connected in series, i.e. a thermopile. The sensitivity of the device would increase proportional to the number of thermocouple junction pairs in the thermopile.

In the proposed GERB configuration the linear array is mounted on one wall of a wedge-shaped cavity, as shown in Figure 1.5.

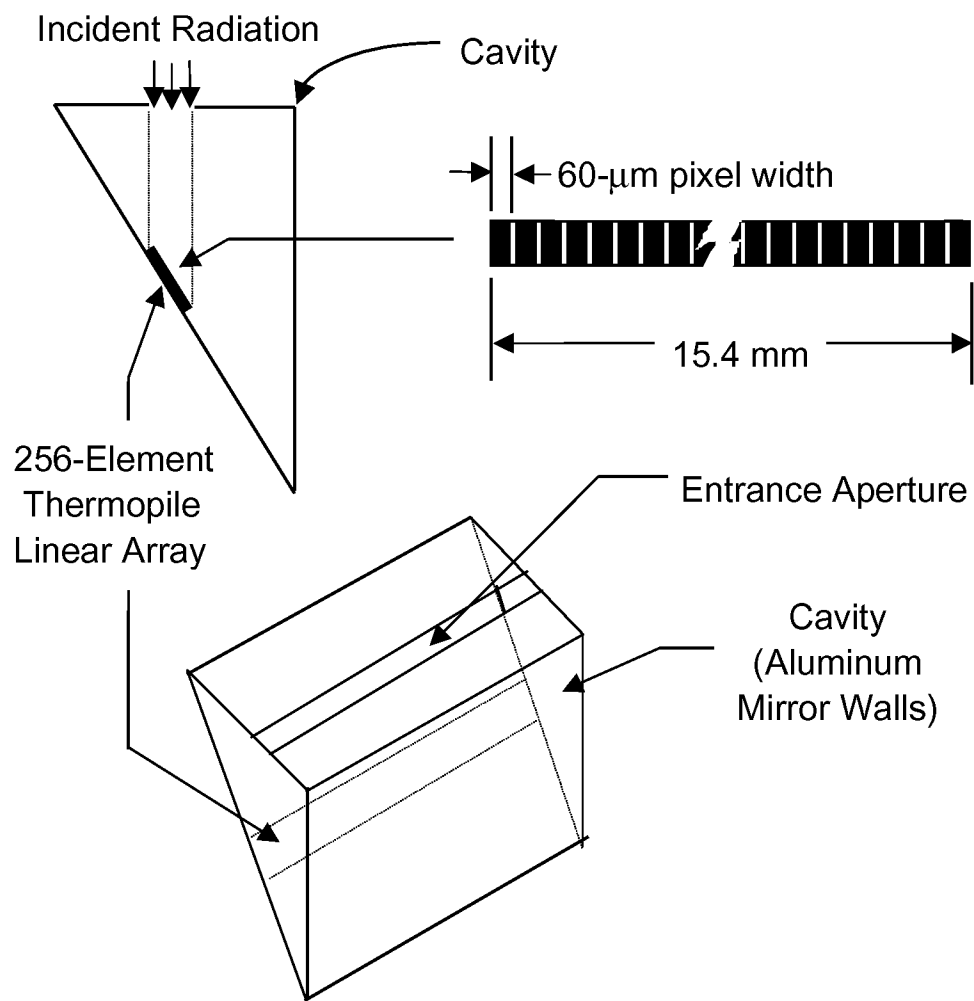


Figure 1.5. The thermopile linear array and its cavity [Mahan, 1997]

Incident radiation enters the instrument aperture through a 60- $\mu\text{m}$  entrance slit. The design of the cavity ensures that the active junctions are directly exposed to incident scene radiation, while the reference junctions are shielded by the opposite cavity mirror wall.

The active junction is coated with a high-emissivity, specularly reflecting paint. This black absorber is sufficiently thick to absorb the incoming radiation, yet sufficiently thin to respond quickly to varying radiation heat fluxes. Both the active and reference junctions are mounted on an aluminum-nitride heat sink. The reference junctions are in direct thermal contact with the heat sink, whereas the active junctions are separated from the heat sink by a thin film of polymer which acts as a thermal impedance. This thermal impedance allows the active junctions to obtain a higher temperature than the reference junctions when exposed to thermal radiation.

The detector concept is innovative in that the thermocouple junctions are made of a zinc-antimonide (ZnSb) and platinum (Pt) couple. This combination of an amorphous semiconductor and a pure metal has a very high Seebeck coefficient, or thermoelectric efficiency. The sensitivity of such a combination is increased by a factor of several hundred compared to traditional metal-metal thermocouple junctions.

In the current design the walls of the cavity and the heat sink are maintained at a constant temperature of 311 K by an actively controlled heater in order to reduce thermal noise due to variations in heating of the satellite.

## 1.5 Goals and Motivations

The Thermal Radiation Group, a laboratory in the Department of Mechanical Engineering at Virginia Polytechnic Institute and State University, has been working on instruments that measure the Earth radiation budget under the direction of Dr. J. Robert Mahan for more than 25 years. The group has provided a unique ability to combine optical, radiative, thermal conduction, and electronic models in order to produce end-to-end dynamic electrothermal models of the ERBE and CERES instruments. In the last two years the group has widened its field of study by exploring a new detector technology: sputtered thermopile thermal radiation detectors. The objective is to study the feasibility of such detectors for future-generation space-borne radiometers. The current thermistor bolometer sensor on CERES may be replaced by a thermoelectric device in the next generation of Earth radiation budget radiometers. The feasibility study is being conducted through of two interrelated efforts:

- (1) development and use of numerical models of the detector and cavity with the overall objective of defining an optimal design, and
- (2) fabrication of prototypes which reflect the optimized design.

The goal of the effort described in this thesis is limited to the development of a dynamic electrothermal model of the thermoelectric device using the finite element method. This numerical modeling effort will allow us to predict the performance of the sensor in its final structure (the cavity) and implement design strategies to predict the optimal sensor thermoelectric properties. These stated goals will be achieved through meeting specific objectives. First a study of the base-line design of a thermocouple junction pair and its limiting case is to be conducted. Then a parametric study will be performed. The thermocouple sensitivity to critical parts of the base-line design geometry will be determined by studying the effect of changing these parameters and exercising different boundary conditions

## 2. The Thermopile

Radiometry is the science of measuring thermal radiation. The atoms and molecules that compose real materials are in motion, and the interactions among them (collisions and bonding forces) produce displacements in the elementary charges within them. The resulting accelerating charges and changing electrical dipole moments produce thermal radiation. The electromagnetic spectrum is depicted in Figure 2.1.

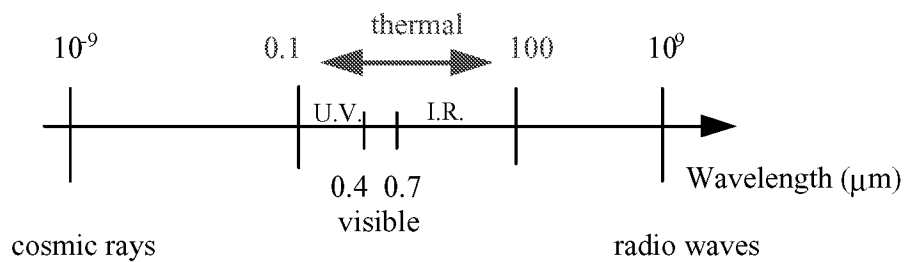


Figure 2.1. Electromagnetic spectrum

Based on the thermoelectric effect, the thermopile can be used as a heat sensor to measure thermal radiation. A thermopile is made of thermocouple junction pairs connected electrically in series. The absorption of thermal radiation by one of the thermocouple junctions, called the active junction, increases its temperature. The differential temperature between the active junction and a reference junction kept at a fixed temperature produces an electromotive force directly proportional to the differential temperature created. This effect is called a thermoelectric effect.

This chapter presents the background in thermoelectricity essential to understand the operation of a thermopile. It also presents the thermodynamics of the three effects in thermoelectricity: the Seebeck effect, the Peltier effect and the Thomson effect. The thermodynamics of thermoelectricity provides a means for describing the observed thermoelectric properties.

## **2.1 Background and Theory**

Some concepts of thermoelectricity and solid-state physics are presented below so that the reader may better understand thermopile technology based on thermoelectric effects.

### **2.1.1 The thermoelectric effects**

Any phenomenon involving an interconversion of heat and electrical energy may be termed a thermoelectric effect. We differentiate between reversible and irreversible energy conversion [Jaumont, 1960]. The best known irreversible thermoelectric effect is the Joule effect, where an electric current  $I$  (A) is transformed irreversibly into heat  $P$  (W) according to

$$P = R I^2 , \quad (2.1)$$

where  $R$  ( $\Omega$ ) is the electrical resistance of the conductor.

The Seebeck, Peltier and Thomson effects are three related reversible thermoelectric effects. The thermocouple is well known and has been used extensively over the last 100 years for measurement of temperature and process control. The principle governing the operation of thermocouple devices is the Seebeck effect.

In 1821, Thomas Johann Seebeck (1770-1831), a German scientist, discovered that a small electric current will flow in a closed circuit composed of two dissimilar metallic conductors when their junctions are kept at different temperatures. A thermocouple consists of two such dissimilar metals connected in series. The electromotive force, or emf (V), that appears in an open circuit is the emf developed by the thermocouple to block the flow of electric current. If the circuit is opened the emf created,  $E_{AB}$ , is called the relative Seebeck emf (RSE), or Seebeck voltage. The emf  $E_{AB}$  (V) created is directly proportional to the differential temperature  $\Delta T$  (K) between the two junctions

$$E_{AB} = S_{AB} \Delta T \quad , \quad (2.2)$$

where  $S_{AB}$  (V/K) is called the Seebeck coefficient.

This effect and is illustrated in Figure 2.2. The pair A-B of conductors, or thermoelements, creates the circuit which forms the thermocouple. The thermoelement A is the positive conductor with respect to B if the current flows from A to B in the cold junction.

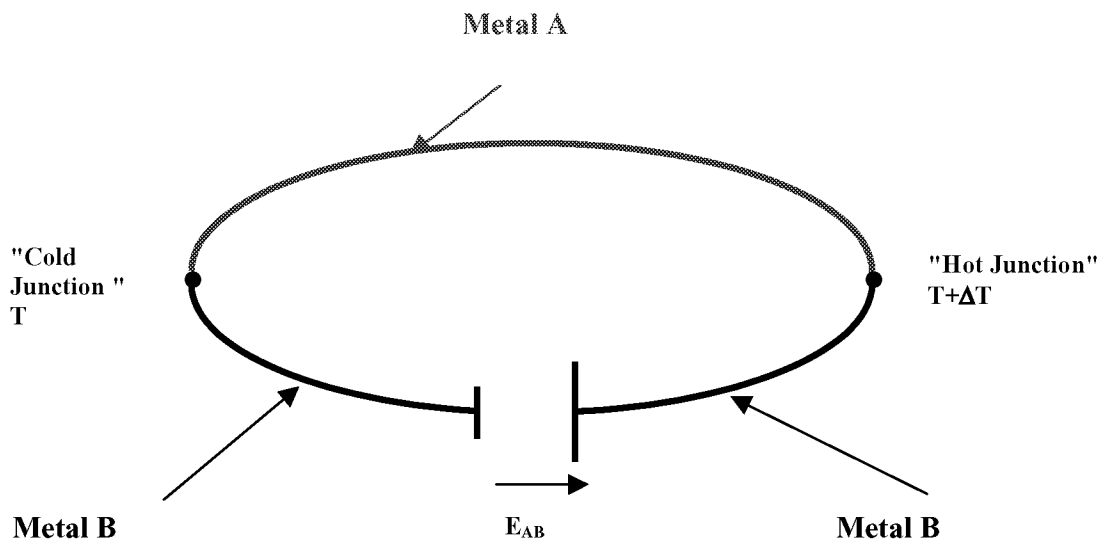


Figure 2.2. Illustration of the Seebeck effect.

In 1834, Jean Charles Athanase Peltier (1785-1845), a French watchmaker-turned-physicist, discovered that when an electric current flows across a junction of two dissimilar metals, heat is liberated or absorbed depending on the direction of this electric current compared to the Seebeck current. The rate of heat liberated or absorbed  $P$  (W) is proportional to the electric current  $I$  (A) flowing in the conductor, that is

$$P = P_{AB}(T) I, \quad (2.3)$$

where  $P_{AB}$  (V) is called the relative Peltier coefficient. This effect is the basis of thermoelectric refrigeration or heating. The Peltier effect is illustrated in Figure 2.3.

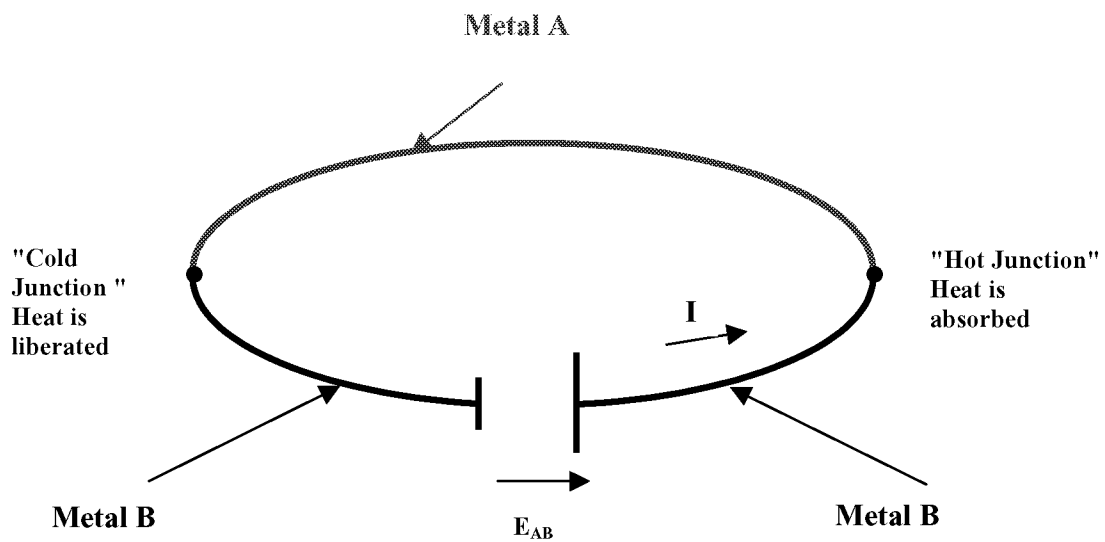


Figure 2.3. Illustration of the Peltier effect.

In 1852, Thomson discovered that if an electric current flows along a single conductor while a temperature gradient exists in the conductor, an energy interaction takes place in which power is either absorbed or rejected, depending on the relative direction of the current and gradient. More specifically heat is liberated if an electric current flows in the same direction as the heat flows; otherwise it is absorbed. Figure 2.4 illustrates the Thomson effect.

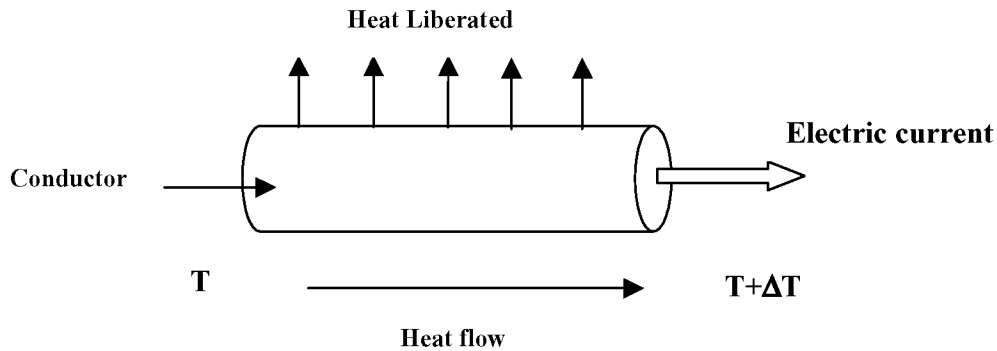


Figure 2.4. Thomson effect.

The power  $P'$  absorbed or rejected per unit length (W/m) is proportional to the product of the electric current  $I$  (A) and the temperature gradient  $\frac{dT}{dx}$  (K/m), that is

$$P' = \sigma(T) I \frac{dT}{dx}, \quad (2.4)$$

where  $\sigma(T)$  (V/K) is the Thomson coefficient.

While practical applications of the Thomson effect are few, the Seebeck effect is widely used in thermocouples to measure temperature and the Peltier effect is occasionally used for air conditioning and refrigeration units. Power generation is possible but because of the low thermal efficiency of the Peltier effect its commercial exploitation is of limited interest. Commercial exploitation of the Peltier effect has generally been limited to areas where quick heat and refrigeration is needed and where efficiency is not of utmost importance.

### 2.1.2 Thermodynamics of thermoelectricity

An understanding of the thermodynamic interdependency among the three reversible thermoelectric effects is critical. The thermodynamic theories presented here are essentially from the work of Pollock [1971].

Let us consider a thermoelectric circuit where Joule heating is neglected. This system can then be considered a reversible heat engine. Consider the circuit in Figure 2.1, where the cold junction is maintained at temperature  $T$  and the hotter junction at temperature  $T+\Delta T$  by heat sinks and sources [Pollock, 1971]. If the emf generated in this circuit is  $E_{AB}$  (V), the thermoelectric power is defined as the change in emf per degree Kelvin,  $dE_{AB}/dT$  (V/K), such that the electrical voltage is given by

$$E_{AB} = (dE_{AB}/dT) \Delta T. \quad (2.5)$$

It should be noted that although  $dE_{AB}/dT$  is called the thermoelectric *power* its dimensions are not power (W) but volts per kelvin (V/K).

Taking into account the heat absorbed and liberated at the junctions (Peltier effects) and the heat absorbed and liberated within the conductors (Thomson effects), the conservation of energy in the system, considered as a reversible heat engine, in which a current  $I$  (A) flows, can be written as

$$(dE_{AB}/dT)\Delta T I = P_{AB}(T+\Delta T) I - P_{AB}(T) I + (\sigma_B - \sigma_A)\Delta T I, \quad (2.6)$$

where  $P_{AB}(T+\Delta T) I$  (W) is the heat absorbed at the hot junction,  $P_{AB}(T) I$  (W) is the heat liberated at the cold junction,  $\sigma_B \Delta T I$  (W) is the heat absorbed in conductor B, and  $\sigma_A \Delta T I$  (W) the heat liberated in conductor A.

If we simplify Equation 2.6 by dividing through by  $I$  and  $\Delta T$  and then taking the limit as  $\Delta T$  approaches zero, we obtain the fundamental theorem of thermoelectricity,

$$\begin{aligned} dE_{AB}/dT &= (dP_{AB}/dT) + (\sigma_B - \sigma_A). \quad (2.7) \\ (V/K) &\quad (V/K) \quad (V/K) \end{aligned}$$

This equation, which is homogeneous in V/K, gives the electrical Seebeck effect as the sum of the thermal Peltier and Thomson effects. This proves the relationship between the three effects

and is the basis of the statement that the **Seebeck effect is the result of both the Peltier and Thomson effects** [Pollock, 1985].

Let us now use the assumption that the thermoelectric interactions are thermodynamically reversible, and add heat sinks at temperature  $T+\Delta T/2$  at the midpoints of the two conductors. The net change of entropy (kJ/K), of the heat sinks at the junctions and along the conductors is zero so for a unit time we can write

$$\frac{-P_{AB}(T+\Delta T) I}{T+\Delta T} + \frac{P_{AB}(T) I}{T} - \frac{\sigma_B \Delta T I}{T+(\Delta T/2)} + \frac{\sigma_A \Delta T I}{T+(\Delta T/2)} = 0 \quad (2.8)$$

(kJ/K)                      (kJ/K)                      (kJ/K)                      (kJ/K)

After dividing through by the current  $I$ , if we multiply the first two terms by  $\Delta T/\Delta T$  and then take the limit as  $\Delta T$  approaches zero, Equation 2.8 becomes

$$-\frac{d}{dT}\left(\frac{P_{AB}}{T}\right)\Delta T - \frac{\sigma_B \Delta T}{T+(\Delta T/2)} + \frac{\sigma_A \Delta T}{T+(\Delta T/2)} = 0 \quad (2.9)$$

If we now define the Thomson effect as the energy change for a temperature difference of 1 K, that is  $\Delta T=1$  K, then since  $T$  generally is much greater than 1 K, we can assume that  $T+\Delta T/2$  is essentially equal to  $T$ . We then have from Equation 2.9

$$\frac{d}{dT}\left(\frac{P_{AB}}{T}\right) = \frac{\sigma_A}{T} - \frac{\sigma_B}{T}. \quad (2.10)$$

Carrying out the indicated differentiation in Equation 2.10 and multiplying each term of the resulting equation by  $T$ , we obtain

$$\frac{P_{AB}}{T} = \left(\frac{dP_{AB}}{dT}\right) + \sigma_B - \sigma_A \quad (2.11)$$

which gives the change in entropy per unit charge of the junction at a given temperature and relates the Peltier and Thomson effects.

Equation 2.11 can be simplified using the theorem of thermoelectricity, Equation 2.7 yielding

$$P_{AB} = \left(\frac{dE_{AB}}{dT}\right)T, \quad (2.12)$$

where the Peltier coefficient,  $P_{AB}$  (V), is described with respect to the thermoelectric power,  $dE_{AB}/dT$  (V/K).

If we differentiate Equation 2.12 with respect to T, we obtain

$$\frac{dP_{AB}}{dT} = \frac{dE_{AB}}{dT} + T \frac{d^2E_{AB}}{dT^2}, \quad (2.13)$$

and if we substitute this result into the theorem of thermoelectricity, Equation 2.7, Equation 2.13 becomes

$$\frac{d^2E_{AB}}{dT^2} = \frac{\sigma_A - \sigma_B}{T}. \quad (2.14)$$

Upon integration Equation 2.14 becomes, for closed thermoelectric circuits,

$$\frac{dE_{AB}}{dT} = \oint \frac{\sigma_A - \sigma_B}{T} dT = \oint \frac{\sigma_A}{T} dT - \oint \frac{\sigma_B}{T} dT. \quad (2.15)$$

Equation 2.15 shows that the thermoelectric power of a thermocouple can be expressed in terms of the Thomson coefficients of its components. In other words, the thermoelectric power is the algebraic sum of the absolute thermoelectric powers of its components:

$$\frac{dE_{AB}}{dT} = S_A - S_B = S_{AB}, \quad (2.16)$$

where  $S_A = \int_0^T \frac{\sigma_A}{T} dT$  (V/K), and  $S_B = \int_0^T \frac{\sigma_B}{T} dT$  (V/K), are the absolute Seebeck coefficients (ASC) of each of the components of the thermocouple materials, or thermoelements, A and B. The symbol S denotes the rate of change with temperature of the Thomson voltage in a single conductor.

The concept of the ASC is very important because it allows the study of the properties of individual thermoelements. If the ASC of one thermoelement is known and the thermoelectric power of the couple is determined experimentally, the ASC of the unknown element can be calculated using Equation 2.15.

After a second integration over a closed thermoelectric circuit, Equation 2.16 becomes

$$E_{AB} = \oint S_A dT - \oint S_B dT = \oint S_{AB} dT, \quad (2.17)$$

where the integrals of the Seebeck coefficients are the absolute Seebeck effects. The flow of current in this circuit is induced by the relative Seebeck coefficient (RSE) which is a consequence of the temperature difference between the two junctions of conductors A and B. Because the Thomson effect is present only when a current passes along the conductor, the Thomson coefficients ( $\sigma_A$ ,  $\sigma_B$ ) are nonzero only in closed circuits. This means that Equation 2.15 can account for thermoelectric properties only in a closed circuit. In contrast to this, the electrical potential (emf) within conductors is always present as long as a temperature difference is maintained between the two junctions, regardless of whether the circuit is open or closed. Hence Equations 2.16 and 2.17 are valid for both open and closed circuits. Usually the RSE is measured in open circuits to eliminate the Thomson and Peltier effects, which cause extraneous thermal variations.

From Equation 2.15 the three laws of thermoelectric circuits may be inferred:

- (1) the law of homogeneous conductors,
- (2) the law of intermediate conductors, and
- (3) the law of successive temperatures.

The law of homogeneous conductors states that a thermoelectric current cannot be maintained solely by application of heat to a single homogeneous conductor, regardless of any cross-sectional variations. In other words, if a thermoelectric circuit is formed of two conductors of the same homogeneous material ( $S_A = S_B$ ), no emf exists in this circuit (Equation 2.16).

The law of intermediate conductors states that the sum of the absolute Seebeck coefficients of dissimilar conductors is zero when no temperature difference exists between the junctions. In other words no extraneous emf will be produced in a circuit made of intermediate materials if no temperature differences exist between the two ends of the materials. This law demonstrates that the contribution of a common thermoelement C to a pair of thermoelements A and B vanishes if the junctions A-C and C-B are at the same temperature.

The law of successive temperatures states that the emf of a thermocouple composed of homogeneous conductors can be measured or expressed as the sum of its properties over successive intervals of temperature. Mathematically this may be stated

$$E_{AB} = \int_{T_0}^{T_1} (S_A - S_B) dT + \int_{T_1}^{T_2} (S_A - S_B) dT + \int_{T_2}^{T_3} (S_A - S_B) dT = \int_{T_0}^{T_3} (S_A - S_B) dT . \quad (2.18)$$

### 2.1.3 Literature on thermoelectric effects

Thermodynamics provides a means for describing the observed thermoelectric properties; however it does not provide a model which can explain the mechanisms responsible for their behavior. The required model follows from an understanding of the roles of electrons in thermoelectric behavior.

The relative Seebeck emf produced in a thermoelectric circuit (RSE) has no relationship with contact potential, or Volta effect [Jastrzebski, 1976; Bridgman, 1934]. Contact potential is measured by the difference in work functions when two different metals are brought sufficiently close so that electron transfer creates a common Fermi level in both metals. This does not require a temperature difference and for closed circuits the net voltage is zero.

The thermoelectric effects can be explained by solid state physics [Callaway, 1991]. Two different materials have different free electron densities while they are both at the same temperature. A temperature difference merely gives the free electrons more kinetic energy to move around. When two materials are joined the most energetic electrons from one material will migrate to the other material in order to establish a new equilibrium of the junctions and balance the charge difference. This move disturbs the individual equilibrium of each of the materials. The disturbance is caused by the migration of energetic free electrons which leaves exposed positive charges on one side of the junction and an excess of negative charges on the other side. This causes an electric field to be formed across the junctions. Since the temperature determines how energetic the free electrons will be and since their migration determines how many exposed positive and excess negative charges are on the two sides of the junction, it follows that the magnitude of the electric field is a function of temperature. In a closed circuit a Seebeck current forms from the electric field and circulates in the loop. At one junction where the electric field has the same direction as the generated current, the current flows easily; at the other junction where the electric field and the generated current have opposite directions, the current must travel against the electric field. This explains the Peltier effect: the junction where the Seebeck

current flows easily is the junction maintained at the higher temperature and thus the current absorbs heat in an effort to cool the junction to the equilibrium temperature. At the other junction the Seebeck current has to go against the electric field, thus having to do work heating up the junction in an effort to bring the temperature up to the equilibrium temperature.

It must also be pointed out that in most references [Bridgman, 1934; Pollock, 1993] emphasis is placed on the fact that the Seebeck effect is only dependent on the temperature difference between the two junctions made of dissimilar and homogeneous conductors. It does not depend on the junction cross-section, the temperature distribution (i.e the temperature gradient) inside those conductors. This hypothesis is known as the Magnus law. Isotropy and homogeneity of the metal forming the conductors is a requirement of this law. However, because there are stresses and strains in any solid metal in which there is a temperature gradient, the universal applicability of the law must be called into question. Even with the qualification that the metal be isotropic and free from stress, there is not unanimous acceptance of this law. Benedicks [1933] claimed the existence of other thermoelectric effects not generally taken into account. Among these thermoelectric effects is a "homogeneous thermoelectric effect," which is a temperature difference in the steady state between the ends of a long uniform wire carrying a steady current. These effects are generally considered to be sufficiently small to be neglected.

## **2.2 The Thermopile**

This section is aimed at describing the thermoelectric sensor proposed for use as a thermal radiation detector. The motivation behind the choice of such a device is developed, as are detailed descriptions of its operation, specifications and expected performance.

### **2.2.1 Description of the device**

Thermocouple operation is based on the Seebeck effect; thus, the amount of electrical potential produced can be interpolated as a measure of temperature difference. But what is the relationship is there between the emf produced in the open circuit and the temperature difference between the two junctions? It all depends on the pair of thermoelements used: some pairs of

thermocouple elements give a Seebeck voltage which varies in an anticipated way with temperature. Thermocouples in common use have nearly linear temperature-emf characteristics. Once the thermocouple calibration curve is obtained, by maintaining one of the junctions at a known fixed temperature, the other junction is used as the measuring junction and is held at the temperature to be determined. The junction maintained at a known temperature is called the reference junction while the other is called the active junction.

For an ideal thermocouple, the open-circuit voltage obtained is proportional to the temperature difference between the junctions constructed of conductors A and B,

$$\Delta V = S_{AB}(T) \Delta T, \quad (2.19)$$

where  $S_{AB}$  is the relative Seebeck coefficient, expressed in  $\mu\text{V}/\text{K}$ . This coefficient depends not only on the temperature, but also on the choice of the two materials used in the thermocouple. A sign is assigned to the Seebeck coefficient according to the sign of the potential difference related to the temperature difference. However, it is much more convenient to work with absolute values: the magnitude of the Seebeck coefficient of a junction is then calculated as the absolute value of the difference between the Seebeck coefficient of each metal; that is,

$$S_{AB} = |S_A - S_B|. \quad (2.20)$$

Because a voltage is produced when a temperature difference exists between the two junctions of the thermocouple junction pair shown in Figure 2.2, the thermocouple can be used as a detector of incident radiation. In open-circuit operation the emf produced is usually low, on the order of a tenth of a microvolt per degree celsius of temperature difference for a single junction pair. In order to increase the output voltage, several junction pairs may be connected in series. The responsivity is then increased by  $n$  if  $n$  thermocouple junction pairs are placed in series; that is,

$$\Delta V = nS(T)\Delta T. \quad (2.21)$$

Such a device is called a thermopile. As shown in Figure 2.5, based on the description by Dereniak [1984], elements of a series of thermocouples of alternate material A and B are placed between a heat source and a heat sink. The hot junction comes into thermal equilibrium with the high temperature surroundings producing an emf at the leads. If a current flow results, thermal

energy is converted into electrical energy. The remaining energy absorbed at the hot junction is rejected to the heat sink at the cold junction.

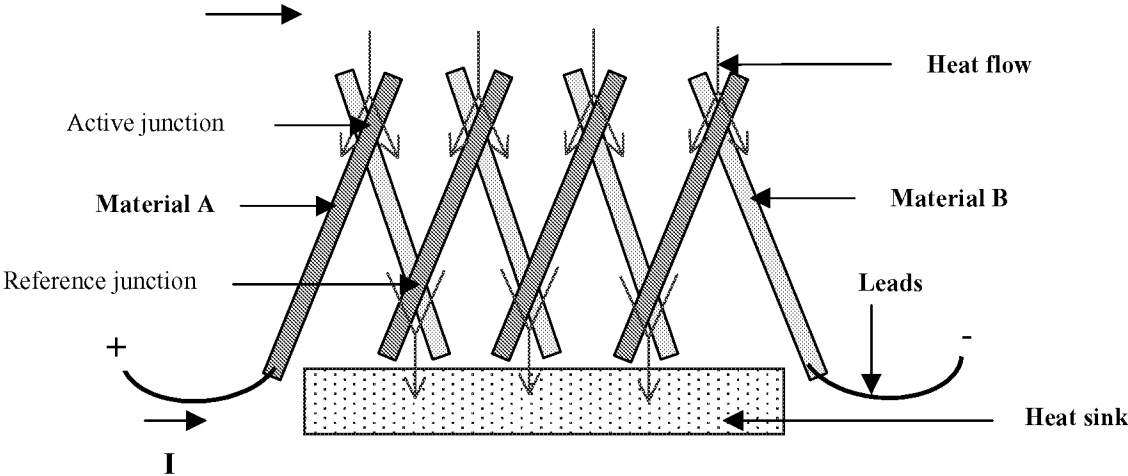


Figure 2.5. Example of a Thermopile

We now turn our attention to thermal radiation detectors. The two most important parts of all thermal radiation detectors are the absorber and the temperature transducer. When a thermopile is used, the radiant energy is absorbed into a layer coated on the active junction which acts as the heat source, and the difference of temperature between the active and the reference junctions is translated into an output voltage through the Seebeck effect. In most practical implementations we can neglect the Joule, Thomson and Peltier effects because the input impedance of the signal-conditioning circuit is sufficiently high to ensure that a negligible current flows through the thermopile.

### 2.2.2 Motivation for the choice of a thermoelectric device

The main goal of this research is to develop a thermal radiation detector capable of measuring small radiation heat fluxes (on the order of  $1 \text{ W/m}^2$ ) arriving from the Earth when the device is in a high Earth orbit. One of our first motivations for replacing the current CERES bolometer sensors with thermopiles is to achieve higher sensitivity. The new thermoelectric sensor, whether for the GERB program (linear array of thermocouple sensors) or for future CERES-like missions (more likely to be a linear array of thermopiles), must be capable of accurate heat flux measurements.

The use of a thermopile in this application offers many advantages over the bolometer. First, bolometers need a matched pair of thermistors in adjacent arms of a two-active-arm bridge circuit. If the instrument temperature changes, both the active and compensating sensors will be affected in the same way and the bridge will deflect in a known way. Measuring the output voltage by adding an external circuit has many drawbacks. First, it is not easy to manufacture two thermistors with exactly the same physical properties and dimensions. It is also difficult to estimate the self-heating effect in the thermistors, which must carry a current in order for their resistances to be measured. In the case of the thermopile a compensating element is not needed. The thermopile generates its own emf and therefore does not need a bias power supply as does the thermistor bridge circuit. Thus, no self-heating or other thermoelectric effects are present. In addition, the thermopile has the advantage of measuring temperature differences directly without any offset: if no radiation hits the detector, the output voltage signal is zero [Dereniak, 1984]. The thermopile also provides a potentially fast time response.

Furthermore, progress is currently being made at Vatech, Inc., in the field of microsensor element manufacturing. Vatech has a unique ability to exploit this latest technology. Vatech's current thermopile manufacturing process uses sputtering technology, which consists of a vacuum chamber where an inert gas is introduced and ionized. The ions are accelerated by an electric field and directed onto a metal target. Metal ions are liberated by the kinetic energy exchange with the gaseous ions and eventually condense into a film on the desired surface. The total thickness of the sensor elements laid down on the surfaces with this process is less than  $2 \mu\text{m}$ . Thus, the resulting sensor has a small volume and therefore a minimum heat capacity and

therefore a fast time response. The current thermopiles sold by Vatec have time responses of 5 to 10  $\mu$ s. Once the thin-film layers have been deposited on the substrate they are laser sliced into pixels, with each pixel yielding a thermocouple junction pair. Actually, this process allows thousands of nearly identical microsensors to be manufactured in one run, on a micrometer size scale. The sensitivity of the thermopile and its performance-to-cost ratio are in this way improved. Figure 2.6 shows the fabrication sequence for the thermopile linear-array thermal radiation detector.

The semiconductor sensor technology field is also moving at a rapid pace [Sze, 1994], and is still under intensive study. The use of semiconductor materials provides a far better Seebeck coefficient which, according to Equation 2.20, directly increases the sensitivity of the device. The current detector concept is unique because it uses thermocouple junctions made of platinum and an amorphous semiconductor of zinc and antimony (50 percent Zn-50 percent Sb). This combination can give values of the Seebeck coefficient as high as 900 mV/K according to Krieder [1994]. In other words it increases the Seebeck coefficient by a factor of several hundred over traditional metal-metal junctions.

With these encouraging prospects, the goal to develop a detector with high sensitivity, a low electrical resistance, a fast time response and in a repeatable way appears achievable.

### 2.2.3 The thermopile thermal model

If, at a certain level of complexity, we consider the one-junction-pair thermopile as a lumped system, the heat exchanges with the external environment are the heat input, that is the radiant energy incident to the detector (at  $T$ ), and the heat losses through conduction to the heat sink and radiation to the surroundings (at  $T_a$ ). If we assume that the temperature of the absorbing layer of the thermopile is near the ambient temperature, the heat loss through radiation can be neglected. Figure 2.7 shows the energy balance for the system.



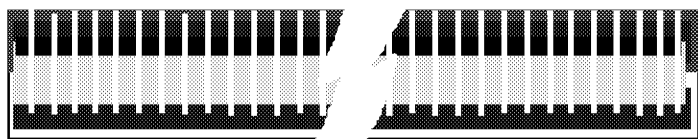
Step 1. Parylene thermal insulation (red) deposited on aluminum nitride substrate (white).



Step 2. Platinum (blue) busses are sputtered onto parylene and aluminum nitride.



Step 3. Zinc-antimonide (yellow) is sputtered to form junctions with the two platinum busses.



Step 4. Active junction is coated with an absorber layer (black) and then laser sliced into pixels.

Figure 2.6. Fabrication sequence for the thermopile linear array [Mahan, 1997]

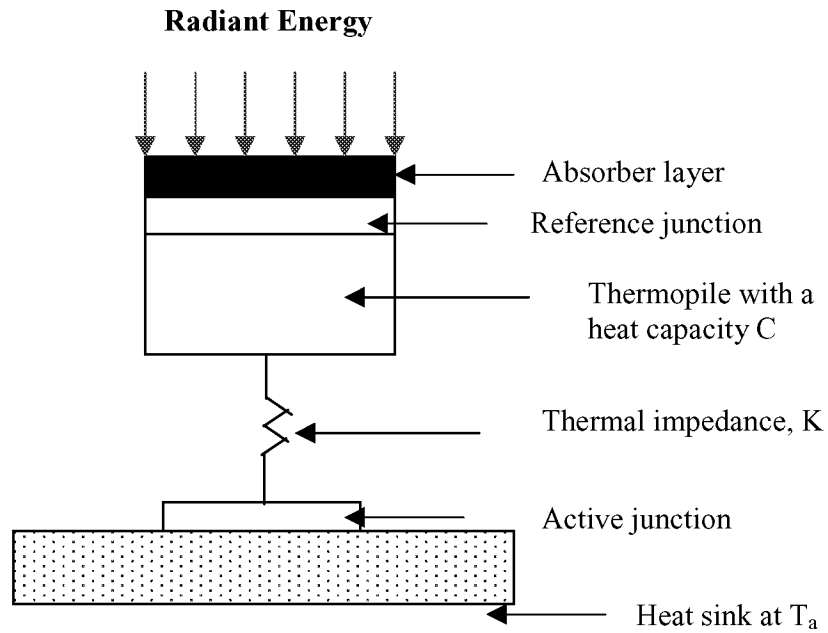


Figure 2.7. The energy balance on a system consisting of a thermal mass,  $C$ , and a thermal impedance of conductance  $K$ .

For this specific system the energy balance leads to

$$C \frac{d\Delta T}{dt} + K \Delta T = P_e \quad (2.22)$$

In Equation 2.22  $P_e$  is the radiant energy absorbed in the absorber layer (W),  $K$  the thermal conductance (W/K) between the thermopile and the heat sink, and  $C$  the heat capacity of the thermopile (J/K),

$$C = m C_p, \quad (2.23)$$

where  $m$  is the mass (kg) and  $C_p$  is the specific heat (J/kg.K) of the thermopile, and the thermal conductance,  $K$ , is defined by

$$K = \frac{A k}{L}, \quad (2.24)$$

where  $L$  is the length (m),  $A$  is the cross-sectional area ( $m^2$ ) and  $k$  the conductivity of the material (W/m K).

If the rate of absorbing radiant energy is constant, the solution to Equation 2.22 is

$$\Delta T = \frac{P_e}{K} \left( 1 - e^{-\frac{K}{C}t} \right) , \quad (2.25)$$

so the thermal radiation detector behaves like a first-order system with a thermal time constant of

$$\tau = \frac{C}{K} . \quad (2.26)$$

Therefore Equation 2.25 can be written

$$\Delta T = \frac{P_e}{K} \left( 1 - e^{-t/\tau} \right) . \quad (2.27)$$

The output voltage of a thermocouple can be computed by simply multiplying the temperature difference by the Seebeck coefficient, yielding

$$V = n S \Delta T = n S \frac{P_e}{K} \left( 1 - e^{-t/\tau} \right) . \quad (2.28)$$

The sensitivity of the instrument is defined as the output voltage divided by the input power and has the units of  $V/W/m^2$ , that is

$$\text{Sensitivity} = \frac{V}{P_e} = \frac{n S}{K} \left( 1 - e^{-t/\tau} \right) . \quad (2.29)$$

In order to minimize the time response, a system needs a high thermal conductance  $K$  and a small heat capacitance  $C$ , whereas to maximize the sensitivity, given by Equation 2.29, a system needs a small thermal conductance  $K$ , a large Seebeck coefficient  $S$  and a sufficient number of thermocouple pairs  $n$ . This suggests that the thermal conductance  $K$  between the thermopile and the heat sink has to be optimized in order to meet the requirements of both high sensitivity and fast time response. Thus, the function of the parylene thermal resistance layer is critical since the value of the thermal capacitance  $K$  depends mainly on its thermal conductivity and dimensions.

#### 2.2.4 The thermoelectric radiation detector specifications and design

The proposed sensor consists of a linear array of thermocouple junction pairs. Each thermocouple junction pair is made of platinum and zinc-antimonide with an active junction laid down on a thermal resistance layer made of parylene to insulate it from an aluminum-nitride heat sink. A detailed profile of one thermocouple junction pair showing the materials and layer thicknesses appears in Figure 2.8.

The primary function of the parylene thermal resistance layer is to increase the device sensitivity. However, we have seen that it also influences the time response. An absorber layer is added on top of the device to absorb the incident radiation. The spectral absorptivity of the absorber determines the device spectral response, since the temperature change produced at the thermopile junctions is directly related to the amount of power absorbed by the absorber layer. For that reason the absorber must be chosen with care to give as spectrally flat a response as possible. This is what motivates our choice of the same absorber material as that used on the bolometer of the CERES instruments [Priestley, 1997]. This absorber material is made of black Chemglaze z-306 paint with 10 percent additional carbon to maximize its absorptance.

Table 2.1 shows the nominal material and the thermal properties of the thermopile, the absorber layer and the heat sink.

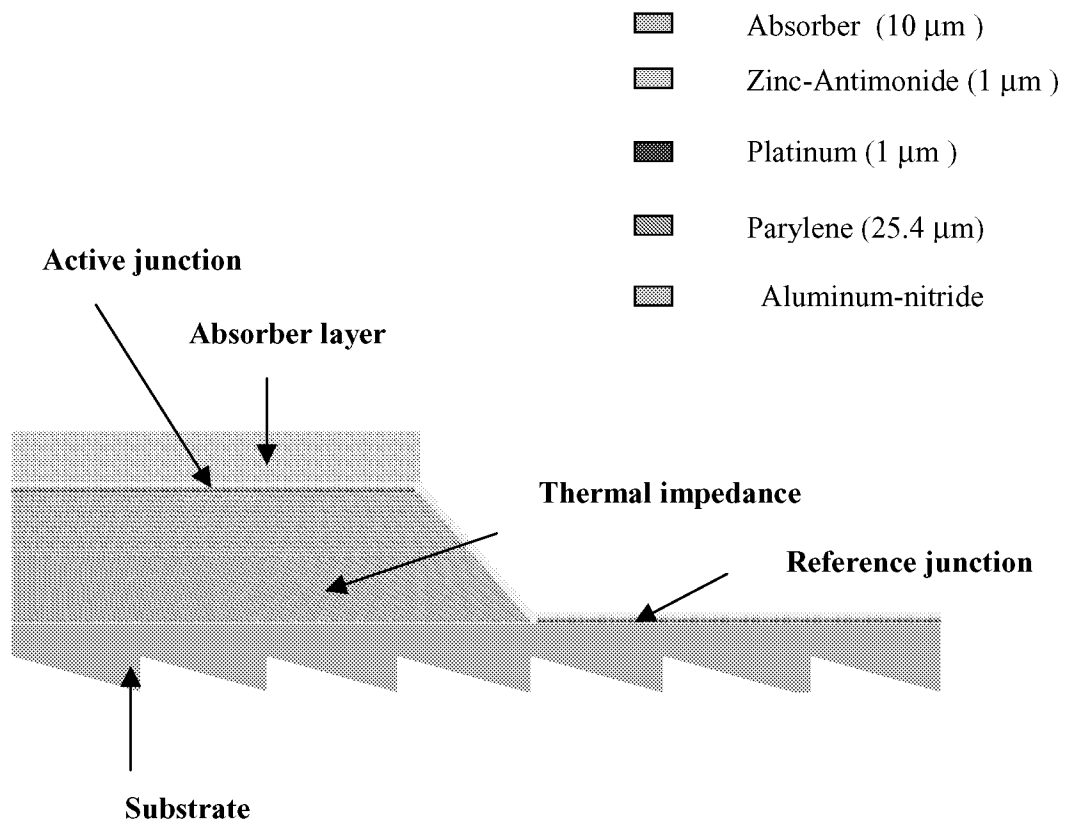


Figure 2.8. Profile of the thermocouple design.

Table 2.1. Nominal material and thermal properties of the thermopile, the absorber layer and the heat sink.

	Mass density (kg/m <sup>3</sup> )	Specific heat (J/kgK)	Conductivity (W/mK)	Electrical resistivity ( $\Omega$ m)
Platinum arm	21450	133	71.6	$10.6 \cdot 10^{-8}$
Zinc Antimonide arm	6880	200	60	$12.5 \cdot 10^{-4}$
Aluminum nitride heat sink	3260	800	165	$10^9$
parylene thermal resistance	1289	712	0.084	$8.8 \cdot 10^{14}$
absorber layer (Chemglaze)	1400	669	0.209	-

The expected performance of the thermopiles is a high sensitivity ( $> 0.27 \mu\text{V}/\text{W}/\text{m}^2$ ), a fast time response ( $< 20 \text{ ms}$ ), and a low electrical resistance ( $< 30 \text{ k}\Omega$ ).

#### 2.2.5 Parameters available to improve the sensitivity of the device

The dimensions, the conductivity, and the geometry of the parylene resistance layer are parameters available for improving the sensitivity of the device. This implies the need for a compromise between the time response and sensitivity. A thicker resistance layer gives a better sensitivity but the time response is then degraded because of added thermal mass and resistance. Additionally, the absorber has to be sufficiently thick to absorb the irradiant power and at the

same time sufficiently thin not to influence the time constant. Also, up to a point, the spectral response is likely to be flatter if the absorber layer is thicker. A compromise must also be found between the sensitivity and time response.

To summarize, the parameters which could be used to improve the thermopile design are:

1. the thermal resistance layer material and its geometry,
2. the dimension of the gap between the active and the reference junctions, and
3. the thickness of the absorber layer.

The next chapter is dedicated to describing the finite element model created to study the time response and sensitivity of the thermopiles. More details are given about the parameters used to achieve an optimized design.

### **3. Finite Element Model**

A numerically approximated description of the thermal behavior of the thermopile must be formulated due to the complexity of the geometry; no closed form analytical solution is available. We chose the finite element method over the finite difference method to conduct this study because of the trapezoidal profile of the detector. It would have been difficult to accurately model the triangular edge with the rectangular grid required of the finite difference method. Using the commercial product ALGOR, we are able to treat both the steady-state and the transient aspects of the analysis. For consistency, some of the finite element results have been checked with a combination of two other commercial finite element commercial packages PATRAN and ABAQUS.

#### **3.1 Finite Element Formulation**

The finite element method was originally developed for structural analysis, and it has since been adapted to the field of heat transfer analysis. The objective is to find an approximate solution of a given boundary-value problem. The basis of this method is the representation of the region of calculation by finite subdivisions (subvolumes), where a spaced grid of nodes replaces a conduction region. These nodes are the location where the solution is computed. The finite subdivisions are called finite elements and they can have different shapes, thus giving more flexibility to the method compared to the finite difference method. The collection of finite elements and nodes is called a finite element mesh. Continuous variables such as temperature can be represented over the finite element by a linear combination of polynomials called interpolation functions. These functions

depend upon the values at nodes only. Figure 3.1 shows a two-dimensional region subdivided into finite elements.

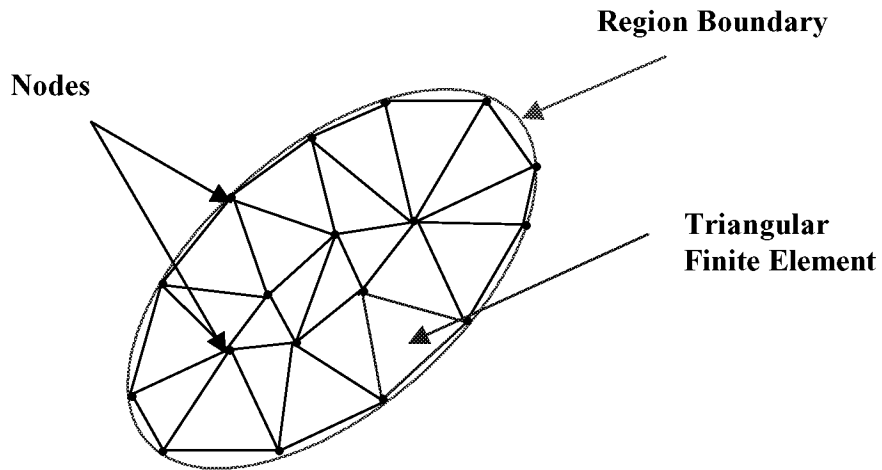


Figure 3.1. Two-dimensional region subdivided in finite elements.

Note that for one-dimensional problems the union of the sub-domains matches exactly with the given domain, but this may not be true for two- and three-dimensional problems, as can be seen in Figure 3.1. One way to improve the representation of the solution space by the collection of assembled finite elements is to increase the number of elements or to increase the order of the interpolation functions (or number of nodes per element).

The governing equation expressing conservation of energy for a system with no heat source on a domain  $D$  is

$$\nabla^2 T = \frac{\rho c}{k} \frac{\partial T}{\partial t} = \frac{1}{\alpha} \frac{\partial T}{\partial t} \quad , \quad (3.1)$$

where  $T$  (K) is the temperature,  $t$  (s) is time,  $k$  (W/mK) is the thermal conductivity,  $\rho c$  is the thermal

capacity ( $J/m^3K$ ) and  $\alpha = \frac{k}{\rho c}$  ( $m^2/s$ ) is the thermal diffusivity.

Boundary conditions such as temperature or imposed surface heat flux, including the adiabatic condition, may be imposed on domain D. Figure 3.2 depicts these three types of boundary conditions. In the figure, the sub-area  $S_1$  has a constant temperature boundary condition applied,  $S_2$  a constant heat flux, and  $S_3$  is insulated.

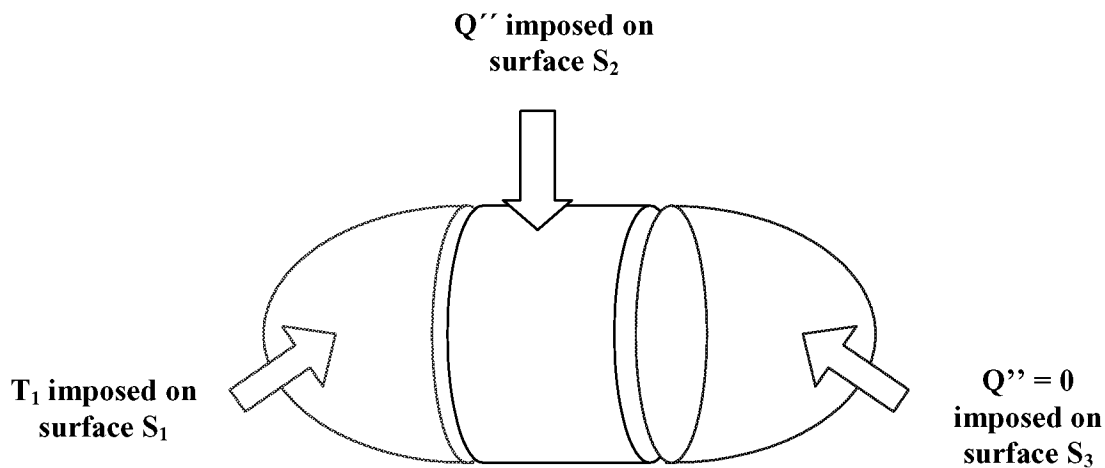


Figure 3.2. The types of available boundary conditions in ALGOR

A classical solution of the problem (strong formulation) is a function  $T$  defined on  $D$ , such that  $T$  satisfies the given differential equation, Equation 3.1, everywhere in  $D$  and the temperature boundary conditions. The finite element solution of the problem is based on the Galerkin approximation which uses interpolation functions defined on the different subdivisions of the domain  $D$ . The resulting formulation gives a system of algebraic equations to be solved. Several methods of integration can be used to solve these equations. In transient problems, the global formulation provides a set of equations for determining the time dependence, and calculations are

then made possible using an initial condition. For steady-state analysis one set of spatial conditions represents the solution. Details about finite element formulation can be found in Gebhart [1993] and Reddy [1993].

## **3.2 Finite Element Software**

The finite element commercial package ALGOR is used to predict the response of the thermopile radiation detector to different boundary and initial conditions. This section focuses on the software itself, its basic operation modes, its capabilities and the numerical integration method it uses.

### **3.2.1 ALGOR operation modes**

ALGOR is used as the pre-processing, processing and post-processing software. First, it prepares the model for the analysis. After having specified the nature of the analysis as either steady-state or transient, ALGOR enables one to build the geometry, define the physical properties, and specify the boundary conditions such as a fixed temperature, or a surface with radiation, convection or insulation. The definition of the different material properties is made possible by assigning a different color to each different type of material. It must also be noted that the heat flux boundary condition is applied manually (node by node) during the pre-processing stage. ALGOR also provides the mesh of the model by meshing the different regions into finite numbers of nodal elements. Two-dimensional thermal elements are 3- or 4-node elements formulated in the Y-Z plane. Meshes can be uniform across the model or concentrated around critical regions. ALGOR also displays and verifies all data prior to executing the analysis. The pre-processing (including the decoder and the feature called Timeload Program) is accomplished by specifying the transient parameters, the heat flux boundary conditions and the format of the solution. The decoder then creates a file called Filename which is the processor input file. The transient heat transfer processor (SSAP11) processes the model.

The processor ALGOR performs the analysis by solving the system of algebraic equations representing the model and providing an output file with the nodal results called Filename.1. The

post-processor displays the nodal results. Unfortunately the transient solution could not be displayed in the desired format, and so a program was developed in Matlab which reads the nodal file, performs different kinds of calculations (averages and errors), and plots the transient solution. Figure 3.3 summarizes the different stages used to create the model and display the results.

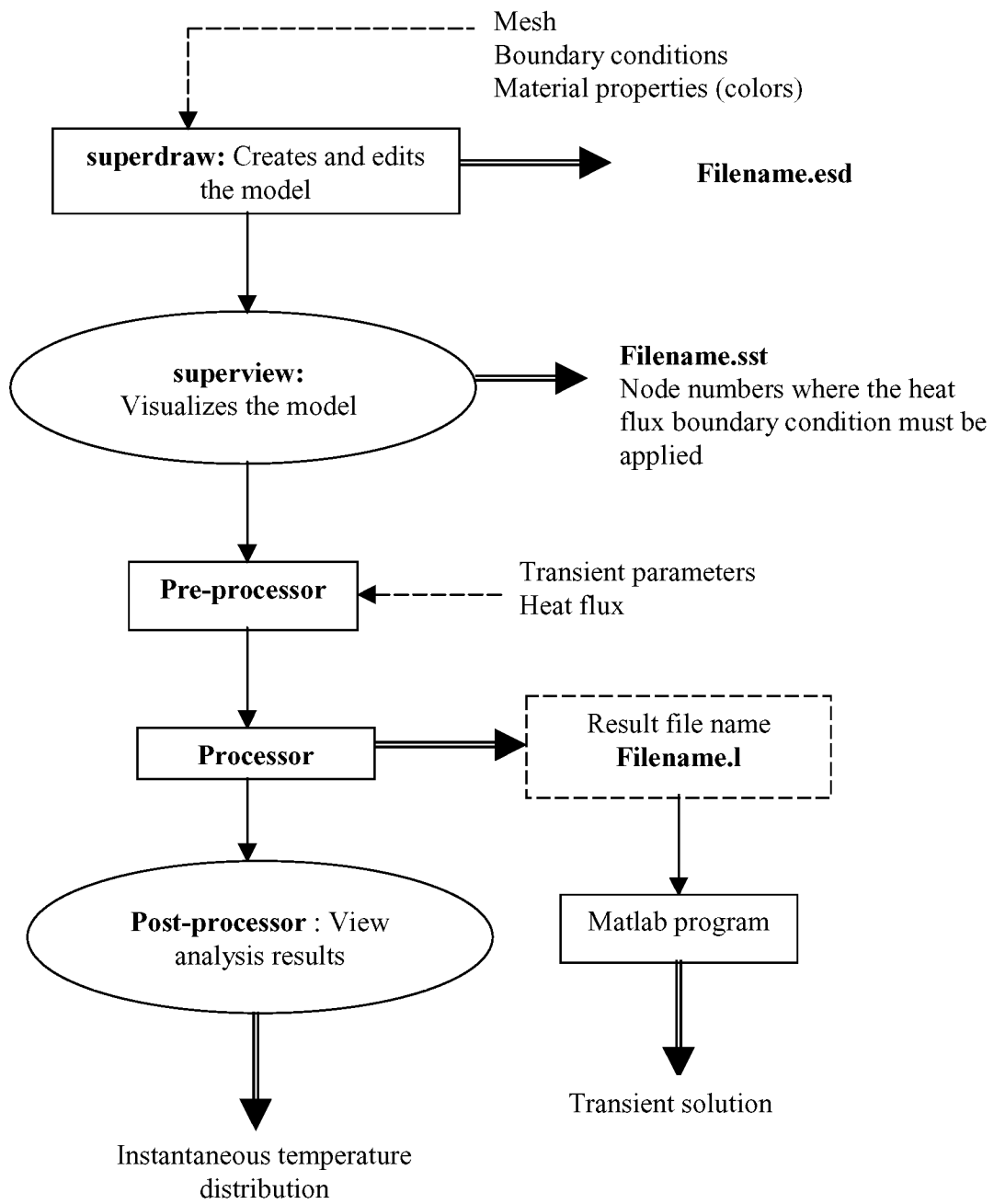


Figure 3.3. Summary of stages used in ALGOR

### 3.2.2 Capabilities of and comments on the software

Comments and criticisms made below about ALGOR are usually made in comparison with the finite element software package PATRAN (Version 2-5).

ALGOR allowed the development of a well-defined finite element mesh in the model. A model made of 3677 elements and 3901 nodes has been created in two dimensions. Element lengths of less than a 1  $\mu\text{m}$  exist in the critical regions such as the active junction of the thermopile. The elements used in the analysis are two-dimensional, second-order, four-node quadrilateral elements specific to heat conduction. Since these elements are second-order, their interpolation functions are quadratic. Quadratic functions are justified over higher-order polynomials since the mesh density is high. Figure 3.4 shows the refined two-dimensional mesh of the part of the thermocouple including the active junction obtained using ALGOR. Comparison of Figure 3.4 with Figure 2.8 clearly established the location of the mesh with respect to the detector geometry. This mesh is acceptable since the elements are undistorted rectangular shaped.

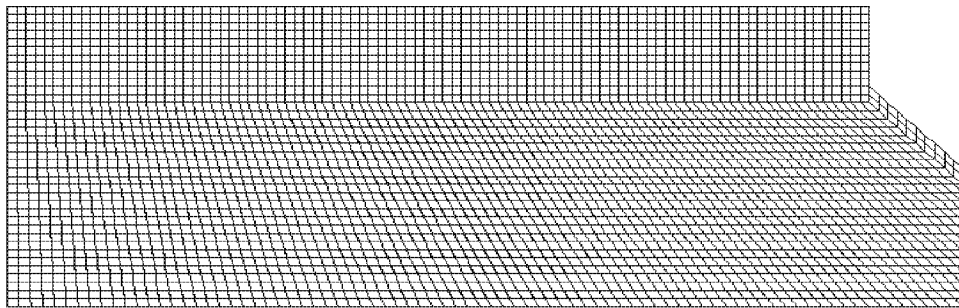


Figure 3.4. Example of a two-dimensional mesh created on ALGOR.

The ALGOR transient thermal processor was used to perform the transient heat transfer analysis. It is a very flexible tool in that, though it does not automatically select the time increment so that steady state is reached, the user may define his own time increment and, even more important, the number of steps used (up to a thousand). The drawback is that a study of the value of the time step must first be made to know when the converged solution is reached. If this step could be made automatic the engineering cost of the analysis would be reduced because the converged solution would be found in a minimum number of iterations. The time integration used by ALGOR is done with an unconditionally converging scheme called Wilson Theta. More details on this analysis can be found in the ALGOR manual [1993].

Several other limitations of the software can be mentioned after using it and comparing it with PATRAN. For example, the default elements are quadrilateral elements and there is no way to use triangular elements with total control of their length or number. Another drawback of ALGOR compared to PATRAN is the fact that the heat flux boundary conditions have to be specified manually. When a model has a complex geometry, a boundary edge may not be numbered sequentially and thus it becomes tedious to enter the node numbers one by one to apply the heat flux boundary condition. Additionally an incorrect node number may be entered by mistake with the result that the data must be entered all over again. Finally, the post-processor ALGOR is really not flexible for displaying results. For example, it is unable to display the transient temperature response of a specified node or group of nodes.

### **3.3 The Thermal Models**

This section examines two thermal models, a one-dimensional model and a two-dimensional model of the thermocouple junction pair. The assumptions and approximations implied when using such models are given. Additionally both models are validated by presenting the results of the derivation of an analytical steady-state solution for the one-dimensional model, and by showing that

the results given by another finite element software package (PATRAN-ABAQUS) confirm the two-dimensional model.

### 3.3.1 General assumptions and approximations

Due to the thermopile environment (vacuum), conduction and radiation are the only modes of heat transfer present in the analysis. Because the cavity and the heat sink where the detector is mounted are assumed to be maintained at a temperature of 311 K, we expect the heat transfer through radiation, other than that due to the incident heat flux from the scene, to be small, and thus negligible in the current analysis.

Due to the high input impedance of the amplifier used to sense the thermopile voltage, we assume that no current flows through the thermocouple junctions. Thus no self-heating nor other thermoelectric effects are taken into account and the volumetric heat source  $q'''$  is assigned a value of  $0 \text{ W/m}^3$  in the energy equation.

Since only small ranges of temperatures are encountered, it is assumed that material properties such as conductivity do not vary with temperature.

As far as the boundary conditions are concerned, the heat sink is modeled by a fixed, known temperature at the interface of the pixel with the aluminum-nitride substrate. This condition gives the substrate the property of a heat sink. Assuming that the incident scene energy striking the absorber is uniform, it is modeled as a net uniformly distributed heat flux boundary condition. This imposed heat flux is assumed normal to the top of the pixel (the absorber). It represents the incident radiation coming from the Earth less the component emitted from the surface of the pixel.

The gap between adjacent pixels is assumed to thermally insulate each thermocouple junction pair of the linear-array; thus the two edges of the pixel are insulated. Since it is not yet clear what kind of conditions exist on to the remaining boundaries of the pixel; it is assumed that they are also insulated. This is at least partially justified because the pixel array is embedded in the cavity mirror wall. Figure 3.5 summarizes the boundary conditions applied to the pixel.

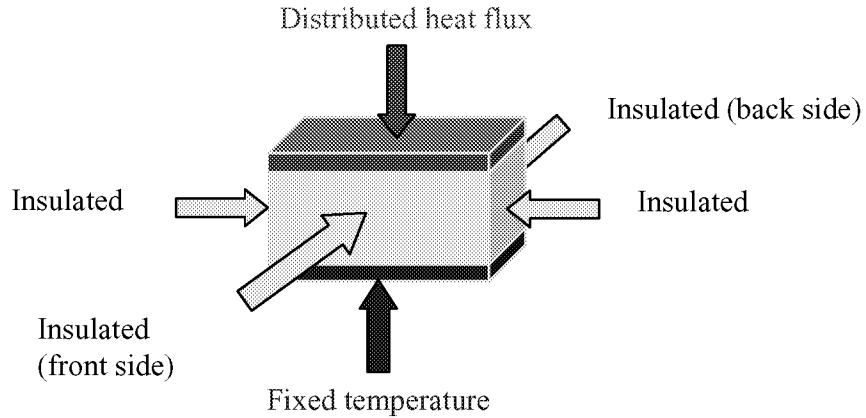


Figure 3.5. Boundary conditions applied to the pixel

The pixel design shown in Figure 3.5 is geometrically three-dimensional. However, the symmetry in the boundary conditions and an aspect ratio such that the two-dimensional heat transfer effects at the edges may be ignored encourages preliminary consideration of a one-dimensional model.

### 3.3.2 One-dimensional model

The one-dimensional model is simplified to represent the active junction only. It consists of two plane boundaries: at one plane boundary a known heat flux is imposed and the other is considered to be at a known constant temperature. The initial temperature throughout the thermopile model is set to the temperature of the heat sink. Figure 3.6 represents this model and its boundary conditions. The model shown in Figure 3.6 assumes that the active junction is infinite in size (thus the neglect of edge effects) and that the reference junction (not represented in this model) mounted on the heat sink and isolated from the incident energy coming from the Earth scene, remains at the

temperature of the heat sink. This model is an ideal case where the loss of energy in the second dimension is neglected.

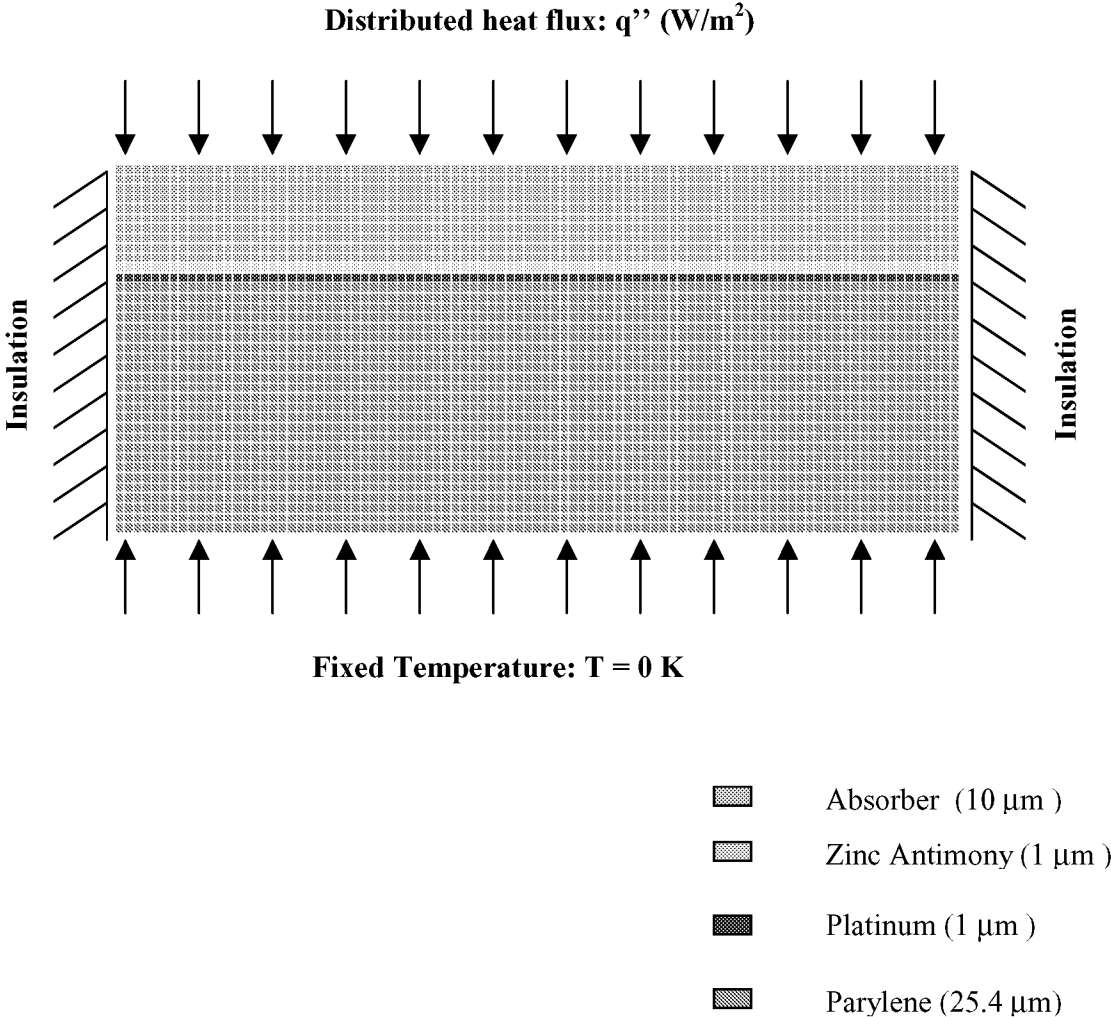


Figure 3.6. One-dimensional model of the active-junction

One major problem encountered when specifying the boundary conditions of the model is the resulting minuscule variations in predicted temperature. A 10  $\mu\text{K}$  temperature difference between the top and the bottom of the model may be anticipated. A simple model can be studied to make a quick prediction of the temperature at the top of the solution space assuming that the heat conduction is one-dimensional with an average thermal conductivity of 3.54 W/mK through a uniform material with 37.5  $\mu\text{m}$  thickness. Fourier's law of heat conduction in one dimension is written

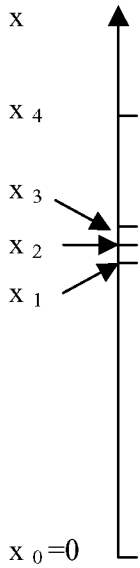
$$q'' = -k \frac{dT}{dx} \quad (3.2)$$

After integration and taking into account the heat flux boundary condition of  $q'' = 1 \text{ W/m}^2$ , which is approximately the heat flux due to an Earth scene, Equation 3.2 gives

$$\Delta T = \frac{q'' \Delta x}{k} = \frac{1.0 \text{ (W/m}^2) \times 3.7510^{-5} \text{ (m)}}{3.54 \text{ (W/Km)}} = 10 \mu\text{K} .$$

So if we fix the bottom of our model to a temperature of 311 K, we can expect a temperature range between 311 and 311.00001 K. Unfortunately, these eight significant figures are meaningless and can never be measured or even calculated to this accuracy due to round-off error. In fact, the ALGOR finite element software gives a maximum of four significant figures. The solution to this problem is to solve for a new temperature variable,  $T' = T - 311$ . This translation shifts the above temperature range to 0 to  $10 \times 10^{-6}$  K. The new constant-temperature boundary condition at the bottom of the model is  $T' = 0 \text{ K}$ .

Validation of the one-dimensional model is made by a one-dimensional heat transfer mathematical model. The one-dimensional steady-state analytical solution can easily be derived. By defining the four different temperature distributions corresponding to each of the four layers of material as  $T_1$  for the parylene,  $T_2$  for the platinum,  $T_3$  for the zinc-antimony and  $T_4$  for the Chemglaze absorber, with their respective conductivities ( $k_1, k_2, k_3, k_4$ ) and the heat flux boundary condition  $q''$ , the problem can be formulated as shown schematically in Figure 3.7.



The equations of steady-state heat transfer are

$$\frac{\partial^2 T_i}{\partial x^2} = 0, \quad x_{i-1} < x < x_i,$$

and the boundary conditions are

$$T_1(x_0 = 0) = 0 \text{ K},$$

$$T_i(x_i) = T_{i+1}(x_i), \quad i = 1, 2, 3, 4$$

$$k_i \left( \frac{\partial T_i}{\partial x} \right)_{x=x_i} = k_{i+1} \left( \frac{\partial T_{i+1}}{\partial x} \right)_{x=x_i}, \quad i = 1, 2, 3, 4$$

$$k_4 \left( \frac{\partial T_4}{\partial x} \right)_{x=x_4} = q''.$$

Figure 3.7. Schematic representation of the one-dimensional steady-state formulation

The solutions  $T_i$ ,  $i=1, \dots, 4$ , for each material are then

$$T_1(x) = \frac{q''}{k_1} x$$

$$T_2(x) = \frac{q''}{k_2} x + x_1 q'' \left( \frac{1}{k_1} - \frac{1}{k_2} \right)$$

$$T_3(x) = \frac{q''}{k_3} x + x_2 q'' \left( \frac{1}{k_2} - \frac{1}{k_3} \right) + x_1 q'' \left( \frac{1}{k_1} - \frac{1}{k_2} \right)$$

and

$$T_4(x) = \frac{q''}{k_4} x + x_3 q'' \left( \frac{1}{k_3} - \frac{1}{k_4} \right) + x_2 q'' \left( \frac{1}{k_2} - \frac{1}{k_3} \right) + x_1 q'' \left( \frac{1}{k_1} - \frac{1}{k_2} \right) \quad (3.3)$$

According to these analytical results we can evaluate the sensitivity of the detector made of

a single infinite pixel. The steady-state sensitivity of a detector, which is its ability to sense a unit amount of radiant energy arriving at its surface, is defined as the ratio of the detector steady-state response to the amount of energy arriving at the detector. The steady-state response of the detector can be evaluated by calculating the temperature difference between the heat sink ( $x = 0$ ) and the active junction ( $x = x_2$ ) which is

$$\Delta T_{\text{active junction}} = T_2(x_2) - T_1(x_0) = T_2(x_2) = \frac{q''}{k_2} x_2 + x_1 q'' \left( \frac{1}{k_1} - \frac{1}{k_2} \right) = 3.024 \cdot 10^{-4} \text{ K}.$$

If a Seebeck coefficient of  $920 \mu\text{V/K}$  is used, the sensitivity of the thermocouple is

$$\text{Sensitivity} = \frac{S_{\text{Zn-Sb}} \Delta T_{\text{active junction}}}{q''} = 0.278 \mu\text{V/W/m}^2.$$

The transient one-dimensional analytical solution of the problem is much more difficult to solve because several different material layers are used. An analytical solution can be found if it is assumed that the model is made of a single material. The transient heat conduction equation for a one-dimension problem is

$$\frac{\partial^2 T}{\partial x^2} = \frac{1}{\alpha_{\text{eff}}} \frac{\partial T}{\partial t}, \quad (3.4)$$

where  $\alpha_{\text{eff}}$  ( $\text{m}^2/\text{s}$ ) is the effective diffusivity of the material.

The heat flux and the temperature boundary conditions along with the initial conditions can be described as

$$T(x_0, t) = 0, \quad x = 0, \quad t > 0, \quad \text{homogeneous boundary condition,}$$

$$T(x, 0) = 0, \quad 0 \leq x \leq x_4, \quad t = 0, \quad \text{homogeneous boundary condition,}$$

$$k_{\text{eff}} \left. \frac{\partial T}{\partial x} \right|_{x=x_4} = q'', \quad x = x_4, \quad t > 0, \quad \text{nonhomogeneous boundary condition,}$$

where the heat flux  $q''$  and the two temperature boundary conditions are known.

To use the method of separation of variables all of the boundary conditions must be homogeneous. So let us look for a solution of the form

$$T(x, t) = \psi(x, t) + \phi(x). \quad (3.5)$$

With the substitution of Equation 3.5, Equation 3.4 becomes

$$\frac{\partial^2 \psi}{\partial x^2} = \frac{1}{\alpha_{\text{eff}}} \frac{\partial \psi}{\partial t} \quad , \quad (3.6a)$$

$$\frac{\partial^2 \phi}{\partial x^2} = 0 \quad (3.6b)$$

and the boundary conditions are equivalent to

$$\psi(0, t) = 0 \quad \text{and} \quad \phi(0) = 0 \quad , \quad (1)$$

$$\left. \frac{\partial \psi}{\partial x} \right|_{x=x_4} = 0 \quad \text{and} \quad \left. \frac{\partial \phi}{\partial x} \right|_{x=x_4} = \frac{q''}{k_{\text{eff}}} \quad , \quad (2)$$

$$\psi(x, 0) + \phi(x) = 0 \quad . \quad (3)$$

The boundary conditions relative to Equation 3.6(a) are now all homogeneous. Separation of variables may be used to solve this equation. That is,  $\psi(x, t) = X(x)T(t)$  so that Equation 3.6(a) becomes

$$\frac{1}{X} \frac{\partial^2 X}{\partial x^2} = \frac{1}{\alpha_{\text{eff}} T} \frac{\partial T}{\partial t} \quad . \quad (3.7)$$

Equation 3.7 is of the form  $f(x) = g(t) = -\lambda^2$  so that after integration it gives

$$X(x) = a \cos(\lambda x) + b \sin(\lambda x) \quad \text{and} \quad T(t) = c e^{(-\alpha_{\text{eff}} \lambda^2 t)} \quad ,$$

where a,b,c are integration variables. Application of the boundary conditions (1) and (2) yields

$$\psi(x, t) = \sum_0^{\infty} a_n \sin(\lambda_n x) e^{-\alpha_{\text{eff}} \lambda_n^2 t} \quad \text{with} \quad \lambda_n = (2n+1) \frac{\pi}{2x_4} \quad .$$

The integration of  $\phi$  gives  $\phi(x) = \frac{q''}{k_{\text{eff}}} x$  .

To evaluate the  $a_n$  the fact that the functions  $\sin(\lambda_n x)$  are a complete set of orthogonal functions is used. Multiplying  $\psi(x, t)$  by  $\sin(\lambda_m x)$ , integrating the result from 0 to  $x_4$ , and then invoking the orthogonality of the circular functions yields

$$a_n = \frac{-\int_0^{x_4} \frac{q''x}{k_{\text{eff}}} \sin(\lambda_n x) dx}{\int_0^{x_4} \sin^2(\lambda_n x) dx} = \frac{-2q''(-1)^n}{k_{\text{eff}} \lambda_n^2 x_4}.$$

Finally the transient response of this “effective material” can be written as

$$T(x, t) = \sum_{n=0}^{\infty} \frac{-2q''(-1)^n}{k_{\text{eff}} \lambda_n^2 x_4} \sin(\lambda_n x) e^{-\alpha_{\text{eff}} \lambda_n^2 t} + \frac{q''x}{k_{\text{eff}}} \quad \text{with} \quad \lambda_n = \frac{(2n+1)\pi}{2x_4}. \quad (3.8)$$

The plot of this function shows that for the solution converges before the ten first modes (n) of the sum. It represents the analytical solution of the transient one-dimensional model. This result is used for the validation of the one-dimensional model when the numerical and the analytical solution are compared. The steady-state temperature and the time constant derived from Equation 3.8 are shown in Table 3.1.

### 3.3.3 Two-dimensional model

The two-dimensional model is a more realistic model of the thermocouple junction pair. If we look at the geometry of the thermocouple junction pair it can be understood why the two-dimensional model is essential to our study. Figure 3.8 shows the three-dimensional geometry of the thermocouple.

The ramp of zinc-antimony and parylene connecting the active and reference junctions allows heat conduction in the second dimension. It is also important to study the two-dimensional model because of the boundary conditions: the heat flux boundary condition is imposed on a portion of the boundary (the absorber), while the remainder of the boundary (the ramp and the top of the reference junction) is assumed to be insulated. The model will help to determine the impact of those boundary conditions on the sensitivity of the instrument.

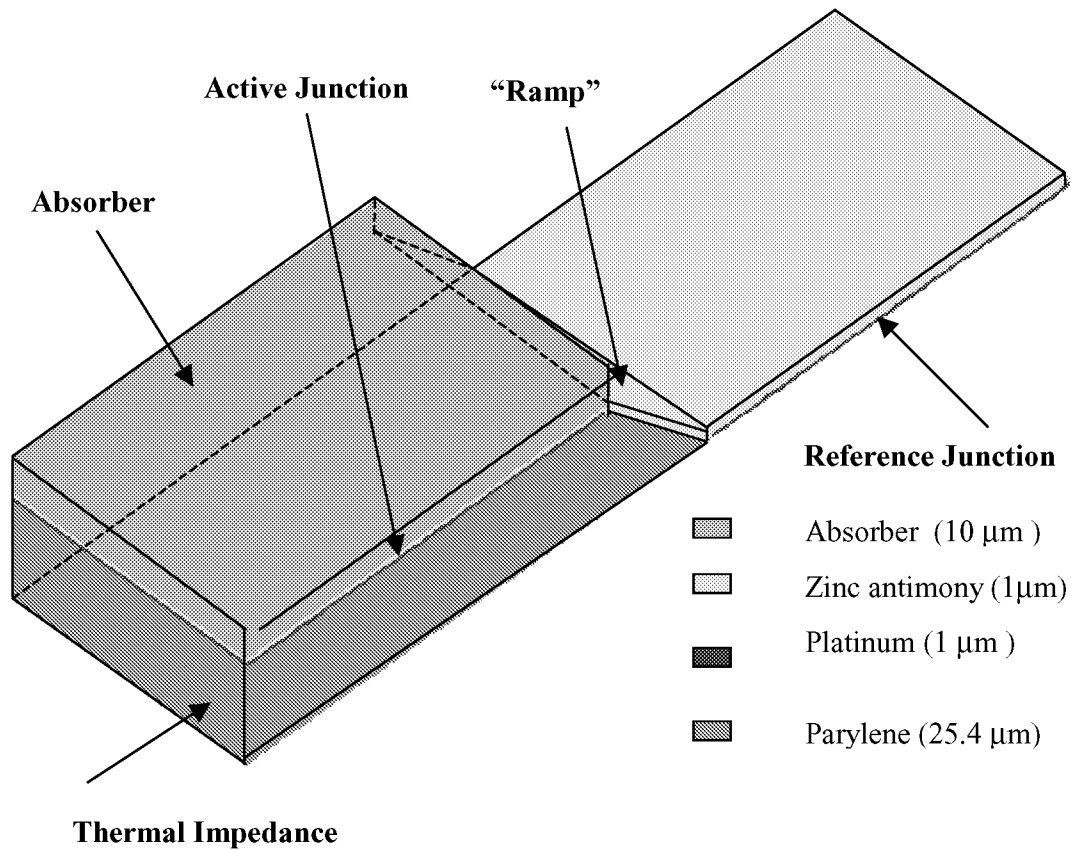


Figure 3.8. Thermocouple three-dimensional geometry.

In the two-dimensional model, the two-thermocouple junction pair is represented so as to take into account lateral heat diffusion and the effect of the slope linking the active and the reference junctions. The assumptions are the same as those used in the one-dimensional model. As far as the boundary conditions are concerned, the same boundary conditions used in the one-dimensional model are again used in the two-dimensional model. The assumption that the top of the reference junction is insulated is justified by the fact that, in the actual device, this junction will be shielded from the incoming radiation by one of the cavity walls. The boundary conditions

are insulated in Figure 3.9. The material properties and the dimensions of the two-dimensional model are given in Figure 3.10.

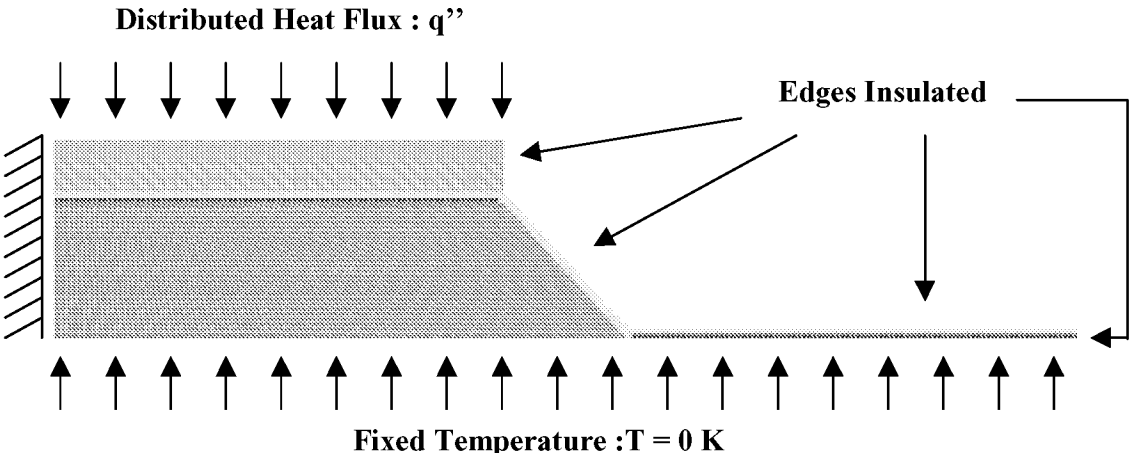


Figure 3.9. Two-dimensional model of the thermocouple boundary conditions.

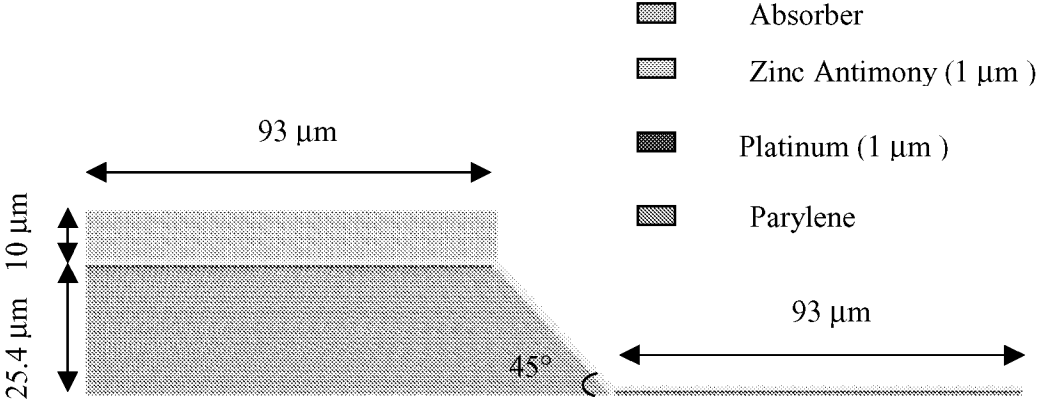


Figure 3.10. Dimensions and materials of the two-dimensional model.

3.3.4 Validation of the models

Validation of the two-dimensional model was made possible through the use of another finite

element software package, PATRAN-ABAQUS. The two-dimensional model used for the comparison differs slightly from the one described in the previous section in that the active junction length is 60  $\mu\text{m}$  instead of 93  $\mu\text{m}$ .

PATRAN-ABAQUS has been used to confirm results in both the one-dimensional and the two-dimensional models. The comparison has been made on the basis of the maximum temperature of the two models. The time response of the one-dimensional and the two-dimensional models has also been computed using the time constant of the associated first-order model. The concept of a “time constant” strictly applies only to lumped systems having a single degree-of-freedom (e.g., spring-mass, thermal capacity-thermal impedance, capacitor-resistor). In the case of the distributed system considered here, whose behavior is at least quasi-first-order, it is convenient to talk about the time constant even though this is not strictly correct. The results are gathered in Table 3.1.

The time constants obtained with PATRAN-ABAQUS are not as accurate as those obtained with ALGOR because the PATRAN-ABAQUS software did not have the capability to provide the time-step refinement. This is why a confidence interval is given for the time constant results obtained with PATRAN-ABAQUS.

Table 3.1. Comparison of the finite element results obtained with ALGOR and PATRAN-ABAQUS

	ALGOR	Analytical (with the approximation of the effective material)	PATRAN-ABAQUS
1-D model	$T_{\max} = 3.50 \times 10^{-4}$ K $\tau = 6.8$ ms	$T_{\max} = 3.49 \times 10^{-4}$ K ( $T_{\max} = 3.50 \times 10^{-4}$ K without any approximation) $\tau = 5.4$ ms	$T_{\max} = 3.50 \times 10^{-4}$ K $6.0 < \tau < 8.0$ ms
2-D model, first configuration <sup>1</sup>	$T_{\max} = 7.86 \times 10^{-5}$ K $\tau = 0.80$ ms	–	$T_{\max} = 7.75 \times 10^{-5}$ K $0.8 < \tau < 1.0$ ms

---

<sup>1</sup> Configuration with a 60- $\mu$ m active junction

As far as the analytical results are concerned only the one-dimensional case has been calculated. The maximum one-dimensional steady-state temperature has been calculated without any approximations and with the approximation of an effective material. In the case where no approximation was made the value of the highest temperature node matches perfectly that of the finite element model. The transient one-dimensional analytical solution has to be approximated. We considered an effective material with a diffusivity  $\alpha_{\text{eff}}$  instead of considering all the material layers. So the time constant is obtained by computing the model given by Equation 3.9 for the junction node ( $x = 26.4 \mu\text{m}$ ), fitting to this model a “best-fit” curve as shown in Figure 4.13, and calculating the time constant associated with the best-fit curve. The time constant found agrees with the finite element software ALGOR within 21 percent, which is acceptable considering the approximation of the effective material.

The temperature distribution inside both models is validated: ALGOR results are fully confirmed both by PATRAN-ABAQUS and by the analytical solution for the one-dimensional model computed using Equation 3.4. As far as the time response of the models is concerned, we find a slight disagreement. This difference between the time constants is due to a bigger time step increment using PATRAN-ABAQUS than using ALGOR. The degree of agreement between the two models tends to validate the finite element model obtained with ALGOR.

The temperature distribution inside the device once steady-state conditions are reached is shown in Figures 3.11 and 3.12. The temperature distribution has been computed with both of the finite element software packages and shows essentially the same isotherms.

A parametric study involving different geometric parameters and using the validated ALGOR models is presented in the next chapter.

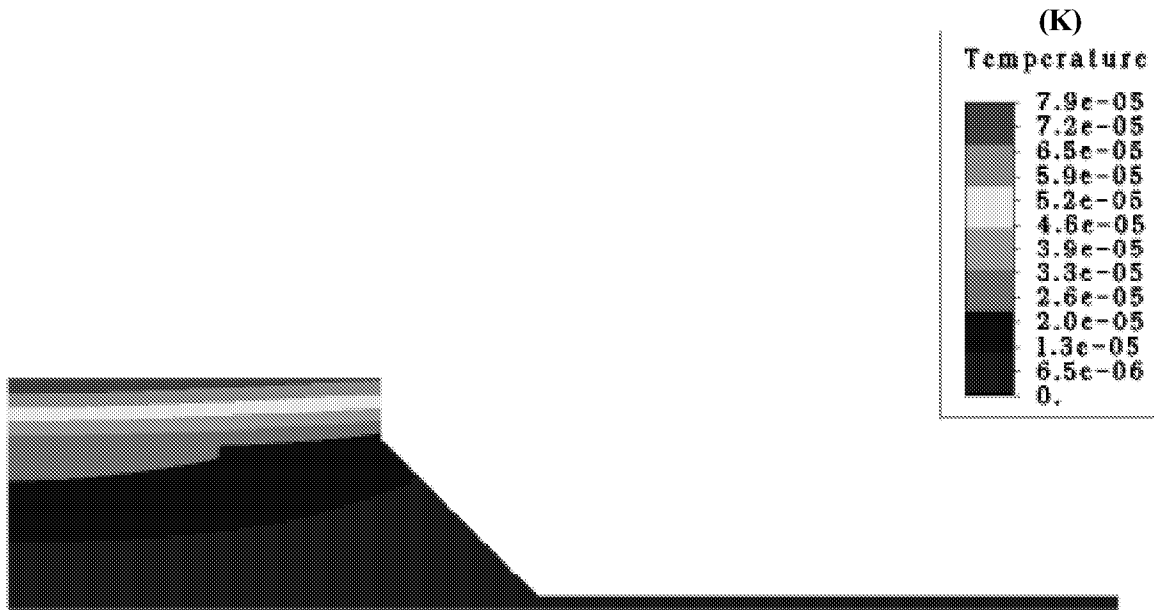


Figure 3.11. Temperature distribution obtained with ALGOR

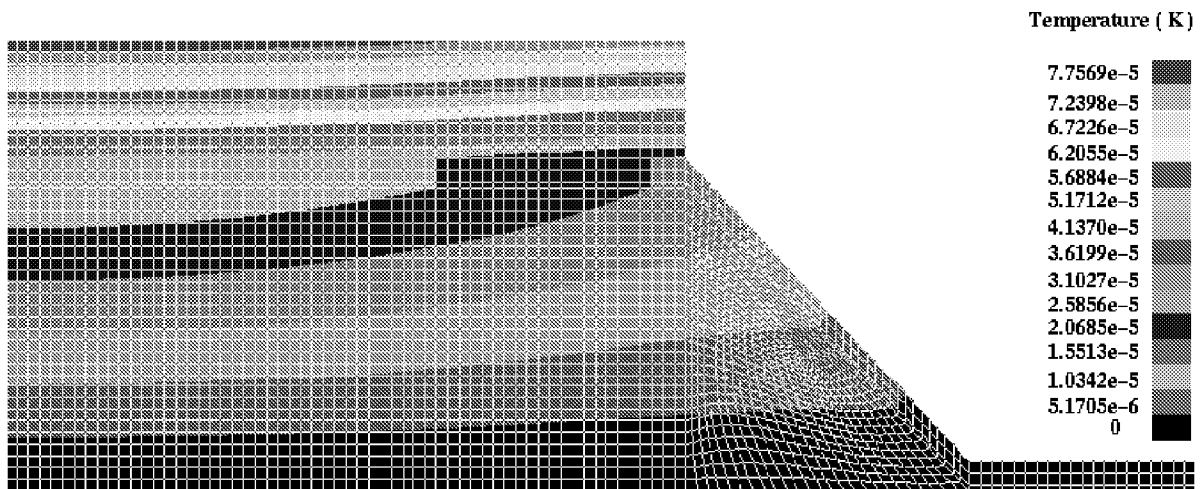


Figure 3.12. Temperature distribution obtained with PATRAN-ABAQUS

## 4. Results and Discussion

To familiarize the reader with the history which motivated the current effort one must go back a year and a half, when Dr. Mahan met with Larry Langley, the owner Vatell Corporation. Vatell develops, manufactures and sells thermopile heat flux micro-sensors based on new patented technologies. The performance characteristics of these sensors, including the sensitivity, the time response and the dimensions were very promising. In February, 1996, the Thermal Radiation Group (TRG) of Virginia Tech entered into an agreement with Vatell, in which the TRG would provide a dynamic thermal model of the original thermopile design. At that time a parametric study was performed to optimize the sensitivity of the device. All the results from this original thermopile design can be found in a report submitted for the “Diplôme d’études approfondies (DEA)” to the Institut Universitaire des Systèmes Thermiques Industriels in June, 1996 [Weckmann, 1996]. In August, 1996, Dr. Mahan proposed to NASA a new variation on the Vatell sensor in a competition for the detector to be used on the GERB instrument. This proposal was accepted and the current efforts are aimed at providing the GERB instrument with a highly sensitive and reliable sensor.

To summarize in a few words, the goals are to predict the sensitivity and the time response characteristics of the latest sensor design and to optimize this design by using the dynamic electrothermal model in a parametric study. All of the results presented in this chapter are analytical and so have to be used with full knowledge of their limitations. They are offered here in support of the experimental results in a way that permits the manufacturing process to be optimized.

This chapter is organized into three parts. In the first part results of the one-dimensional and

two-dimensional models, including the sensitivity and the time response, are presented and are compared to the experimental results obtained by Vatel Corporation. In the second part, by exercising different model boundary conditions and changing critical parts of the geometry, a first attempt at design optimization is made. Finally, in the third part we investigate the basic assumption inherent to the model that no current flows in the device. This last part raises many questions, unanswered for the most part, but nevertheless interesting from the physical point of view.

## **4.1 One-Dimensional and Two-Dimensional Model Results**

### 4.1.1 Temperature distribution

The steady-state temperature distributions calculated with the thermocouple one-dimensional and two-dimensional models are displayed in Figures 4.1 and 4.2, respectively. The one-dimensional model represents an ideal thermocouple in which the active junction is modeled as infinite in lateral dimensions. This is the ideal configuration for the thermocouple design because no heat is transferred in a second dimension and so the sensitivity is maximized. Following theory, the isotherms are perpendicular to the different layers of material in this model while the temperature distribution reflects the symmetry of the geometry and the boundary conditions. The heat is conducted only in the vertical plane. Most of the temperature gradient occurs in the thermal impedance layer of parylene, as expected.

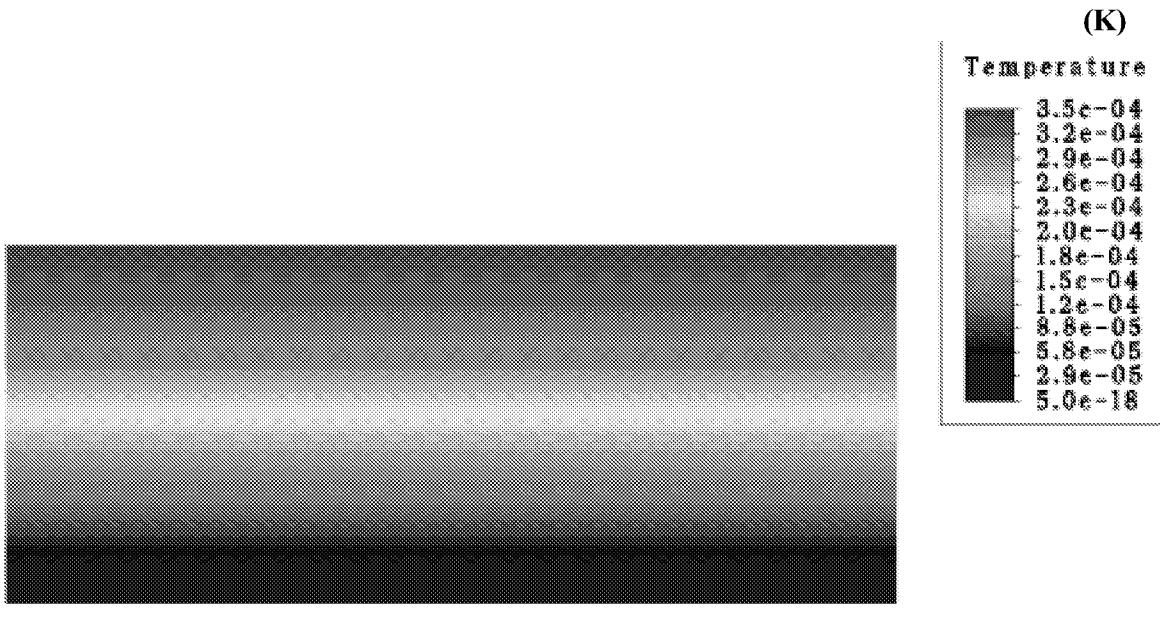


Figure 4.1. The steady-state one-dimensional temperature distribution for the boundary conditions shown in Figure 3.6.

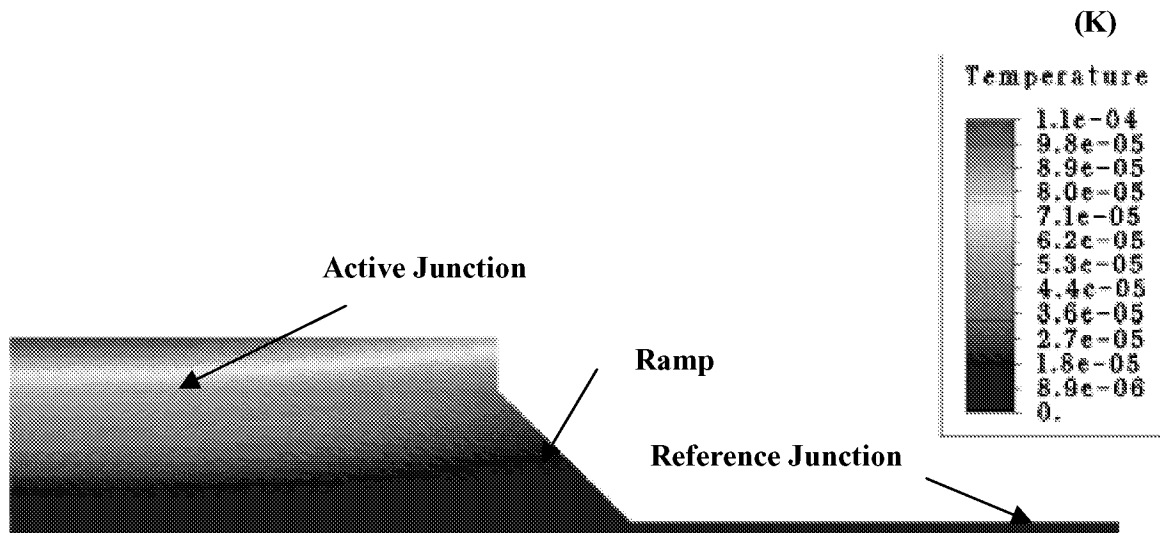


Figure 4.2. The steady-state two-dimensional temperature distribution corresponding to the boundary conditions of Figure 3.9

In the two-dimensional model, the isotherms are no longer perpendicular to the different layers of material in the region near the ramp connecting the active junction and the reference junction. The ramp permits divergence of the temperature field from the vertical; the heat flux is partially conducted in the horizontal plane as a result of the ramp. This effect and the fact that the heat sink is twice as big as the heat source (active junction) allow a smaller average temperature difference between the active junction and the reference junction than in the case of the one-dimensional model. For this reason it is predicted that the two-dimensionality of the thermocouple will decrease its sensitivity. The following provides more details about the sensitivity.

#### 4.1.2 Sensitivity

A numerical sensitivity study has been conducted so as to quantify the ability of the thermocouple to sense a unit amount of radiant energy arriving at the active junction. Used were a nominal value of the Seebeck coefficient for the zinc-antimonide couple  $S_{\text{ZnSb-Pt}}$ , equal to  $920 \mu\text{V/K}$ , and a heat flux input  $q''$  equal to  $1 \text{ W/m}^2$ . The sensitivity ( $\text{V/Wm}^{-2}$ ) can be expressed as

$$\text{Sensitivity} = \frac{S_{\text{ZnSb-Pt}} \Delta T}{q''} \quad , \quad (4.1)$$

where  $\Delta T$  (K) is the temperature difference between the active and reference junctions.

According to the literature [Pollock, 1985] the sensitivity of a thermocouple device can be evaluated by measuring the difference in temperature between the active, or “hot,” junction and the reference, or “cold,” junction. In the current case the thermocouple device is slightly different from the usual design of thermocouples due to the extremely small size of its junctions. The ratio,  $r$ , of the combined length of the junction to the length of the connecting leads has a value of five in the current design, whereas usually thermocouples have a ratio close to zero. This difference is illustrated in Figure 4.3.

The problem is to decide what temperature to assign to a junction in the case where the temperature is not uniform along the length of the junction, as is the case for the two-dimensional model. Figure 4.4 shows the temperature profile along the active junction. An overall temperature difference of  $1.213 \times 10^{-5} \text{ K}$  is predicted between the two ends of a  $60\text{-}\mu\text{m}$  active junction, compared

to a mean temperature difference between the active and reference junctions of  $2.228 \times 10^{-5}$  K. The mean junction temperature is obtained by averaging the temperature along the nodes lying within the plane of the junctions. Thus the temperature gradient represents 54 percent of the mean temperature.

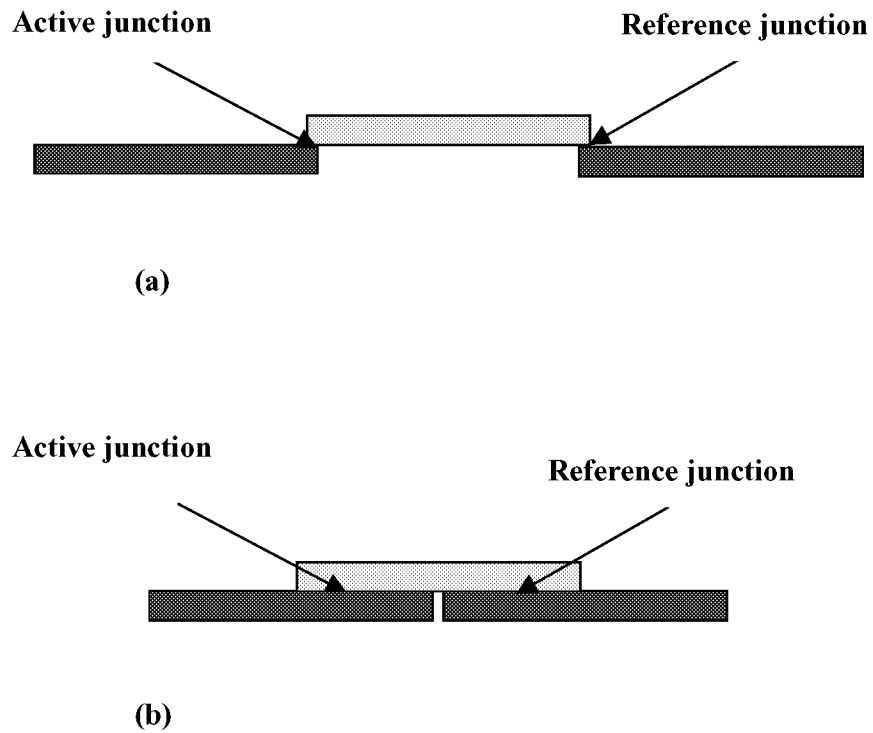


Figure 4.3. Comparison between different type of junctions: (a) the typical design and (b) the current design.

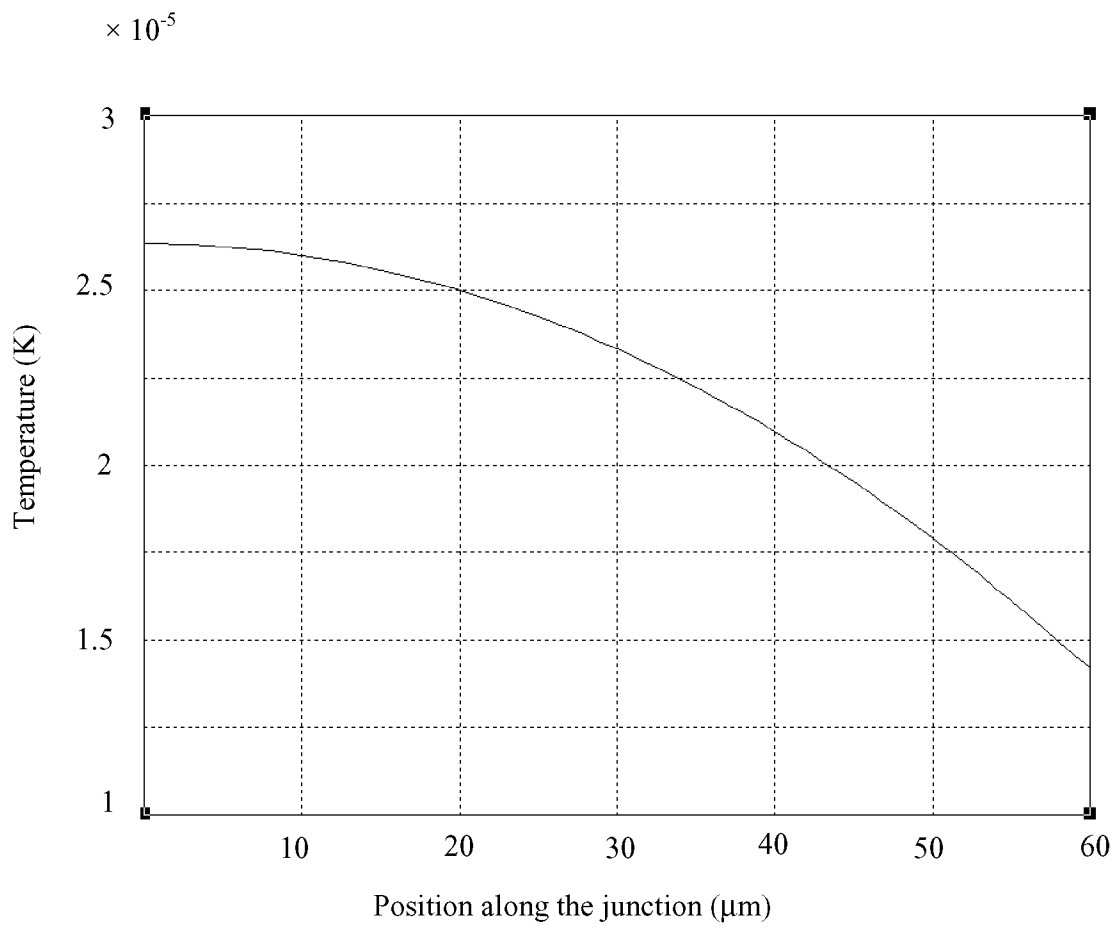


Figure 4.4. Temperature profile along the active junction

As for the reference junction, its temperature is essentially uniform; the temperature difference between its ends is smaller than  $1.0 \times 10^{-8}$  K and remains near the temperature of the heat sink (0 K)<sup>1</sup>. Thus, we will assume that the entire reference junction is kept at a uniform fixed temperature of 0 K. As a result only the temperature of the active junction influences the sensitivity of the instrument.

Since no accepted methods could be found in the literature for treating a thermocouple junction with an internal temperature gradient, it was decided to calculate the sensitivity two different ways. The first way is to take the highest local junction temperature as being representative of the temperature of the entire junction. This assumption is based on the law of successive temperatures, which states that a junction can be modeled as a series of small junctions with intermediate temperatures. The hot junction temperature is the highest temperature of the junction and the cold junction temperature is the lowest, as illustrated in Figure 4.5.

---

<sup>1</sup> The calculations are made on the basis of a relative temperature of T-311 K, as described in Section 3.3.2

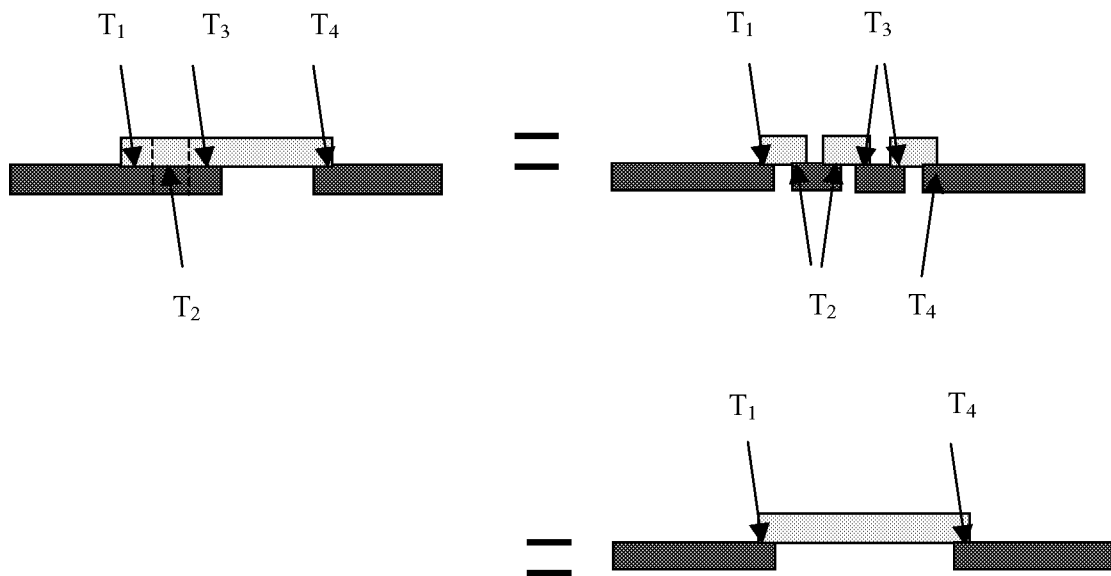


Figure 4.5. The law of intermediate temperatures applied to our model.

The second way that sensitivity is calculated is to take the average temperature at the junction. This assumption is based on the fact that we do not really know where to locate the effective junction in our model. This question has not been answered in the literature found on solid-state physics, but it must somehow be taken into consideration. To partially solve the problem of where to locate the effective junction, the sensitivity has been calculated for different candidate junction locations. The so-called “upper junction”, “physical junction” and “lower junction” are shown in Figure 4.6.

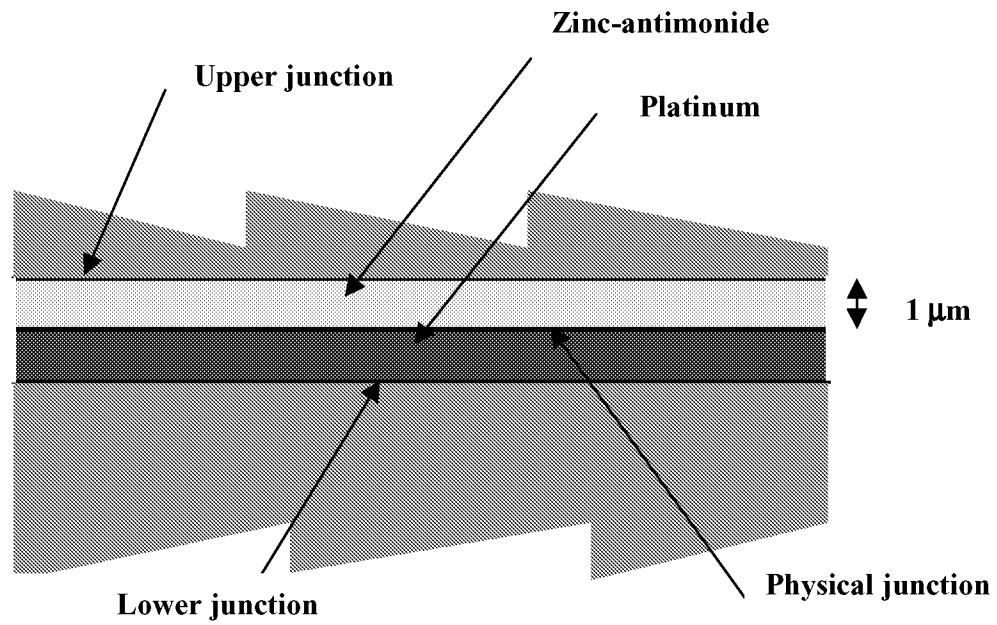


Figure 4.6. Definition of three different candidate junctions according to their locations

Table 4.1 shows the sensitivity obtained by averaging the temperature along the nodes lying within the planes of the three different junction definitions.

Table 4.1. Effect of junction definition on the predicted sensitivity

	<b>Upper Junction</b>	<b>Physical Junction</b>	<b>Lower Junction</b>
<b>Sensitivity</b> ( $\mu\text{V}/\text{Wm}^{-2}$ )	0.04626	0.04624	0.04623

Since no significant difference (less than 0.03 percent) in the predicted sensitivity for the three different junctions was found, the average temperature at the physical junction is used in this thesis.

To study sensitivity, two different two-dimensional configurations have been modeled. The first configuration involves an active junction of 60- $\mu\text{m}$  length, and the second involves an active junction of 93- $\mu\text{m}$  length. The length of the reference junction remains at 93  $\mu\text{m}$  for both configurations. The length of the connecting ramp (25.4  $\mu\text{m}$ ) remains the same in both configurations. These two configurations are used to study the two-dimensionality of the problem.

The effect of the two-dimensionality is greater in the first configuration because the aspect ratio between the active junction and the ramp connecting it to the reference junction is smaller compared to the second configuration (0.33 for the first configuration and 0.44 for the second configuration).

The predicted sensitivities of the one-dimensional and two-dimensional models are presented in Table 4.2

Table 4.2. Sensitivity of the detector based on the one-dimensional and two-dimensional models.

	Sensitivity <sup>1</sup> ( $\mu\text{V}/\text{W}\cdot\text{m}^{-2}$ ) based on the average temperature	Sensitivity <sup>2</sup> ( $\mu\text{V}/\text{W}\cdot\text{m}^{-2}$ ) based on the highest temperature	Improvement of column 2 results over those of column 3 (percent)
One-dimensional model	0.278	0.278	0
Two-dimensional model (first configuration:60- $\mu\text{m}$ length)	0.0205	0.0242	15.3
Two-dimensional model (second configuration 93- $\mu\text{m}$ length)	0.0462	0.0543	14.9

---

<sup>1</sup> Sensitivity calculated based on the average junction temperature

<sup>2</sup> Sensitivity calculated based upon the highest local temperature at the junction

As anticipated, the sensitivity decreases as the two-dimensionality of the model increases. In other words the sensitivity decreases as the size of the ramp becomes bigger compared to the length of the active junction. These results show a significant difference in sensitivity depending upon how the junction temperature is defined. If the temperature at the junction is assumed to be the highest temperature, the value of the sensitivity is increased by more than 15 percent. This difference increases with the two-dimensionality (or inverse of the aspect ratio) of the model.

#### 4.1.3 The time response

The concept of detector time constant is based upon the premise that the detector responds as a first-order system to a step input applied at time  $t = 0$ . This assumption is justified if the detector is modeled with heat capacitance  $C$  (J/K) and a thermal conductance  $K$  (W/K) between the detector and the heat sink. More details on this simple thermal model are given in Section 2.2.3.

If the detector responds as a first-order system, its temperature response as a function of time for a step input at time  $t = 0$  can be modeled as

$$T'(t) = T_{\text{final}} [1 - e^{-t/\tau}], \quad (4.2)$$

where  $\tau$  is the time constant and  $T_{\text{final}}$  is the steady-state temperature. The time constant of the first-order system is defined as the time necessary for the response to reach 63.2 percent of its steady-state value.

The temperature response of the junction has been computed with the dynamic model developed using the finite element tool ALGOR. In order to compare the analytical results with the model of Equation 4.2 we used a least-squares best-fit analysis. With the least-squares method the time constant  $\tau$  is selected to minimize the sum of the squared deviations of the finite element data points from the theory of Equation 4.2. In other words, we minimize the quantity

$$\sum_{i=1}^{\text{nstep}} [T_i - T'_i]^2, \quad (4.3)$$

where  $T_i$  and  $T'_i$  are the calculated finite element and modeled (Equation 4.2) temperatures, respectively, at the  $i^{\text{th}}$  time step  $t_i$ .

This implies that

$$\frac{\partial}{\partial \tau} \left\{ \sum_{i=1}^{nstep} [T_i - T'_i]^2 \right\} = 0 \quad . \quad (4.4)$$

Differentiating yields

$$\sum_{i=1}^{nstep} \frac{t_i}{\tau} \exp(-t_i/\tau) [T_i - T'_i]^2 = 0 \quad . \quad (4.5)$$

Solving Equation 4.5 gives the value of the time constant  $\tau$  in the least-squares sense.

To determine how accurately the temperatures calculated with the finite element model match the temperatures calculated with the first order model, the root-mean-square (rms) error,

$$rms = \frac{1}{nstep} \sqrt{\sum_{i=1}^{nstep} [T_i - T'_i]^2} \quad , \quad (4.6)$$

was computed, where  $nstep$  is the number of steps.

Before running any transient cases on ALGOR a study to optimize the value of the time step increment had to be carried out for both the one-dimensional and two-dimensional models. Plotting the highest model junction node temperature attained for different time steps has provided a value of time step which gives converged results. These plots can be found in Figures 4.7 and 4.8 for the one-dimensional model and the two-dimensional model (second configuration), respectively. An optimized time step of  $1.0 \times 10^{-4}$  s has been chosen for the one-dimensional model, and a  $1.0 \times 10^{-5}$  s time step for the two-dimensional model.

In order to calculate the time constant of the device, a study must be conducted to assess the influence of the assumed effective junction node location on the time response. The time constant may be sensitive to the assumed location of the junction in the two-dimensional model, since some of the thermal energy diverges through the ramp from the active junction towards the reference junction. This effect may modify the time constant of the device depending on which node is used to define the active junction temperature. For this study the time constant has been calculated for different node locations in the active junction, for each of two different model geometrical configurations. The first configuration has a shorter active junction than the second configuration

so as to assess the effect of the two-dimensionality. The effect of the two-dimensionality is bigger in the first configuration where the active junction is smaller (i.e the aspect ratio is smaller).

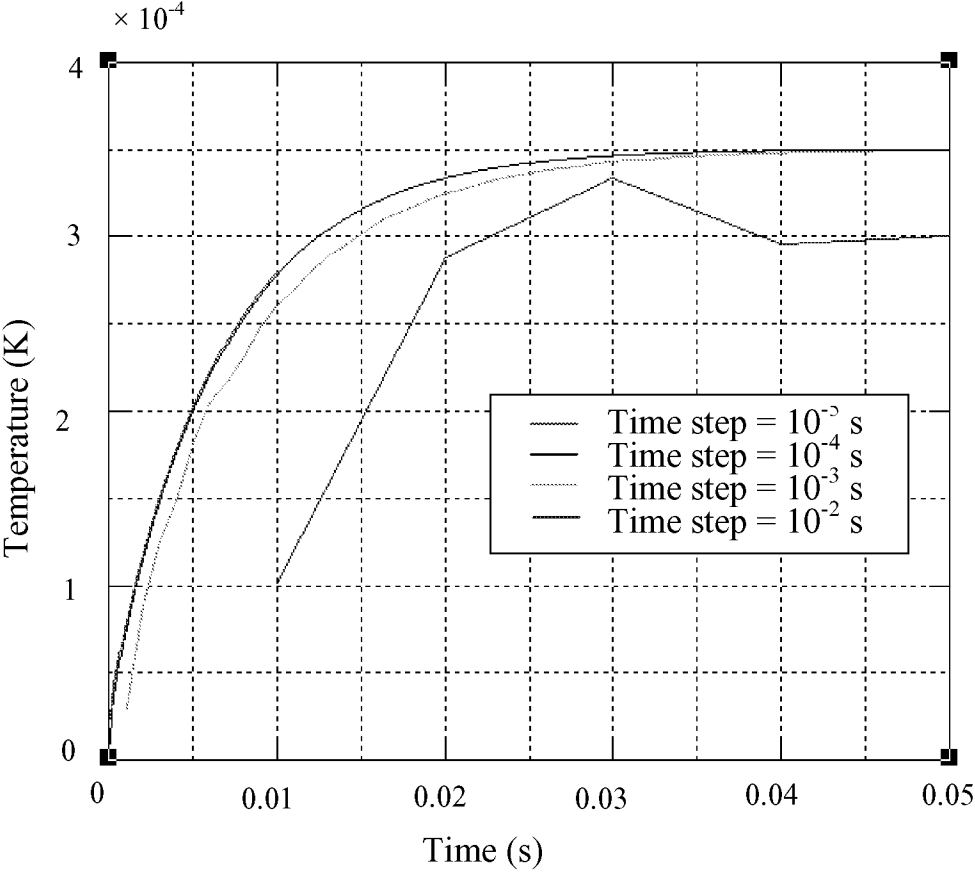


Figure 4.7. One-dimensional model time step optimization

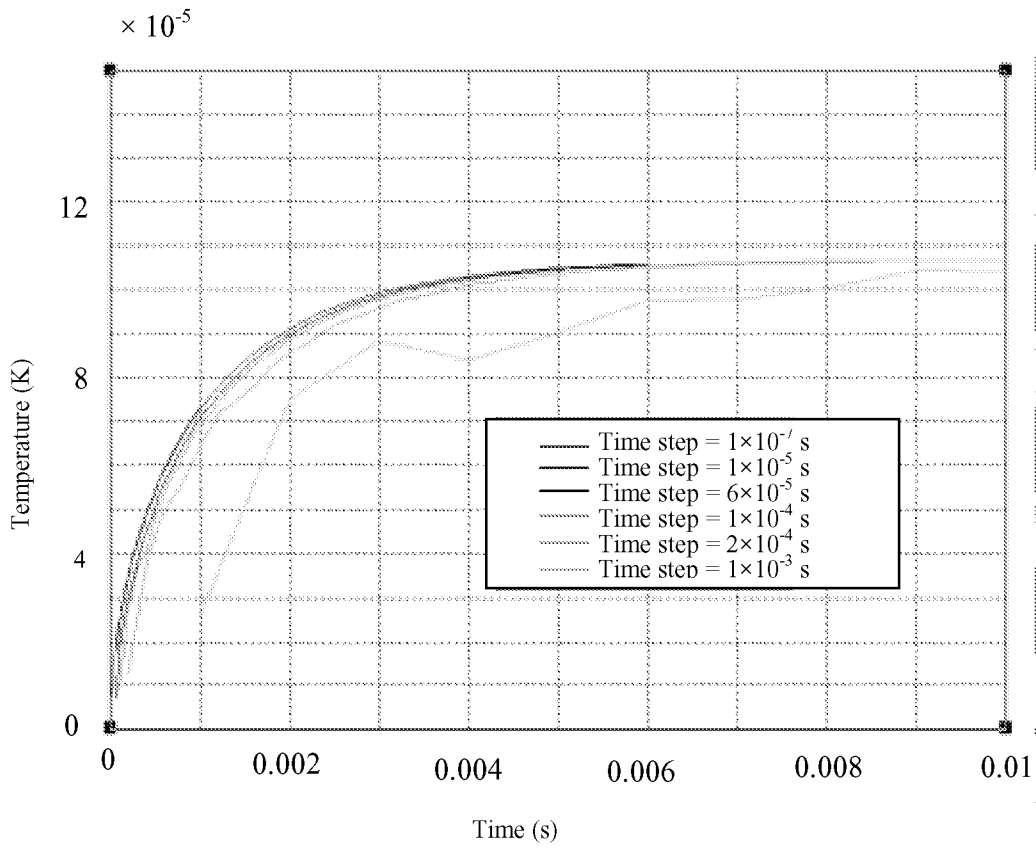


Figure 4.8. Two-dimensional model time step optimization

Nodes at five different locations in the plane of the junction of the thermocouple were selected for the first geometrical configuration (i.e having an active junction length of  $60\ \mu\text{m}$ ). They have been regularly selected with a  $15\text{-}\mu\text{m}$  space separating them. These node locations may be seen in Figure 4.9. The time response corresponding to the different nodes is depicted in Figure 4.10.

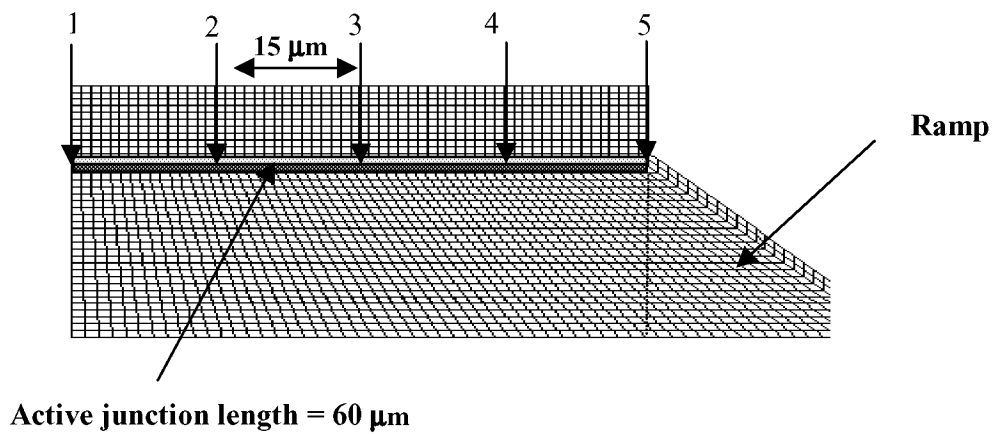


Figure 4.9. Junction nodes selected (active junction length of  $60\ \mu\text{m}$ )

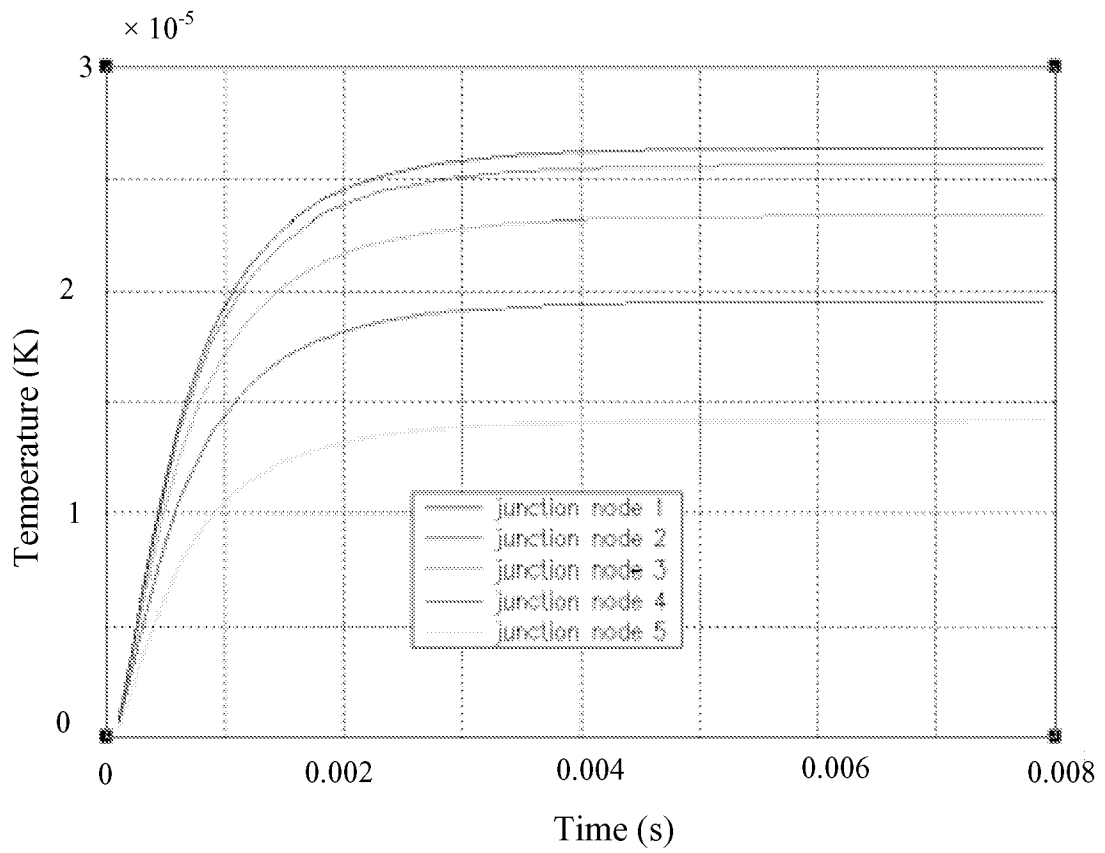


Figure 4.10. Time response of different junction nodes (active junction length of 60  $\mu\text{m}$ )

Six different nodes were selected at the active junction of the thermocouple with the second configuration (i.e with an active junction length of  $93\ \mu\text{m}$ ). They have been selected with a  $22\text{-}\mu\text{m}$  space between the first five nodes and a  $5\text{-}\mu\text{m}$  space between the last two nodes. These node locations may be seen in Figure 4.11, and the time response based on the different nodes is depicted in Figure 4.12.

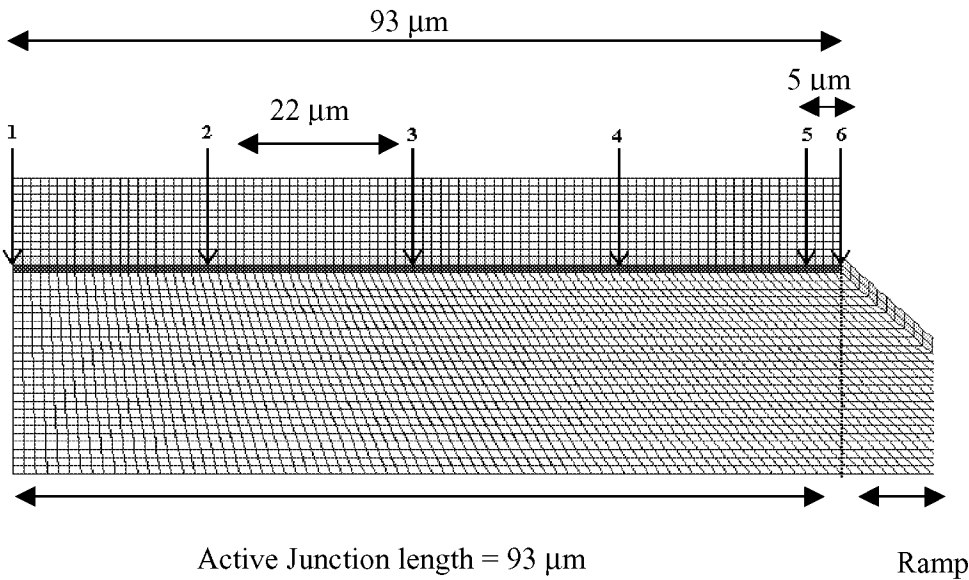


Figure 4.11. Junction nodes selected (active junction length of  $93\ \mu\text{m}$ )

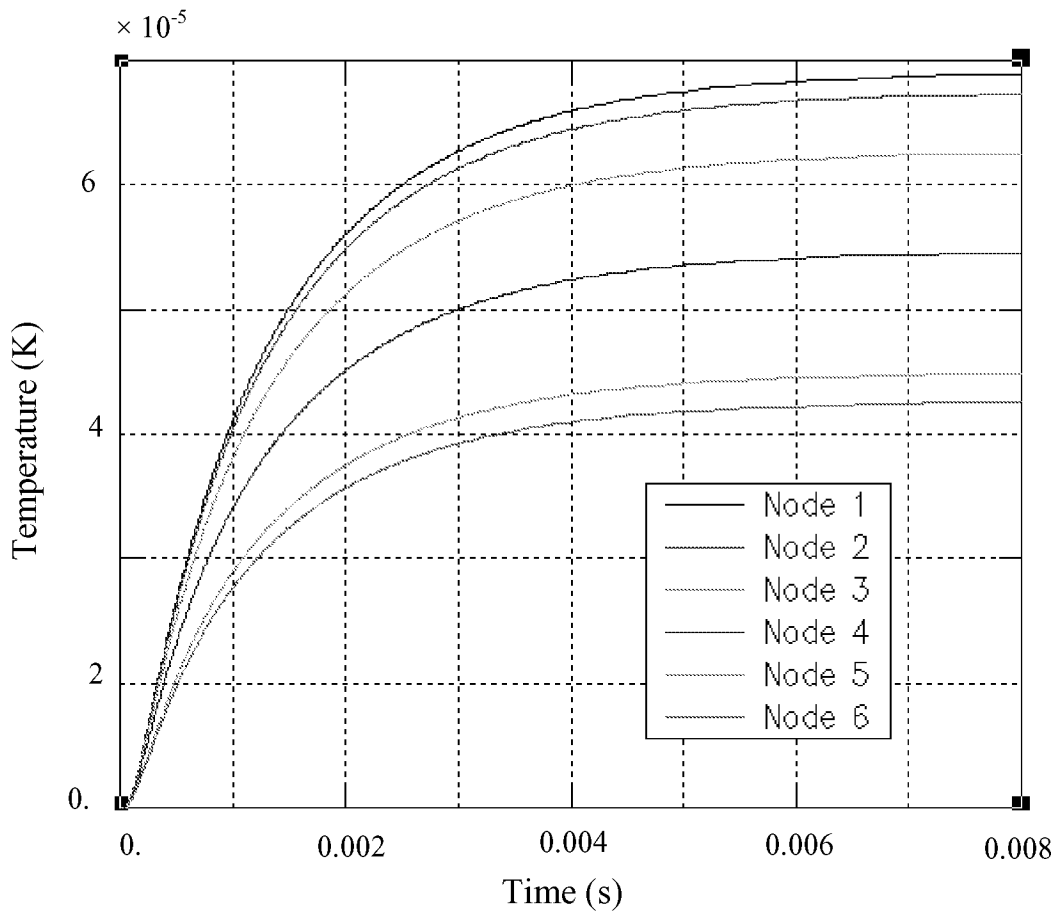


Figure 4.12. Time response of different junction nodes (active junction length of 93  $\mu\text{m}$ )

Table 4.3 presents in tabular form the time constant results and the calculated rms value (using Equation 4.6) associated with all of the selected nodes as well as for the scheme where the junction nodes are averaged together.

Table 4.3. Influence of the device geometry on time constant and rms error.

	First configuration (60 $\mu\text{m}$ )	Second configuration (93 $\mu\text{m}$ )
Node 1	$\tau = 0.80 \text{ ms}$ $\text{rms} = 4.88 \cdot 10^{-7} \text{ K}$	$\tau = 1.4 \text{ ms}$ $\text{rms} = 6.87 \cdot 10^{-7} \text{ K}$
Node 2	$\tau = 0.79 \text{ ms}$ $\text{rms} = 4.73 \cdot 10^{-7} \text{ K}$	$\tau = 1.3 \text{ ms}$ $\text{rms} = 6.56 \cdot 10^{-7} \text{ K}$
Node 3	$\tau = 0.79 \text{ ms}$ $\text{rms} = 4.22 \cdot 10^{-7} \text{ K}$	$\tau = 1.3 \text{ ms}$ $\text{rms} = 5.75 \cdot 10^{-7} \text{ K}$
Node 4	$\tau = 0.78 \text{ ms}$ $\text{rms} = 3.50 \cdot 10^{-7} \text{ K}$	$\tau = 1.3 \text{ ms}$ $\text{rms} = 4.61 \cdot 10^{-7} \text{ K}$
Node 5	$\tau = 0.78 \text{ ms}$ $\text{rms} = 2.55 \cdot 10^{-7} \text{ K}$	$\tau = 1.3 \text{ ms}$ $\text{rms} = 3.38 \cdot 10^{-7} \text{ K}$
Node 6	-	$\tau = 1.3 \text{ ms}$ $\text{rms} = 4.89 \cdot 10^{-7} \text{ K}$
Average across the junction	$\tau = 0.79 \text{ ms}$ $\text{rms} = 3.64 \cdot 10^{-7} \text{ K}$	$\tau = 1.3 \text{ ms}$ $\text{rms} = 4.88 \cdot 10^{-7} \text{ K}$

Two important results may be inferred from these data. First, the calculated time constant remains constant along the junction independent of the effective junction location used. Due to the negligible differences (at most 1.25 percent) in the schemes where the average junction nodes are used and where the highest temperature node is used, it was decided to use the transient response based on the highest temperature for the remaining analysis. The second result is that the rms error is small enough to validate the least-squares fit and thus the use of the first-order model for time response. That is, we can indeed refer to the “time constant” of this particular distributed thermal system. It should be noted that the rms error decreases as the distance between the nodes and the ramp decreases. This behavior cannot be easily explained. Figure 4.13 displays a comparison between the finite-element time response function and the “best-fit” curve from the first-order model. The term “best-fit” here refers to a curve based on using Equation 4.2 with a value of  $\tau$  derived from application of Equation 4.5. The error between the two response curves (the linear interpolation of the data points and the “best-fit” curve) is plotted in Figure 4.14 and is less than 2.88 percent at any given time.

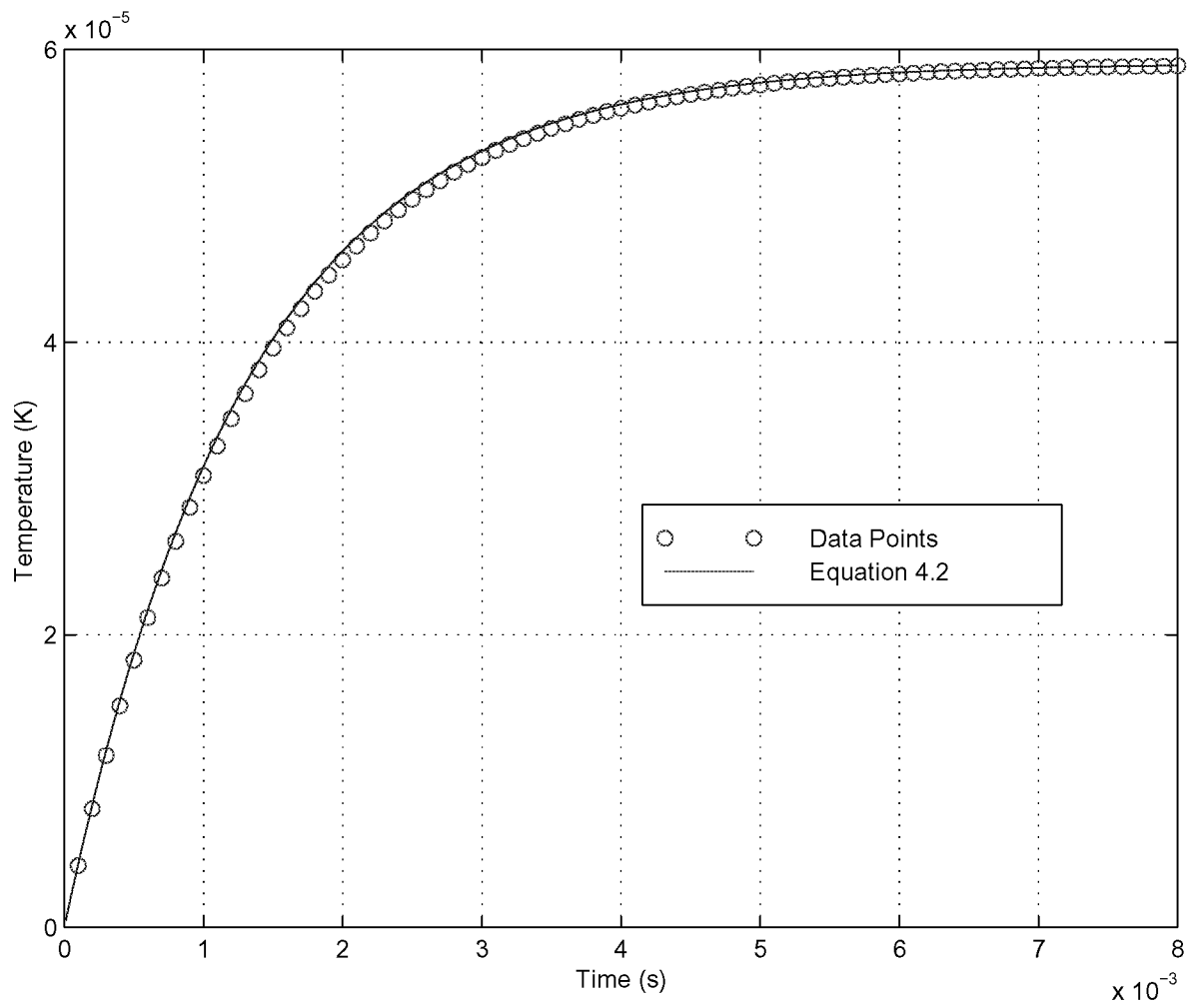


Figure 4.13. Comparison between the finite element time response function (Data points) and the “best-fit” curve (Equation 4.2) from the first-order model.

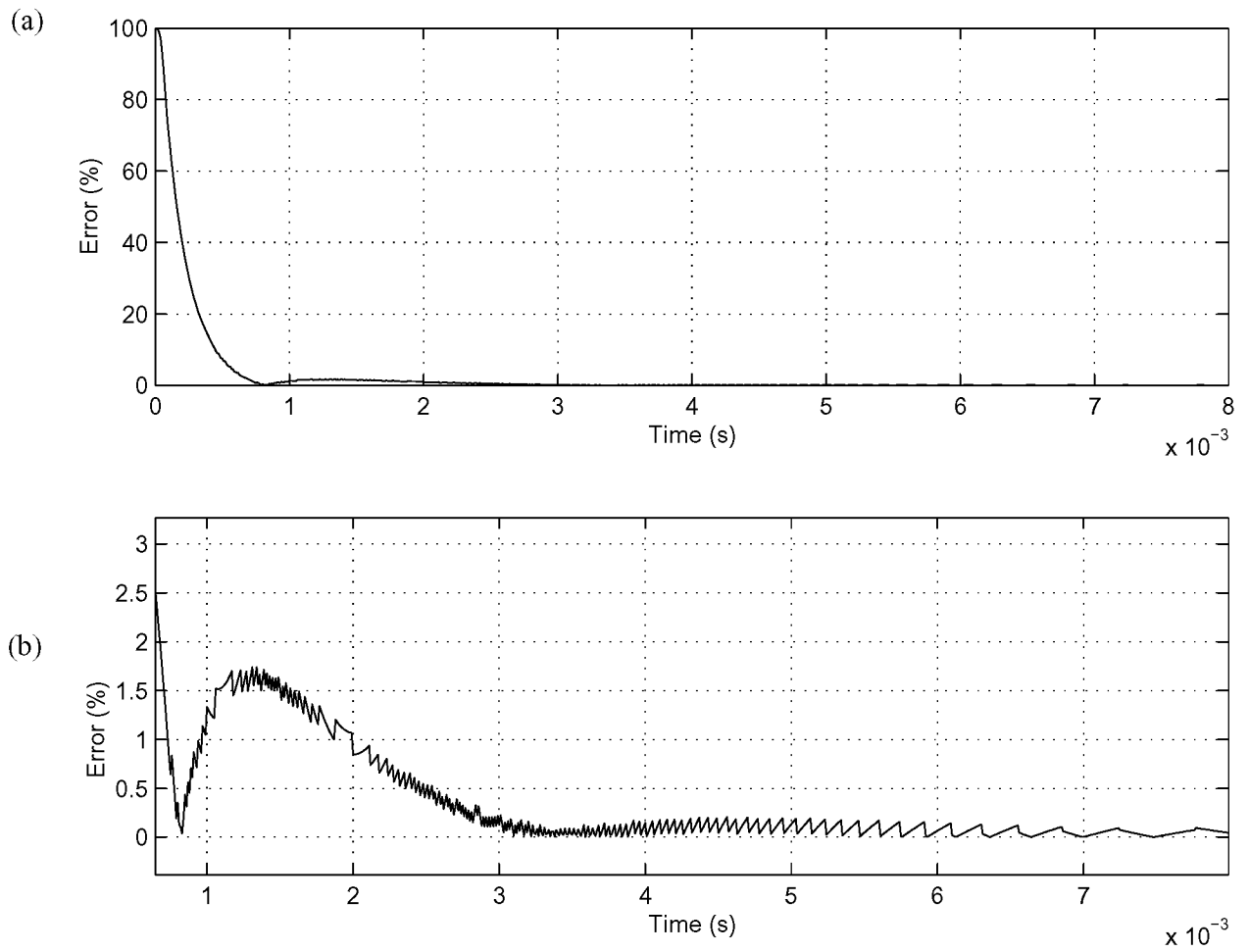


Figure 4.14. (a) Error (percent) between the finite element time response function and the “best-fit” curve (Equation 4.2), and (b) view with greater vertical resolution for  $t \geq 0.7 \times 10^{-3}$  s.

#### 4.1.4 Conclusion

A summary comparison of both the one-dimensional and the two-dimensional model is displayed in Table 4.4.

Table 4.4. Comparison between the one-dimensional and two-dimensional models

	<b>One-dimensional model</b>	<b>Two-dimensional model</b> ( active junction length = 93 $\mu\text{m}$ )
<b>Assumptions</b>	One-dimensional heat flux Ramp effect neglected Reference junction not modeled	Two-dimensional heat flux Ramp effect taken into account Reference junction kept at 0 K
<b>Sensitivity</b> ( $\mu\text{V}/\text{W}\cdot\text{m}^{-2}$ ) based upon the highest temperature	0.278	0.0543
<b>Time constant</b> (ms)	7.8	1.4
<b>Rms</b> (Equation 4.6)(K)	$6.89 \times 10^{-7}$	$6.87 \times 10^{-7}$

The two-dimensional model yields a decrease in sensitivity and a faster time response compared to the one-dimensional model. The fact that the heat sink is twice as big in the two-dimensional case as in the one-dimensional case explains why the steady-state temperature reached is smaller in the two-dimensional case, and therefore so is the sensitivity. The fact that we obtain a time constant almost three times larger in the one-dimensional model than in the two-dimensional model with an active junction of 93  $\mu\text{m}$  can be readily explained. The effect of having an aspect ratio between the heat source and the heat sink of less than one-half is that the lower steady-state temperature is going to be reached faster than in the one-dimensional model. We tentatively conclude from this study that there exists an inverse relationship between sensitivity and time response for the current thermopile design. As far as the effect of the addition of the ramp on the

sensitivity and the time response is concerned, nothing can be inferred thus far.

From the foregoing explanation one can assume that the two main geometric parameters responsible for the two-dimensional effect are the aspect ratio between the heat source and the heat sink and (likely) the slope, or length, of the ramp connecting the active junction with the reference junction. The effect of these two parameters on the sensitivity and the time response of the thermocouple is presented in the next section.

## **4.2 Parametric study**

The results of a parametric study, including geometric parameters and boundary condition parameters, are presented in this section along with an optimized design of the thermocouple pair.

The heat source (active junction) size and the slope of the ramp connecting the active and reference junctions are the two geometric parameters varied. The spatial distribution of the heat flux boundary condition was also used as a parameter in the design optimization.

### **4.2.1 Heat-source (active junction) size effect**

Different versions of the thermocouple thermal models have been created by changing the size of the active junction while holding all other parameters constant. The active junction length was varied between 93  $\mu\text{m}$  and 1000  $\mu\text{m}$  in order to characterize the effect of this parameter on the sensitivity and time constant of the thermocouple. By increasing the size of the active junction, the area illuminated by heat radiation is increased. The tendency should be that the modeled performance converges to the one-dimensional results since the contribution of the ramp and the reference junction would become small compared to those of the active junction. The motivation for this study is to know how large the active junction must be relative to the rest of the design such that the two-dimensional effects described above are negligible. In other words we would like to obtain relations giving the sensitivity and time response of the thermocouple as a function of the active junction length. To determine these relationships five model versions with active junction lengths of 60, 93, 200, 500 and 1000  $\mu\text{m}$  have been created. The transient response of each model

version is displayed in Figure 4.15. This figure clearly demonstrates that as we increase the active junction length the thermal time response converges to that of the one-dimensional model.

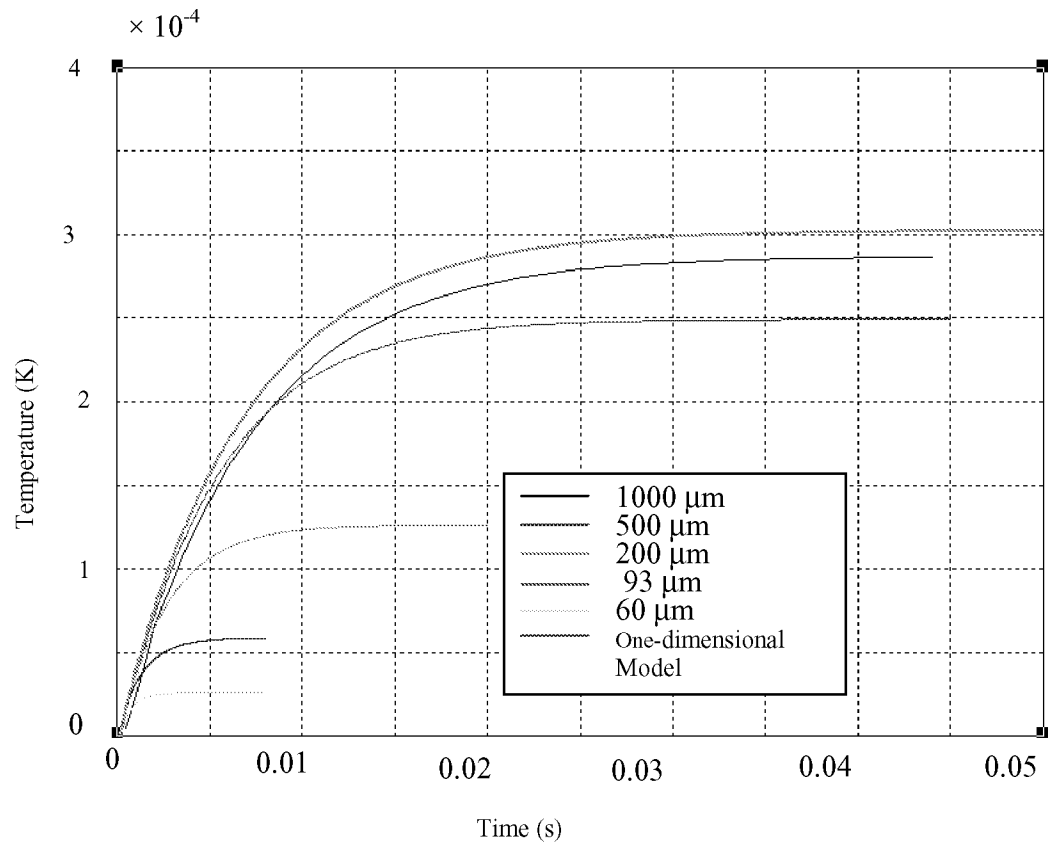


Figure 4.15. Influence of the size of the active junction on the thermal time response of the thermocouple.

Prototype detectors with active junctions over 1000  $\mu\text{m}$  have been fabricated and tested by Vattel and their behavior compared to the one-dimensional model. The sensitivity of the prototypes manufactured to date vary from 0.203 to 0.276  $\mu\text{V}/\text{Wm}^{-2}$  which is in good agreement with the one-dimensional model predictions ( $> 0.264 \mu\text{V}/\text{Wm}^{-2}$ ).

Figures 4.16 and 4.17 display the sensitivity and the time constant as a function of the active junction length. The last data points plotted for an active junction length of 5000  $\mu\text{m}$  represents the one-dimensional model. This value, supposedly for an infinite active junction length, is used to fit an exponential curve of the form

$$\text{Sensitivity}(l) = 0.278 (1 - e^{-l/350}) \tag{4.7}$$

to the calculated points in Figure 4.16.

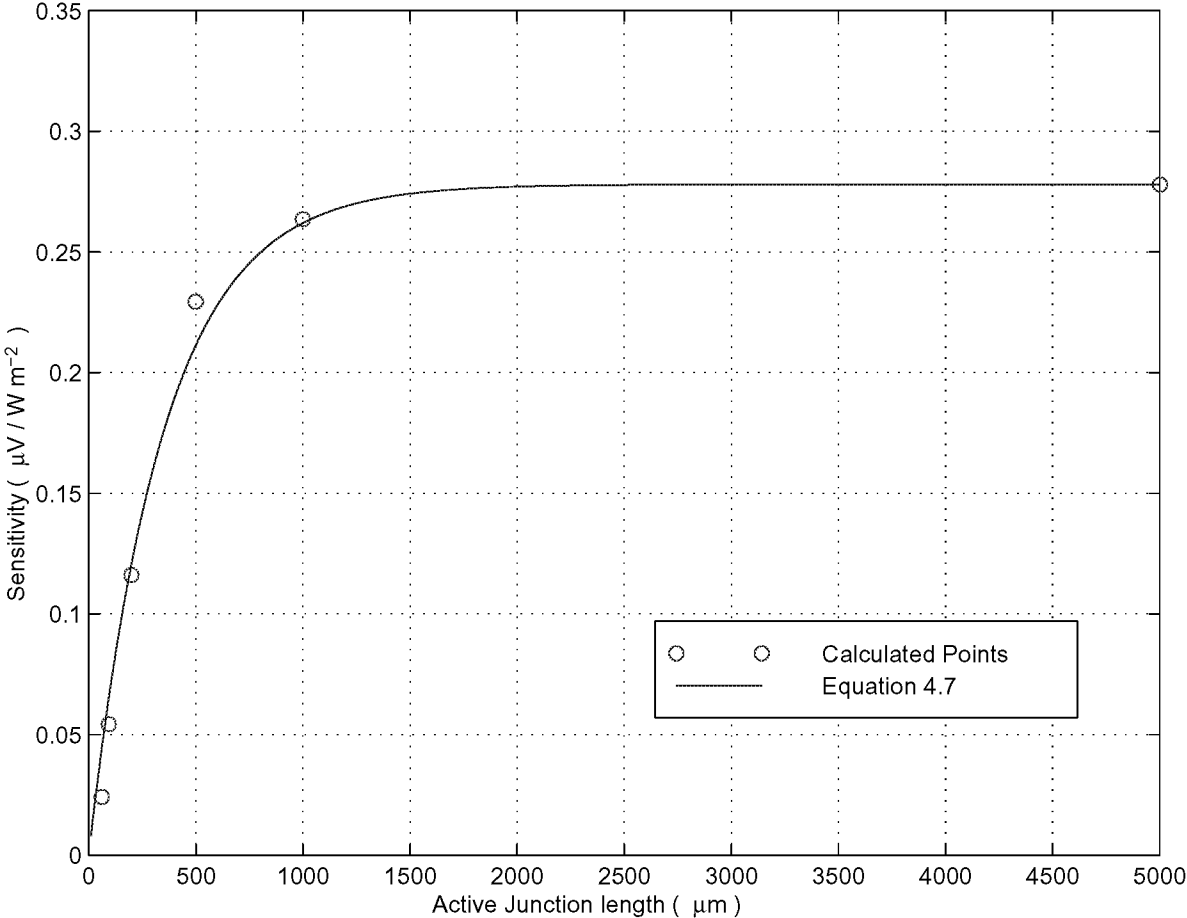


Figure 4.16. Sensitivity of the thermocouple as a function of the active junction length.

An exponential curve of the form

$$\tau(l) = 7.8 \cdot 10^{-3} (1 - e^{-l/420}) \quad (4.8)$$

has been fitted to the calculated points in Figure 4.17. Here also the value of the one-dimensional time constant has been used for an infinite active junction length.

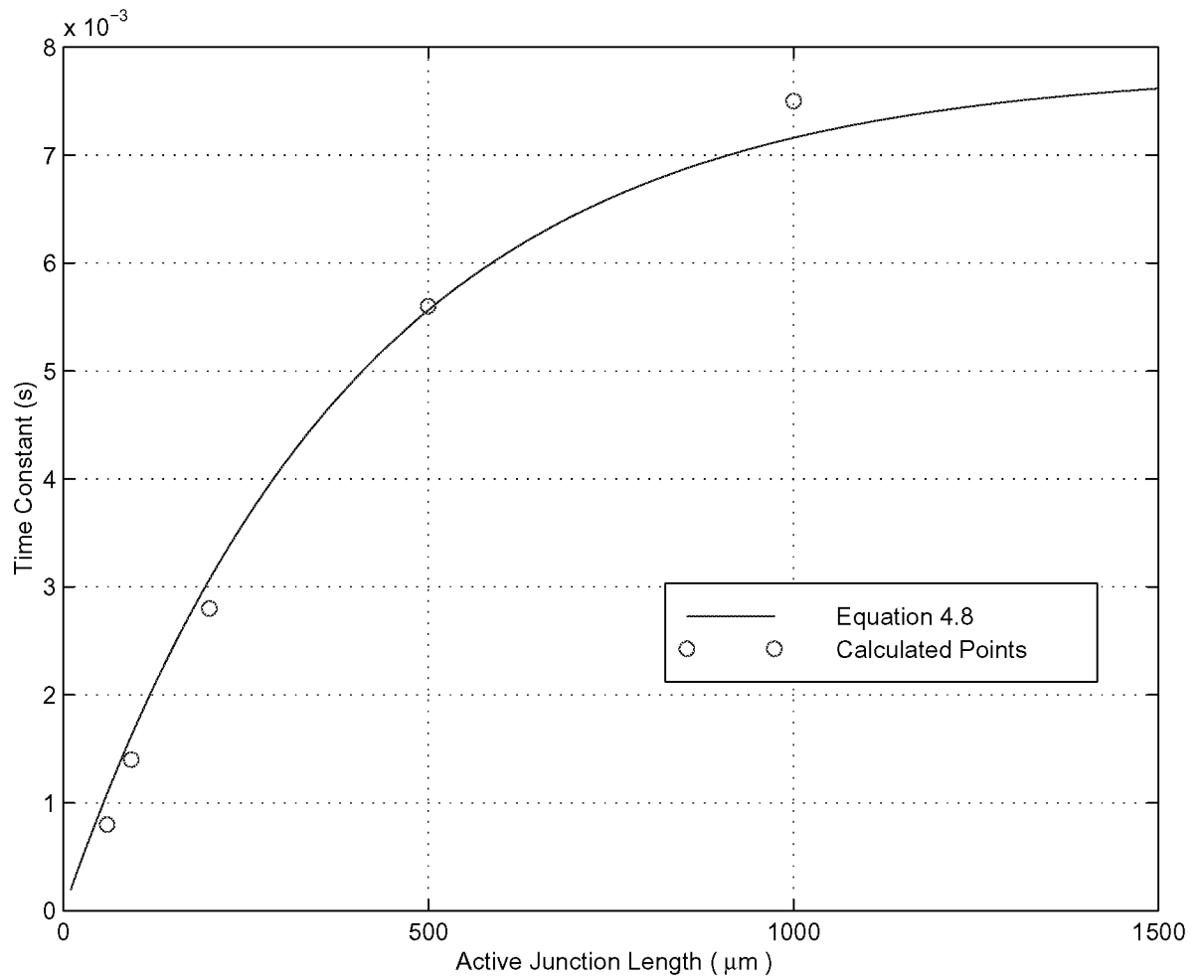


Figure 4.17. Time constant of the thermocouple as a function of the active junction length

The values of the different time constants obtained for the six cases and the associated rms error are presented in Table 4.5.

Table 4.5. Sensitivity, time constant and rms error associated for different active junction lengths

	Sensitivity ( $\mu\text{V}/\text{Wm}^{-2}$ )	Time Constant (ms)	Rms error Equation 4.6 (K)
1000 $\mu\text{m}$ case	0.2636	6.3	$8.7 \times 10^{-6}$
500 $\mu\text{m}$ case	0.2294	5.5	$1.63 \times 10^{-6}$
200 $\mu\text{m}$ case	0.1162	2.8	$1.1 \times 10^{-6}$
93 $\mu\text{m}$ case	0.05430	1.4	$6.87 \times 10^{-6}$
60 $\mu\text{m}$ case	0.02423	0.80	$4.88 \times 10^{-7}$
One-dimensional model	0.2780	6.8	$6.88 \times 10^{-7}$

#### 4.2.2 Ramp slope effect

In this section the effect on the sensitivity and time constant of the slope of the ramp connecting the active and the reference junctions is studied. It is desirable to determine an optimized ramp angle,  $\alpha$ , so as to optimize the trade-off between the sensitivity and the time constant of the thermocouple. Five different case studies have been performed. These studies cover ramp angles,  $\alpha$ , of 26.5, 35, 45, 50 and 63.4 deg. The two extreme design cases ( $\alpha = 26.5$  and  $\alpha = 63$  deg) and the base-line design case where  $\alpha = 45$  deg are illustrated in Figure 4.18.

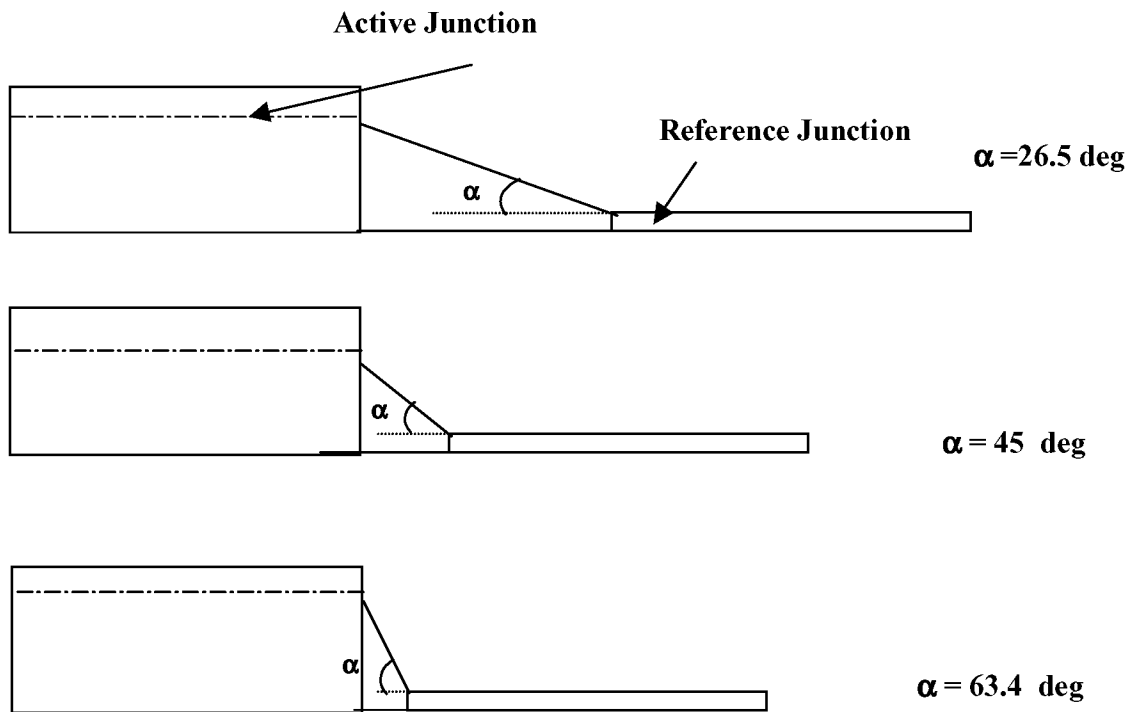


Figure 4.18. Comparison of three different designs considered in the parametric study

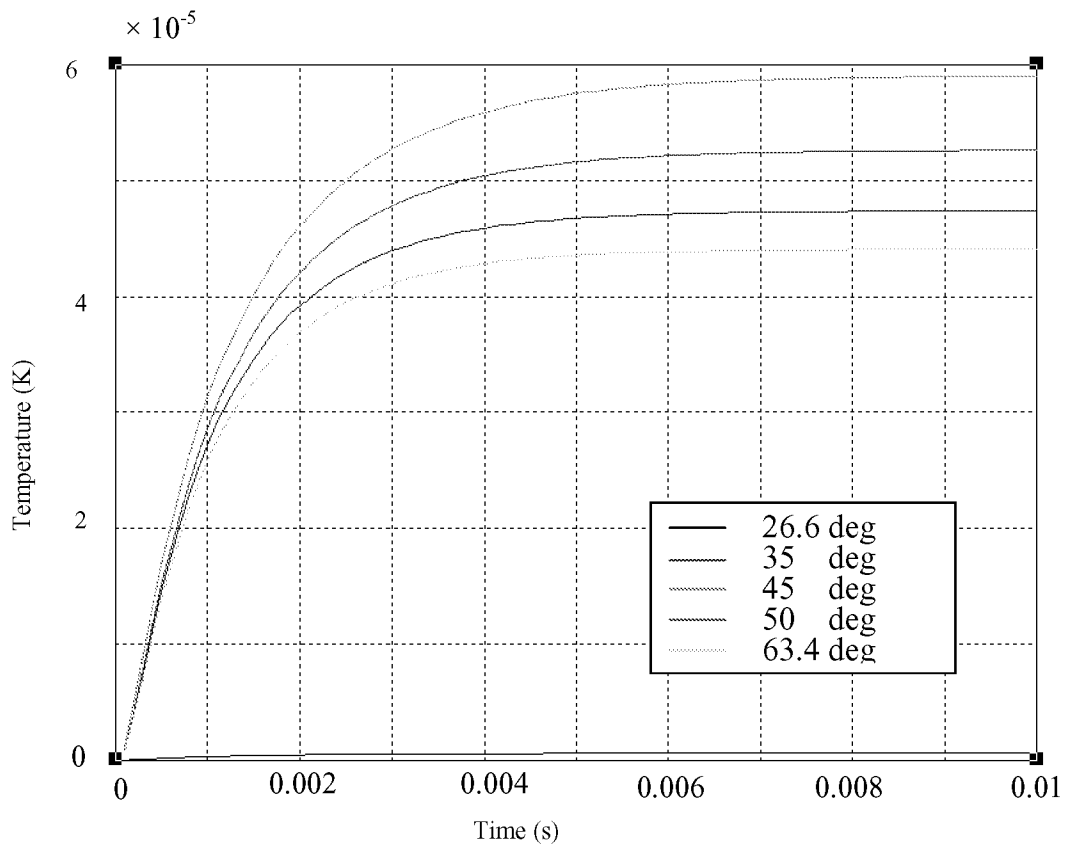


Figure 4.19. Effect of the ramp slope on the thermal time response of the thermocouple.

Figure 4.19 clearly shows that the slope of the ramp contributes to the two-dimensional effect if all other geometric parameters are held constant. However this contribution is not linear. The sensitivity increases as the angle increases from 26.5 to 45 deg and then it decreases as the angle increases beyond 45 deg up to 63 deg.

This behavior is explained by the fact that as the angle varies two other variables are inevitably varied, each of which has an opposite effect on sensitivity. The two variables are the thermal resistance of the ramp,  $R_t$ , and the aspect ratio  $r$  (the same defined in Section 4.1.2) between the heat source and the heat sink. As the ramp angle  $\alpha$  increases the resistance  $R_t$  decreases whereas the aspect ratio  $r$  increases. When the angle  $\alpha$  increases, the effective length  $l$  (m) decreases (Figure 4.18) and the effective cross-sectional area  $A_c$  ( $m^2$ ) increases, so that according to

$$R_t = \frac{l}{k A_c}, \quad (4.9)$$

$R_t$  decreases.

Decreasing the thermal resistance of the ramp decreases the sensitivity whereas increasing  $r$  increases the sensitivity. From the ramp angles between 26.5 to 45 deg the "resistance effect" is dominant and the sensitivity increases, and from 45 to 63 deg the "aspect ratio effect" is dominant and the sensitivity decreases.

Figure 4.20 displays the sensitivity as a function of the ramp angle  $\alpha$ . The time constant as a function of the ramp angle  $\alpha$  is not shown because it is essentially constant.

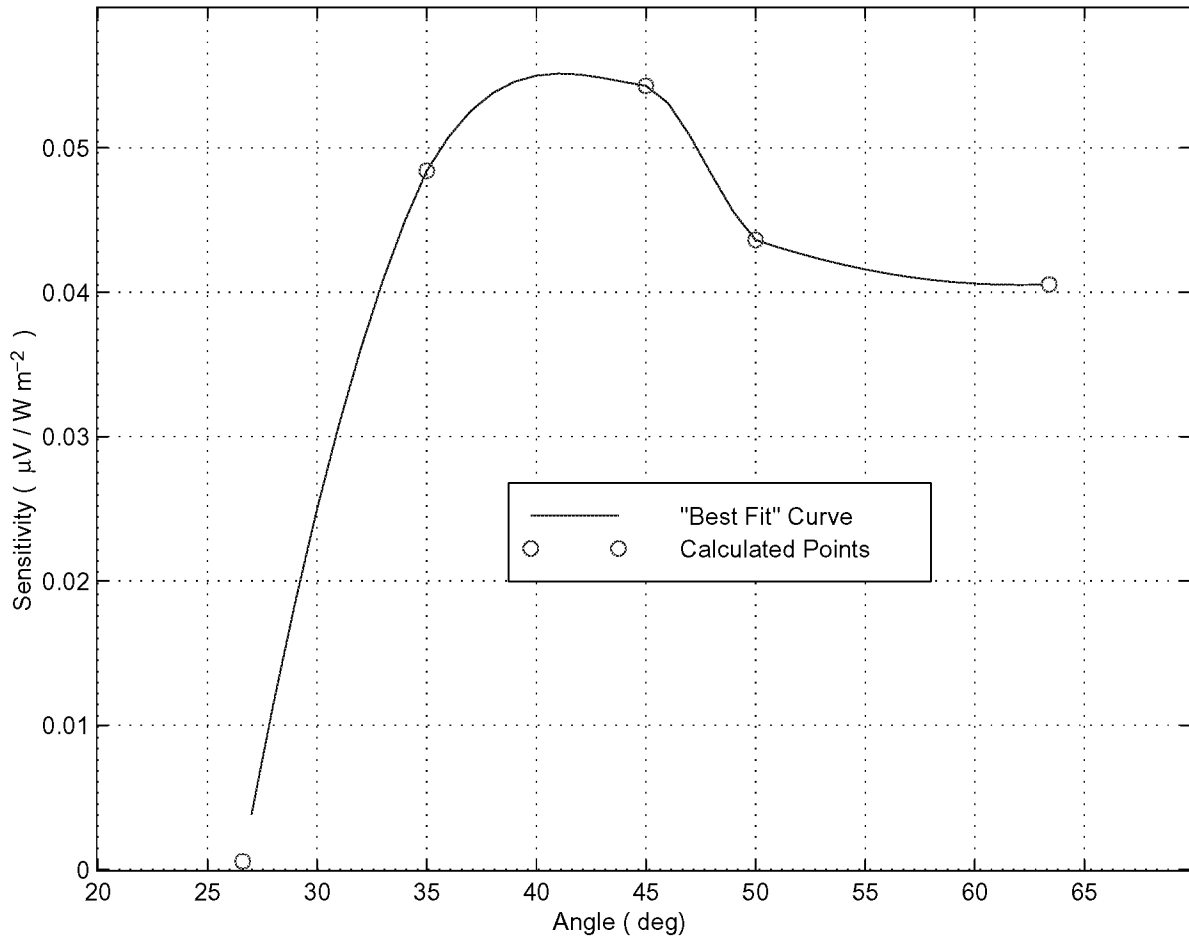


Figure 4.20. Sensitivity in function of the ramp angle  $\alpha$ . (The “best-fit” curve is provided to help the eye follow the trend, it has no theoretical basis)

The values of the sensitivity, time constant and associated rms error are presented in Table 4.6.

Table 4.6. Sensitivity, time constant and rms error for different ramp angles

$\alpha$ (deg)	Sensitivity ( $\mu\text{V}/\text{Wm}^{-2}$ )	Time Constant (ms)	Rms error (K)
26.5	$582.3 \times 10^{-6}$	1.3	$5.17 \times 10^{-9}$
35	0.04841	1.3	$7.04 \times 10^{-7}$
45	0.05430	1.4	$6.87 \times 10^{-7}$
50	0.04362	1.2	$6.80 \times 10^{-7}$
63.4	0.04053	1.2	$6.70 \times 10^{-7}$
One-dimensional model	0.2780	6.8	$6.88 \times 10^{-7}$

#### 4.2.3 Heat flux boundary condition

Nominally, incident radiation falls only on the active junction. In seeking to optimize the responsivity of the device a study was conducted where the heat flux boundary condition is extended to the ramp connecting the active junction and the reference junction, as shown in Figure 4.21.

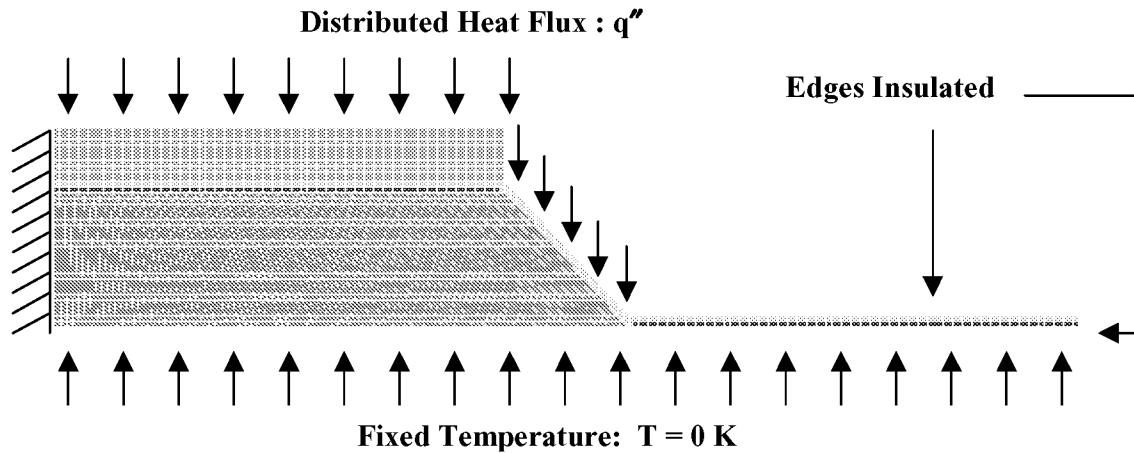


Figure 4.21. New model boundary conditions

By extending the boundary conditions to include the ramp the calculated sensitivity increased by 7 percent, from  $0.0543$  to  $0.0584 \mu\text{V}/\text{Wm}^{-2}$ . Implementing this new boundary condition with the physical device would require slight changes in the position of the thermopile array in the cavity. The array would have to be positioned such that the incoming radiation illuminates both the active junction and the ramp connecting it to the reference junction.

The results obtained from the parametric studies presented in this chapter will be helpful in the design optimization of the thermopile linear array and provide useful feedback for the thermopile manufacturer. Tradeoffs between sensitivity and time constant must be made since decreasing the size of the thermocouple will provide faster time response but smaller sensitivities.

In the following section the possibility of having eddy currents flowing in the active junction is studied. So far it has been assumed that no current flows in the active junction even though a temperature gradient was found there. By taking into account the temperature gradient, the presence of local eddy currents is at least possible, which implies that the Peltier, Thomson and Joule effects

may have to be accounted for in the energy equation. At this point this is only a working hypothesis; experiments need to be carried out to verify it. In this section more questions are raised than answered.

### 4.3 Electrical model of the active junction

According to the temperature distribution results obtained in the previous sections, temperature gradients exist in the active junction. Temperature gradients may cause eddy currents to flow in the junction. Those currents are not taken into account in the current thermal model. If those currents exist the Peltier, Thomson and Joule effects must somehow be taken into account in the energy equation. An electrical model of the active junction has been formulated in order to estimate the magnitude of the currents. The active junction of the 60- $\mu\text{m}$  active junction model has been discretized into cells with the temperature fixed at different values at the two ends. The cells created correspond to the finite element control volumes used in the thermal model. Figure 4.22 displays 60 discrete cells of 1- $\mu\text{m}$  length each (61 nodes) and the associated electrical model. The temperature gradient  $\Delta T_i$  between Node  $i$  and Node  $i+1$  creates a current  $I_i$  in cell  $i$ . The generated voltages  $V_i$  (V) can be calculated using the Seebeck effect Equation 4.2, relating the emf  $V_i$  to the temperature gradient  $\Delta T_i$  (K) and the Seebeck coefficient  $S_{\text{ZnSb-Pt}}$  ( $\mu\text{V/K}$ ).

$$V_i = S_{\text{ZnSb-Pt}} \Delta T_i . \quad (4.10)$$

The resistance  $R_1$  ( $\Omega$ ) represents the zinc-antimonide resistance and  $R_2$  ( $\Omega$ ) the platinum resistance. The resistances  $R_1$  and  $R_2$  are calculated based on the resistivity  $\rho_1$  and  $\rho_2$  ( $\Omega\text{m}$ ) of the associated material according to the relationship

$$R = \frac{\rho L}{A} , \quad (4.11)$$

where  $L$  (m) is the length of material conducting the current flow and  $A$  ( $\text{m}^2$ ) is the cross-sectional area.

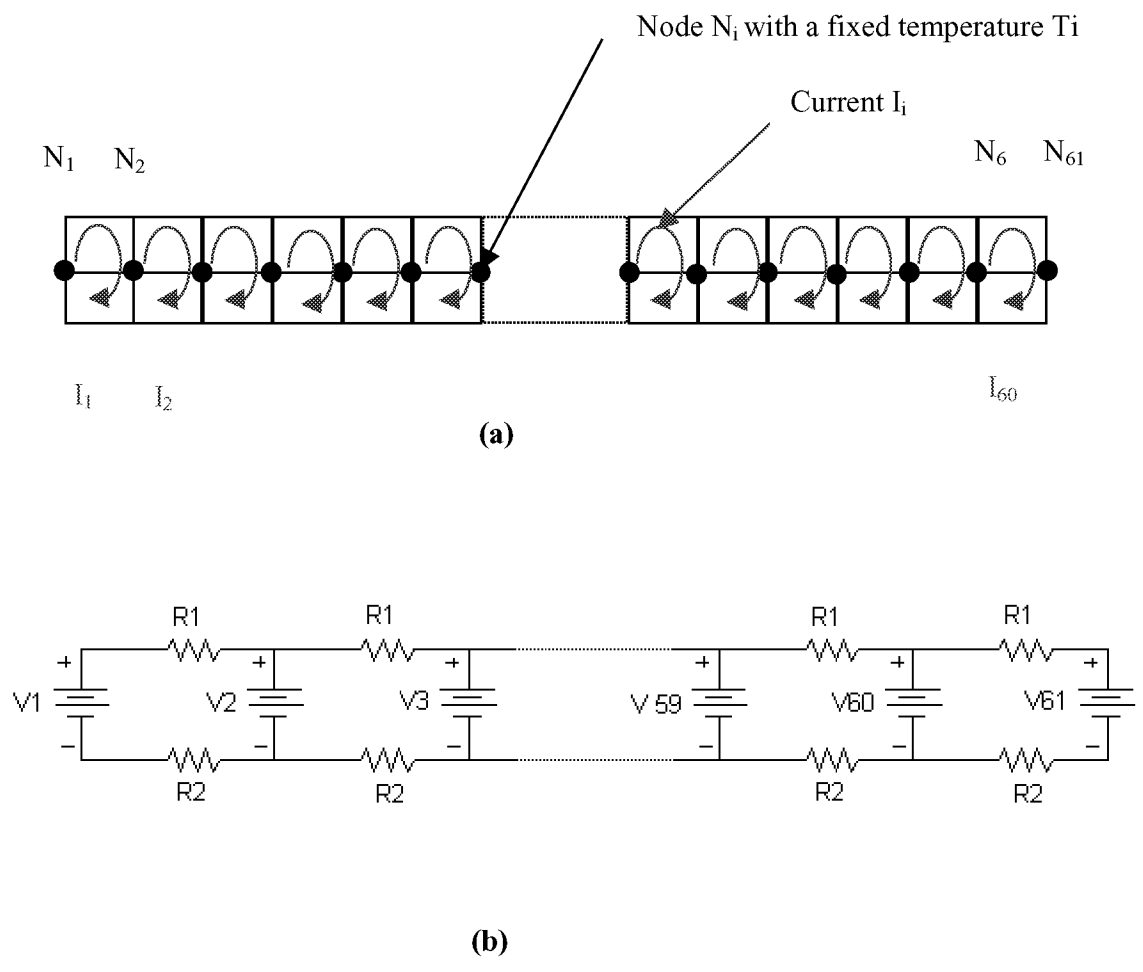


Figure 4.22. The distributed junction represented as (a) sixty discrete cells (61 nodes) and (b) the associated electrical model.

In order to evaluate the different currents  $I_i$  flowing in the 60 cells, the algebraic system

$$\begin{aligned} V_1 + R_1 I_1 - V_2 + R_2 I_1 &= 0 \\ V_2 + R_1 I_2 - V_2 + R_2 I_2 &= 0 \\ \vdots & \\ V_{60} + R_1 I_{60} - V_2 + R_2 I_{60} &= 0 \end{aligned} \quad (4.12)$$

was solved for each  $I_i$ . This leads to the equivalent system

$$I_k = \frac{(V_{k+1} - V_k)}{R_1 + R_2} \quad , \quad k=1,2, \dots, 60 \quad . \quad (4.13)$$

Using Equations 4.2 and 4.3 we obtain

$$I_k = \frac{(T_{k+1} - T_k) S_{\text{ZnSb-Pt}} A}{(\rho_1 + \rho_2) L} \quad , \quad k=1,2, \dots, 60 \quad , \quad (4.14)$$

where  $T_k$  is the temperature (K) at node k calculated by the finite element model.

The idea is to modify the energy equation, Equation 3.3, by adding a heat source term  $q'''_k$  (W) of the form

$$q'''_k = R I_k^2 + P_{AB} I_k + \sigma_{AB} \frac{\Delta T}{\Delta X} I_k \quad (4.15)$$

for each node k of the finite grid through which an current  $I_k$  flows. Equation 4.6 takes into account the power due to the Peltier, Thomson and Joule effects. The new temperature distribution could be calculated by the finite difference method. The unresolved problem is to determine the coefficients associated with the Peltier and Thomson effect. To accomplish this additional experiments would need to be carried out. For example, we could take a rod of zinc-antimonide with a temperature gradient. We could force a current through it and then be able to measure the heat loss (if the current goes with the temperature gradient). The Thomson coefficient of the rod of zinc-antimonide could be calculated, knowing how much energy has been dissipated by the Joule effect.

A temperature gradient of  $1.213 \times 10^{-5}$  K is found at the two ends of a 60- $\mu\text{m}$  active junction. The eddy current flowing in the active junction due to this temperature gradient would be on the

order of 0.2 mA and the heat released by the Joule effect would then be on the order of  $4.24 \times 10^{-15}$  W, which is surely negligible. It might be expected that the heat absorbed and released by the Peltier and Thomson effects would also be of the same order of magnitude, and therefore also negligible.

## 5. Conclusions and Recommendations

The results of the dynamic electrothermal model are reviewed in this section. Suggestions for further research are also provided.

### 5.1 Conclusions

1. A dynamic electrothermal model of a thermocouple junction pair has been formulated which predicts the sensitivity of the nominal thermopile detector design (Figure 3.8) to be  $0.0543 \mu\text{V}/\text{Wm}^{-2}$  and its time constant to be 1.4 ms.
2. The model allows parametric studies aimed at improving the sensitivity and time response characteristics in the design of the thermocouple. The study shows that by illuminating the ramp connecting the active junction to the reference junction an improvement in the sensitivity of the instrument of seven percent may be obtained. We conclude that the new design of the thermopile linear array in its cavity should be such that the active junction and the ramp are directly illuminated by incoming radiation.
3. A parametric study has been performed with the active junction length and the ramp slope as variables. The sensitivity and time constant of the thermocouple pair are very sensitive to the active junction length. By increasing the junction length to greater than  $1000 \mu\text{m}$  the design converges to a one-dimensional model with excellent sensitivity ( $0.278 \mu\text{V}/\text{Wm}^{-2}$ ) and time

constant (7.8 ms). A relationship between the sensitivity and time constant as a function of the active junction length has been determined. This should prove to be a valuable tool to optimize the thermocouple according to the sensitivity and time constant specifications. The sensitivity of the thermocouple is less sensitive to the ramp slope and seems to be maximized for an angle of 45 deg. The time constant is essentially independent of the ramp slope.

4. For future CERES-like instruments a thermopile made of thermocouple junction pairs connected in series seems appropriate. This would maintain the nominal thermocouple size specifications ( $\cong 100\text{-}\mu\text{m}$  long active junction) while producing a sensitivity which increases directly as the number of thermocouple junction pairs. The pixel width would presumably be greater than  $60\ \mu\text{m}$ , which is the GERB specification.
5. The results of this study clearly establish that the precision with which the individual pixels of a thermopile linear-array detector must be constructed to ensure uniformity of sensitivity and time constant is much greater than previously thought.

## **5.2 Recommendations for further study**

1. The influence of the thermophysical properties and the thickness of the thermal resistance and absorber layers on the sensitivity of the device and its time constant should be studied in a parametric fashion.
2. A three-dimensional model should be developed to account for three-dimensional diffusion of heat through the thermocouple and also to account for heat conduction cross-talk among the adjacent elements of the array of thermopiles. The boundary conditions will be provided by the results of a ray-trace model of the cavity currently being completed by another member of the Thermal Radiation Group, Maria Cristina Sánchez.

3. A complete instrument simulation should be done by incorporating the reflective optics workbench developed by Walkup [1996] of the Thermal Radiation Group to accurately simulate illumination of the array. Such an end-to-end detector model could be used to design an optimum staring or scanning radiometric channel for the future generation of CERES-type instruments.
4. Experiments to evaluate the Peltier and Thomson coefficients of the material used in the detector should be carried out to verify the hypothesis that the Peltier and Thomson effects are negligible.
5. The effects of diffraction by the entrance slit to the cavity should be incorporated into any subsequent Monte-Carlo ray-trace model

## References

ALGOR, Standard User's Manual, 1993.

Anon. Internetwork, Incorporation, *EOS A Mission to Planet Earth*, The National Aeronautics and Space Administration, 1993.

Barkstrom, B.R., *The Earth Radiation Radiation Budget Experiment (ERBE)*, **Bulletins of the American Meteorological Society**, Vol.65, No.11, 1984, pp 1170-1185.

Barkstrom, B.R., *Earth Radiation Radiation Budget Measurements: pre-ERBE, ERBE, and CERES*, **Proceeding of SPIE-The International Society for Optical Engineering**, Vol.1299, 1990, pp 52-60.

Benedicks, C., Siljeholm, C., *Arkiv for Matematik, Astronomi och Fysic*, 24A, No.7, 1933.

Bridgman, P.W., **The Thermodynamics of Electrical Phenomena in Metals**, The Macmillan Company, 1934, pp 39-77.

Callaway, J., **Quantum Theory of Solid State**, Second Edition, Academic Press, 1991.

Dereniak, E.L. and Crowe, D.G., **Optical Radiation Detectors**, John Willey and Sons, 1984.

Gebhart, B., **Heat Conduction and Mass Diffusion**, McGraw-Hill, 1993.

Haeffelin, M., **Introduction to Atmospheric Science and Engineering**, ME4984 course, Virginia Polytechnic Institute and State University, spring1997.

House, F.B., A. Gruber, G.E Hunt, and A.T. Mecherikunnel, *History of Satellite Missions and Measurements of the Earth Radiation Budget (1954-1984)*, **Review of Geophysics**, Vol.24, No.2, May 1986, pp 357-377.

Jastrzebski, Z.D., **The Nature and Properties of Engineering Materials**, Wiley and Sons, 1976.

Jaumont, F.E., **Direct conversion of heat to Electricity: Review of thermoelectric effects**, Kay, J. and Welsh, J.A., 1960, Chapter 4.

Krieder, K.G., **Intermetallic Thermocouples**, United States Patent, Patent Number 5,356,485, 1994.

Lee, R.B., Gibson, M.A., Thomas, S., Mahan, J.R., Meekins, J.L., Tira, N.E., *Earth Radiation Radiation Budget Experiment Scanner Radiometric Calibration Results*, **Proceeding of SPIE-The International Society for Optical Engineering**, Vol.1299, 1990, pp 80-91.

Mahan, J.R., Langley, L.W., **The Geo-Synchronous Earth Radiation Budget Instrument: Athermopile Linear-Array Thermal radiation Detector**, Proposal submitted to NASA, Hampton, VA, 1996.

Mahan, J.R., Langley, L.W., **Technology Development of a Sputtered Thermopile Thermal Radiation Detector for Earth Radiation Budget Applications**, Proposal submitted to NASA, Hampton, VA, 1997.

Pollock, D.D., **Physical Properties of Materials for Engineers**, Second Edition, CRC Press, Inc., 1993, pp 229-268.

Pollock, D.D., *Thermoelectricity Theory, Thermometry, Tool*, **American Society for Testing and Materials**, 1985, pp 111-132.

Pollock, D.D., *The Theory and Properties of Thermocouple Elements*, **American Society for Testing and Materials**, 1971, pp 6-14.

Priestley, K.J., **Use of First-Principle Numerical Models to Enhance the Understanding of the Operational Analysis of Space-Born Earth Radiation Budget Instruments**, Ph.D. Dissertation, Mechanical Engineering Department, Virginia Polytechnic Institute and State University, Blacksburg, VA (1997).

Ramanathan, V., Cess, R.D., Harrison, E.F., Minnis, P., Barsktrom, B.R., Ahmad, E, and Hatmann, D., *Cloud Radiative Forcing and Climate: Results from the Earth Radiation Budget Experiment*, **Science**, Vol 243, 1989, pp 57-63.

Reddy, J.N., **An introduction to the finite element method**, McGraw-Hill, Second Edition, 1993.

Sze, S.M., **Semiconductor sensors**, Wiley, J. and sons, 1994.

Tira, N.E., **Dynamic simulation of solar calibration of the total, Earth viewing Channel of the Earth Radiation Budget experiment (ERBE)**, M.S. Thesis, Mechanical Engineering Department, Virginia Polytechnic Institute and State University, Blacksburg, VA (1987).

Walkup, M.D., **A Monte-Carlo Optical Workbench for Radiometric Imaging System Design**, M.S. Thesis, Mechanical Engineering Department, Virginia Polytechnic Institute and State University, Blacksburg, VA (1996).

Weckmann, S., **Dynamic electrothermal Model of a Thermoelectric Linear Array Sensor for Radiometric Imaging from Space**, report submitted to the Insitut Universitaire des Systèmes Thermiques Industriels, France, 1996.

Wielicki, B.A. , Cess, R.D., King, M.D., Randall, D.A., and Harrisson, E.F., *Mission to Planet Earth : Role of Clouds and Radiation in Climate*, **Bulletin of American Meteological Society**, Vol.76, No.11, November 1995, pp 2125-2153.

## Vita

Stéphanie A. Weckmann was born on the [REDACTED] day of [REDACTED], [REDACTED] in [REDACTED], [REDACTED], France. After a Baccalaureate in Mathematics and Physics in 1990 she attended during three years a Preparatory School for competitive entrance examinations for French engineering schools. She was accepted to the Institut Universitaires des Systèmes Thermiques Industriels, an engineering school specializing in heat transfer in 1993, and she graduated three years later in 1996. In the same time she received a “Diplôme d’études approfondies (DEA)”, which is awarded after half a year of theoretical classes and the another half year of practical training preparatory to the doctorate. She spent her practical training in the Thermal Radiation Group, directed by Professor J. R. Mahan. At this time Professor J. R. Mahan proposed her to come back for a Master of Science. In August 1997, Stéphanie received her Master of Science Degree in Mechanical engineering.

Stéphanie Weckmann